PNNL-26585

Pacific Northwest
NATIONAL LABORATORY
Proudly Operated by Battelle Since 1965

Integrated Solar Thermochemical Reaction System

Final Report

April 2019

RF Zheng
RS Wegeng

U.S. DEPARTMENT OF ENERGY

Prepared for the U.S. Department of Energy
under Contract **DE-AC05-76RL01830**

DISCLAIMER

PACIFIC NORTHWEST NATIONAL LABORATORY
operated by
BATTELLE
for the
UNITED STATES DEPARTMENT OF ENERGY
under Contract DE-AC05-76RL01830

Printed in the United States of America

Available to DOE and DOE contractors from the
Office of Scientific and Technical Information,
P.O. Box 62, Oak Ridge, TN 37831-0062;
ph: (865) 576-8401
fax: (865) 576-5728
email: reports@adonis.osti.gov

Available to the public from the National Technical Information Service
5301 Shawnee Rd., Alexandria, VA 22312
ph: (800) 553-NTIS (6847)
email: orders@ntis.gov <http://www.ntis.gov/about/form.aspx>
Online ordering: http://www.ntis.gov


This document was printed on recycled paper.
(8/2010)

PNNL-26585

Integrated Solar Thermochemical Reaction System

RF Zheng
RS Wegeng

April 2019

Prepared for
the U.S. Department of Energy
under Contract DE-AC05-76RL01830

Pacific Northwest National Laboratory
Richland, Washington 99352

Abstract

This report describes progress accomplished in a three-phase project that has advanced the concept for a Solar Thermochemical Advanced Reactor System (STARS) – a system that is designed to convert solar energy into storable/useful chemical energy – from Technology Readiness Level 3 to Technology Readiness Level 6. STARS accomplishes its objective by directing the heat from a dish concentrator onto a chemical reaction system, increasing the energy content of the feedstock, methane, a chemical fuel that is available from multiple sources including natural gas, landfills and anaerobic digesters. The system uses a parabolic dish solar concentrator, previously developed for electrical power generation, and a compact, process-intensive chemical reaction system based on micro- and meso-channel process technology (MMPT).

The combined Dish-STARS™ system provides a solar augment to the incoming methane stream, increasing its chemical energy content by 20-30% while decreasing its carbon intensity. When the immediate chemical product, known as syngas, is directly used for power generation the result is electricity with approximately 20% less CO_2 emissions. Alternately, if the syngas is further reacted to produce valuable chemical products, such as hydrogen, the reduction in carbon emissions is retained and reduced carbon intensities can be attained for the chemical products. In a co-production mode, low-carbon hydrogen or electricity plus various hydrocarbons (for example, methanol, olefins or plastics) can be produced.

Over the course of this project, the efficiency of Dish-STARS™ was improved from a previous value of 63% to slightly over 70%, with results and analyses indicating a potential for values greater than 80%; manufacturing investigations identified fabrication methods for the MMPT components, proofed-out additive manufacturing for microchannel heat exchangers, developed equipment cost models and, together with on-sun testing, supported technoeconomic evaluations. If developed into commercial products, project results indicate the potential for the efficient use of concentrated solar energy in near-term applications for electrical power generation and the production of chemicals, including hydrogen.

Acronyms and Abbreviations

BOM	bill of materials
CNC	computer numerical control
COGS	cost of goods sold
CSP	concentrating solar power
DOE	Department of Energy
DMLS	direct metal laser sintering
DNI	direct normal irradiance
FE	finite element
HHV	higher heating value
HTR	high temperature recuperation
IR	infrared
LCOE	levelized cost of electricity
LCOA	levelized cost of augment
MPV	minimum viable product
MMPT	meso- and microchannel processing technology
MMBTU	million British Thermal Units
PD3	PowerDish™ III
PD4	PowerDish™ IV
PD5	PowerDish™ V
PDV	process development vehicle
PNNL	Pacific Northwest National Laboratory
PSA	pressure swing adsorption
S/C	steam to carbon ratio
SLM	selective laser melting
SMR	steam methane reforming
STARS™	Solar Thermal Advanced Reaction System™
TRL	technology readiness level
TDV	technology development vehicle
WGS	water gas shift

Contents

Figures

Tables

1.0 Introduction

This report describes the development of the Solar Thermochemical Advanced Reactor System (STARS), a system that is designed to convert solar energy into storable/useful chemical energy with relatively high efficiencies. The system accomplishes this by directing the heat from a dish concentrator onto a reaction system, increasing the energy content of the feedstock, methane (CH_4), a chemical fuel that is available from multiple sources including natural gas, landfills and anaerobic digesters. The system uses a parabolic dish solar concentrator, previously developed for electrical power generation, and a compact, process-intensive chemical reaction system based on micro- and meso-channel process technology (MMPT).

The system provides a solar augment to the incoming methane stream, increasing its chemical energy content by 20-30% while decreasing its carbon intensity. When the immediate chemical product, known as syngas, is directly used for power generation the result is electricity with approximately 20% less CO_2 emissions. Alternately, if the syngas is further reacted to produce valuable chemical products, such as hydrogen, the reduction in carbon emissions is retained and reduced carbon intensities can be attained for the chemical products. In a co-production mode, low-carbon hydrogen or electricity plus various hydrocarbons (for example, methanol, olefins or plastics) can be produced.

This project builds on an earlier effort combining high TRL parabolic dish concentrators with prototype MMPT components for steam-methane reforming. This effort advanced the concept to a Technology Readiness Level of 3 (TRL 3) and earned a world-record solar-to-chemical energy conversion efficiency of 63 +/- 4%.

Our approach to solar energy utilization makes use of the high-temperature heat from solar concentrators to increase the chemical energy content of a reacting stream, in this case to convert methane to synthesis gas (syngas). The chemical reactions that are accomplished within STARS are commonly referred to as "steam-methane reforming (SMR)" and "water-gas shift (WGS)" and are listed in their idealized forms as follows:

$$CH_4 + H_2O \rightarrow CO + 3H_2 \qquad \text{(steam-methane reforming)}$$
$$CO + H_2O \rightarrow CO_2 + H_2 \qquad \text{(water-gas shift)}$$

While the water-gas shift reaction is exothermic, the net reaction is nevertheless highly endothermic. Both reactions occur in our solar reactor and the actual products will consist of a mix of carbon monoxide (CO), hydrogen (H_2), some carbon dioxide (CO_2) plus some unreacted water (H_2O) and methane (CH_4). Overall, the chemical energy content of the reacting stream is increased by up to about 20-30%.[1] CH_4 sources include natural gas and biogas (e.g., gas from an anaerobic digester).

Figure 1-1 depicts the application of STARS to provide a solar thermochemical augment to a combined-cycle power plant.

[1]As measured by the maximum increase in the Higher Heating Value (HHV) of the stream, the proportional increase in the idealized version of the combined reactions is about 27%. Alternately, when measured as Lower Heating Value (LHV), the proportional increase is about 21-26%, depending upon the extent to which carbon monoxide in the product stream is additionally reacted through the water-gas shift reaction.

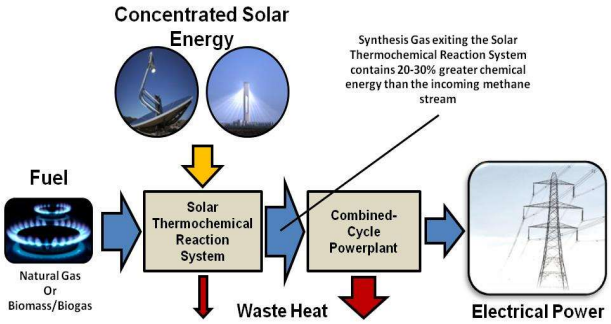

Figure 1-1 Solar Thermochemical Augment. Concentrated solar thermal energy is used to increase the chemical energy content of the fuel stream by up to about 27% (as measured as the increase in the HHV) subsequent to use in a combined-cycled power plant.

Combining this with the proven high efficiencies associated with a combined-cycle powerblock or with an advanced fuel cell powerblock, each of which are approximately 50-60% efficient, our expectation is that overall solar-to-electricity efficiencies of up to about 40% will be achieved.

This approach to CSP can use any solar collector capable of heating the reactants to approximately 700ºC or above, but those that can do this at high efficiency and moderate cost are, of course, most attractive. The parabolic dish provides the highest amount of solar exergy, per square meter of mirror surface, and allows commercial-scale development at a relatively modest cost.

Our Phase 1 and Phase 2 investigations provide an expectation that the solar thermochemical reaction system can be mass produced at sufficiently low costs to enable the production of electrical power at a LCOE below 6 ¢/kWh, the DOE SunShot goal for 2020. However, considerable work still needs to be accomplished in order to reach this goal.

Work by Others

Over the past few decades, a number of relevant laboratory-scale and prototype solar thermochemical demonstrations were performed in the United States and abroad. Among them are R&D projects and demonstrations conducted in the 1980s and 1990s that included CH_4 reforming. Solar-to-chemical energy conversion efficiencies as high as 55% were reported.

A summary listing of this past work was reported in our Phase 1 continuation report and is not repeated here due to page count limitations. Readers are referred to the previous report for details.

Significance, Innovation, and Fundamental Advances

The most important advance that our project accomplished during Phase 1 was increasing the solar-to-chemical energy conversion efficiency from our previously reported value of 63+4% to 69%. During Phase 2, efficiency potentially improved – through the reduction in heat leaks and reduced temperature gradients with the reactor – with the result being that the limited TRL 5 STARS testing suggests we will be able to observe efficiencies in the mid-70% through continued testing of the system during the first few months of Phase 3.

Techno-economic calculations suggest that these efficiencies are good enough for the project to support the SunShot goal of 6 ¢/kWh; however, it is clear from the effort that accomplishing the mass-production of STARS hardware at reasonable costs is critical.

The scientific and technical innovations associated with this project are derived in four principal areas. First is the development of chemical reactors that can be used as solar receivers with high conversion of incident solar flux to high-temperature heat and high conversion of heat to chemical energy through endothermic chemical reactions. The second area of innovation is developing unique, highly integrated chemical networks, to accomplish operations with high exergetic efficiency.

Our unique application of microchannel and mesochannel technologies to reduce hardware size and accomplish high efficiencies takes advantage of the low resistance to heat and mass transfer in channels having small cross-sectional dimensions. In addition, because heat and mass transport are rapid, high heat transport power densities are accomplished (10 to 100+ watts/cm^3). For solar thermal applications, a high receiver heat transfer rate is essential; it is therefore necessary to reduce receiver heat loss and reduce cost. As a result of this new approach, the reactor and the component heat exchangers in the system are simultaneously process-intensive (i.e., compact) and able to operate with high exergetic efficiencies. This is a key requirement and enabler of efficient solar receivers.

The third area of innovation is to develop new and novel methods for mass producing the thermochemical process hardware at affordable costs. This work has the potential of enabling new, efficient process systems, not just for our solar thermochemical process system, but for a number of other potential applications where size and efficiency are important.

The fourth area in which technical merit is derived comes from the benefit of converting solar thermal energy to chemical energy. Carnot's rule dictates that operating heat engines at higher heat-input temperatures results in higher theoretical conversion efficiency; however, conventional CSP approaches directly couple the concentrator and the heat engine such that the heat engine cannot be operated at a higher temperature than the solar concentrator can efficiently provide. It is clear that significant performance and economic advantages can be achieved by efficiently producing a fuel that can be combusted in conventional power plants, potentially at much higher temperature than the concentrator provides. Combined-cycle power plants, including advanced systems that are capable of 1200 to 1400°C operating temperatures, therefore provide an opportunity for very high solar-to-electrical efficiencies. Likewise, the utilization of STARS' syngas product in fuel cells, the efficiencies of which are not constrained by Carnot Cycle limitations since they are not heat engines, is another route to very high solar-to-electrical efficiencies.

2.0 Summary and Conclusions

Substantial progress was achieved during this cost-shared project in progressing STARS technology – from an early prototype system in a previous project – through a staged, iterative approach that considered multiple measures of cost and performance to advance the system, achieving a Technology Readiness Level of 6 (TRL 6) during Phase 3 of the project. As a result of this effort, the STARS technology platform is believed to be within 2-3 years of commercial readiness for an initial, Minimal Viable Product (MVP) at TRL 9.

While electrical power generation was the original focus of this project, it is believed that hydrogen production from natural gas, based on the addition of a water-gas shift (WGS) reactor and hydrogen purification, is considered to be the MVP opportunity. The WGS reactor and purification components, based on pressure-swing adsorption, are already at high TRLs, thus allowing their inclusion through engineering efforts (as opposed to additional substantial technology development).

Additional work is required to advance to TRL 9, the point where commercial deployment is possible. However, assuming that continued development efforts overcome barriers to commercialization, including additional efficiency advances and the establishment of manufacturing capabilities for parabolic dishes and MMPT reactors and heat exchangers, it is believed that Dish-STARS™ will be competitive with alternatives such as electrolysis or conventional steam-methane reforming.

2.1 Technical Progress

Technical progress was achieved in this project in three, interactive areas: 1) performance assessments and enhancements for the STARS reactor, heat exchangers, and integrated system, enabling highly efficient conversion of solar energy to chemical energy; 2) investigations of manufacturing cost methods for MMPT components, including demonstrations and manufacturing cost studies; and 3) technoeconomic evaluations for power generation (in Phases 1, 2 and 3) and hydrogen production (in Phase 3) that evaluated the financial impacts of improvements and aiding in the setting of component and system objectives in each phase of the project.

Specific achievements during the project include:

- Through an iterative process that included design, fabrication and on-sun testing of MMPT reactors and heat exchangers, including analysis of test results, the maturity of the Solar Thermochemical Advanced Reaction System (STARS) technology platform was advanced from TRL 3 to TRL 6.

- In on-sun tests, STARS' solar-to-chemical energy conversion efficiency[2] was increased from 63% to slightly more than 70%. Test results combined with analyses indicate that, with an improved dish, efficiencies as high as 75% would have been obtainable with the TRL 6 system. Yet higher efficiencies, as high as 80%, are believed to be obtainable through the use of higher performance concentrators and with additional improvements to the reaction system.

[2] Based on higher heating value increase. See 4.3.3.4, Equation (22), for a full definition.

- The STARS technology platform received an R&D 100 Award in 2014.

- Mass production manufacturing methods for STARS components were investigated, particularly for MMPT reactors and heat exchangers. Additive manufacturing was demonstrated for multiple microchannel heat exchangers, including a high-temperature, highly effective heat exchanger, as part of the project.

- Technoeconomics for power generation and hydrogen production confirmed the potential for electricity production in a hydrid solar/natural gas powerplant at about 6-7¢/kWh and hydrogen production in the range of $1.25-$2/kg.

2.1.1 Advances in Performance and Cost

2.1.1.1 STARS On-Sun Performance

As discussed in Chapter 1.0 of this report, STARS performance was improved throughout the project through as combination of simulations (including flowsheet simulations using CHEMCAD and 3D reacting flow simulations using COMSOL Multiphysics®), through analyses including Second Law analyses (i.e., exergy analyses), and testing. These improvements can be highlighted by two critical metrics: 1) Reactor-receiver efficiency and 2) Solar to chemical energy conversion efficiency. The former is focused on the performance of the reactor-receiver combination as well as the effectiveness with which the steam-methane stream is preheated by recuperative heat exchange prior to the reaction and the latter includes consideration of the inefficiencies in the dish-concentrator. The numerator of both metrics contain the increase of the Higher Heating Value of the reacting stream and are discussed in greater detail in Chapter 4.0 (in particular, see Section 4.3.3.4). Noting that the price of natural gas is often expressed in dollars per million British Thermal Units ($/MMBTU), where the denominator is based on the Higher Heating Value of the natural gas, both of our efficiency metrics therefore directly correspond to an increase in economic value.

Table 2-1 tracks progress in these two critical metrics through the three phases of the project and identifies the potential performance improvements that could be realized through the combination of a highly efficient STARS reaction system and improved parabolic dish concentrators.

As Table 2-1 shows, the solar to chemical energy conversion efficiency of STARS was improved during the course of the project to slightly greater than 70%, a world record. This was accomplished during Phase 2 with the TRL 5 system and in Phase 3 with the TRL 6 systems. However, while the TRL 6 reactor-receiver efficiency was greater than in the TRL 4 and TRL 5 systems, the dish-concentrator used during Phase 3 of the project attained an inferior solar intercept (compared to the concentrator used during Phases 1 and 2). For this reason, the solar to chemical energy conversion efficiency attained through on-sun tests during Phase 3 were not as high as expected. Table 2-1 presents this information also with the expectation that, with an improved concentrator and with the combination of an improved concentrator with further improvements in the integrated reaction system, solar to chemical energy conversion efficiencies of 75% and 80% are attainable.

Table 2-1 Dish-STARS™ system and component performance metrics.

Project Phase	*Technology Readiness Level*	*Peak Reactor-Receiver Thermal-to-Chemical Energy Conversion Efficiency* [3]	*Dish Concentrator Solar Intercept* [4]	*Peak System Solar-to-Chemical Energy Conversion Efficiency* [5]
1	4	83%	0.9	69%
2	5	87%	0.87-0.89	71%
3	6	95%	0.83	73%
Future Potential (improved dish)	6	95%	0.9	79.5%
Future Potential (improved dish and reaction system)	7-8	95%	0.95	83.9%

A thorough discussion of reactor and heat exchanger simulation and design details, fabrication and assembly steps, catalyst performance investigations, dish-concentrator calibration methods, on-sun testing, and experimental data analysis, and activities that steadily improved the efficiency of the reaction system such as through the investigation of sources and magnitudes of heat loss and exergy destruction, is presented in Chapter 4.0.

2.1.1.2 Manufacturing Methods and Costs

The capital cost for Dish-STARS™ is another important metric in which progress was made during this project. As is described in Chapter 4, it was determined during Phase 1 that the high temperature reactor and recuperative heat exchanger were the majority (slightly greater than 80%) of the STARS equipment cost items. Efforts during Phase 1 and 2 therefore concentrated on reducing the cost for these two components as well as determining the cost advantages associated with mass production. Two manufacturing approaches for each of these components were downselected during Phase 2 and the Phase 3 effort was expanded to include initial cost models for the parabolic dish concentrator, which is still believed to be the highest STARS cost components.

Table 2-2 provides a summary of the Phase 3 results for the reactor, high temperature heat exchanger (HTR) and the concentrator. The table includes a comparison for costs at two volume manufacturing rates (1000 units per year and 10,000 units per year). In addition, while evaluating the potential for further technology improvements was not a part of this project's work scope, Table 2-2 presents the impact of a possible 30% reduction in cost associated with a "learning curve" such as has been applied to the development of cost targets for heliostat mirrors under the DOE CSP program.

[3] Peak efficiency measured experimentally, based on the reactor stream HHV increase and the total solar energy intercepted by the receiver-reactor (see definition in Eq. 21).
[4] The reflectivity of the parabolic dish in all cases is assumed to be 0.93.
[5] Peak efficiency measured experimentally, based on the reactor stream higher heating value (HHV) increase and the total solar energy incident upon the dish concentrator (see definition in Eq. 20).

Table 2-2 PD3-Scale Dish-STARS™ component cost projections at 1,000 and 10,000 annual production rates.

Component	*Manufacturing Method*	*10^3 units per year*	*10^4 units per year*	*10^4 units per year with 30% reduction due to technology improvements*
Reactor	Machined	$ 2,288	$ 1,735	$ 1,215
	Additive	$ 1,695	$ 982	$ 687
HTR	Half-Array	$ 1,086	$ 216	$ 151
	Additive	$ 1,212	$ 1,104	$ 773
Concentrator	PD3 (scaled down from PD4 size)	$ 4,501	$ 3,152	$ 2,207
	PD3 (approximated as Solartron 4.5m dish)	$ 6,480	$ 7,884	$ 5,519
Best Case System		$ 7,282	$ 4,350	$ 3,045

The above table also sums the cost for the best case in each column and allows a favorable comparison to technoeconomic calculations performed early in Phase 3 based on Phase 2 assumptions, thus verifying our expectation that Dish-STARS™ can support electricity production through a hybrid solar/natural gas powerplant within a cost target of 6-7¢/kWh and hydrogen production at costs well below the DOE goal of $2/kg.

2.2 Follow-on Work

As a result of the success of this project, two additional cost-shared projects have been proposed and accepted. One is focused on advancing a Minimum Viable Product (MVP) version of Dish-STARS™ for hydrogen production in California to TRL 8 over a two-year period. The other is focused on developing and proving MMPT manufacturing methods that are mass-producible and, if successful, are targeted to further reduce costs below those identified in this report.

3.0 System Evaluation and Optimization

3.1 System Evaluation and Optimization

This task investigated different configurations for a few Dish-STARS™ applications. The baseline project application, power generation through a utility-scale, hybrid solar/natural gas-fired combined-cycle power plant, is described below in Section 3.1.1. Initial evaluations of renewable pipeline gas and hydrogen generation are also being developed and are described in Section 3.1.2.

Table 3-1 End-of-Phase 2 STARS Performance Assumptions

Parameter	*Value*
Concentrator reflectivity	0.930
Concentrator spillage factor (solar intercept)	0.950
SMR fixed thermal loss W/m² concentrator	0.067
SMR chemical energy fraction	0.9806
DNI to chemical energy @ 1000 W/m²	0.801
Annual possible DNI to chemical energy in Phoenix	0.758
Allowance for off-design performance and outages	0.950
Net annual DNI to chemical energy in Phoenix	0.720

It should be emphasized that all economic results reported here were performed during the first two quarters of Phase 3. They are preliminary, based on manufacturing cost estimates and experimental performance for STARS components developed in Phases 1 and 2, and provide an understanding of how the combination of equipment cost and performance affect the cost of electricity and hydrogen from Dish-STARS™ applications. Updated cost estimates for key STARS components will be generated in future projects.

Common to the evaluation of all applications are the design point and annual performance assumptions shown in Table 1 for the solar SMR. The net annual conversion efficiency figure now incorporates a 95% factor to allow for less than design performance and/or outages as suggested by DOE at the Phase 2 review. The inclusion of the 98% chemical energy fraction also represents a refinement from Phase 2 modeling. This 2% factor arises from less than perfect recovery of thermal energy from the SMR product stream.

Aspen models were developed to evaluate alternative equipment configurations for each application. A key design variable, requiring tradeoff evaluations, is SMR pressure. Lower pressure allows higher methane conversion, but requires recompression of the syngas for the applications being investigated. The models also allow optimization of the thermal energy recovery network exchanging heat between

[6] This value varies from 0.97 to 0.99 depending on SMR pressure and steam/carbon ratio.

product and feed streams. The results of these process optimizations are described in the following sections.

3.1.1 Gas Turbine Technoeconomics Evaluation

During Phase 2 of this project, PNNL worked with Siemens to evaluate using Dish-STARS to reduce natural gas consumption in a utility-scale combined-cycle power plant. Although preliminary results were reported at the end of Phase 2, system optimization was left to Phase 3. Unfortunately, in the interim between Phases 2 and 3, the Siemens group in Orlando that had been working with PNNL was disbanded. Thus, the system optimization was completed by PNNL alone using the same analytical methodology established by Siemens during Phase 2.

The system optimization evaluated 5, 10, and 20 bar SMR operating pressures and the two "fuel preparation" configurations. As noted above, lower SMR operating pressures allow higher methane conversion, but require larger compressors. The Siemens combustion turbine requires 435 psia fuel for proper burner flow control (the actual pressure at the burner tip is approximately 290 psia). Therefore, SMR operation at lower pressure requires compression of the syngas product. This requirement is exacerbated by the fourfold increase in volume of the syngas product compared to the natural gas feed.

The primary difference in the two configurations is the location of the first compressor. In one configuration, syngas is compressed after cooling to ambient and condensing and removal of most of the steam, which minimizes compressor cost and power consumption. In an alternate configuration, the syngas is partly compressed after leaving the high-temperature recuperator, which increases the energy that can be transferred to the feed stream. This increases compressor costs, of course, but reduces feedwater boiling duty since it enables condensation and recovery of steam at a higher temperature, suitable for steam generation for the SMR.

Table 3-2 Configuration Design and Performance Characteristics[7]

Design Configuration	***1***	***2***	***3***	***4***
SMR pressure, bar	5	5	10	20
Warm syngas compression	yes	no	no	no
Recuperator, Btu/hr	36,570	35,587	35,480	34,084
Syngas cooler, Btu/hr	18,334	9,346	8,206	6,996
Syngas condenser, Btu/hr	16,124	10,962	13,993	16,938
Supplemental Boiler, Btu/hr	9,170	23,413	22,547	21,524
Ambient air cooler, Btu/hr	6,426	9,449	11,008	12,199
Methane conversion	.819	.819	.72	.585
Annual solar fraction of GT energy input	0.0462	0.0462	0.0413	0.0348

[7] Based on 1 lb-mol CH_4 and 2 lb-mol H_2O SMR feed.

LP compressor, kW	3.18	1.33	None	None
HP compressor, kW	2.06	2.06	1.72	0.51

Key Aspen modeling results are shown in Table 3-2 for the four configurations evaluated. The results show that compression of the warm syngas leaving the recuperator cuts the supplemental boiling requirement by approximately 60%, but more than doubles the size, cost, and parasitic power consumption associated with the low pressure compressor. Greater heat recovery also requires a larger syngas cooler and syngas condenser. The net effect of warm syngas compression is to increase power plant levelized electricity cost, so this option was not further considered.

Increasing SMR operating pressure from 5 to 10 and 20 bar significantly reduces methane conversion, but higher pressure allows mass flow rate to increase without reducing reactor residence time, hence maintaining close approach to theoretical methane conversion while fully absorbing available solar energy[8]. Solar to chemical energy conversion remains nearly constant, but the solar fraction of syngas energy and annual solar fraction of all gas turbine energy input decline.

The overall cost and performance results for the reference power plant and the three solar hybrids at different SMR pressures are shown in Table 3-3. The preference for operating the SMR at higher pressure for this application is indicated by the higher power output, lower capital cost, and lower levelized electricity cost for the 20 bar configuration.

Table 3-3 Power Plant Cost and Performance Results[9]

Case		*NGCC,1x1*	*Case 1*	*Case 2*	*Case 3*
Primary fuel		Methane	Methane	Methane	Methane
GT fuel		Methane	Methane / Syngas	Methane / Syngas	Methane / Syngas
SMR Operating Pressure	bar	N/A	5	10	20
Syngas Net Power	kWe	N/A	290,570	297,776	303,080
Annual Solar Fraction GT Fuel		0	0.0462	0.0413	0.0348
Natural Gas Net Power	kWe	291,823	291,823	291,823	291,823
Plant Efficiency	%LHV	56.08%	53.93%	55.29%	56.3%
Raw Water Consumption	L/kWh	0.98	1.28	1.24	1.22
Total Overnight Cost (TOC)	$k	$333,426	$477,710	$446,478	$422,402
Total Overnight Cost	$/kWe	$1,143	$1,639	$1,524	$1,438
First year O&M + Fuel	$/MWh	$41.95	$43.04	$42.75	$42.79
Levelized Cost of Electricity	$/MWh	$61.38	$70.69	$69.19	$68.12

3.1.2 Hydrogen Production Technoeconomics Evaluation

Five different hydrogen plant configurations were evaluated. A central hydrogen plant, producing 100 metric tons per day (MTPD), was evaluated for SMR pressures of 2, 10, and 20 bar. The best SMR operating pressure was then evaluated for distributed hydrogen plants with 1500 kg/day and 200 kg/day

[8] The present analysis ignored the effects of pressure on reactor mass transfer or press dependency of SMR reaction kinetics, which should be considered in a more detailed analysis as follow-on work.
[9] All costs are in 2011 dollars.

capacities. 100 MTPD was selected for the central plant capacity because it requires approximately the same number of parabolic dishes as the utility-scale power plant application and is comparable to conventional large hydrogen plant capacities. 1500 kg/day is the reference size for distributed hydrogen production used by DOE's Fuel Cell Technology Office. Finally, 200 kg/day is the approximate size of hydrogen fueling stations currently being installed in California for fuel cell vehicles.

For the larger four configurations, solar field costs were estimated based on the same unit costs as used in the utility-scale power plant application, i.e., they were based on manufacturing a few thousand concentrators, SMRs, heat exchangers, and other distributed components per year. For the 200 kg/day configuration, the unit costs for manufactured components were increased by a factor of three based on production volume cost curves developed in Phases 1 and 2. This multiplier will be revised as updated production volume cost curves are completed next quarter.

Producing hydrogen from syngas requires two additional processing steps beyond that required for the power plant application. After leaving the high-temperature recuperator, the syngas is sent to a water-gas-shift (WGS) reactor where CO and H_2O are reacted to produce CO_2 and H_2. This reaction is moderately exothermic, hence conversion is favored by lower temperatures. Commonly, WGS is accomplished in two stages, with the first stage operating at higher temperature to improve reaction kinetics and the second stage operating at a lower temperatures to achieve additional conversion.

Downstream from the WGS reactors, hydrogen must be separated from the gas mixture. Although membrane separation is an option, the preferred technology typically is a pressure-swing adsorption (PSA) system. PSA technology scales down well to sizes applicable to 200 kg/day production and is capable of producing the nearly pure hydrogen required by fuel cell vehicles. As its name implies, PSA systems work by first preferentially adsorbing non-H_2 species on a solid adsorbent bed at high pressure. After one bed becomes loaded the feed stream is routed to another bed while the first bed is regenerated by lowering its pressure and flushing with pure H_2. In practice at least 4 beds are used in a system, but additional beds are often used to achieve higher H_2 recovery fractions.

As noted above, lower SMR operating pressures favor methane conversion but will generally increase syngas compression requirements, depending on the use of the syngas. PSA systems require inlet pressures near 300 psia or higher to be effective. Thus, a tradeoff similar to that described above for a utility scale power plant application occurs. However, methane conversion matters a lot more when the objective is to produce hydrogen and especially for a solar-powered SMR. In conventional hydrogen plants, the tail-gas from the PSA provides the SMR reaction heat as well as boiling feedwater. For these preliminary evaluations, tail-gas use was limited to boiling feedwater; this puts additional emphasis on achieving high methane conversion and high hydrogen recovery in the PSA. However, alternative configurations are available for future evaluation/optimization, including recycle of the tail gas to the SMRs and/or staged SMRs that operate at lower pressures, therefore yielding higher overall methane conversions while limiting additional recompression requirements.

Table 3-4 Hydrogen Plant Performance

SMR pressure	20 bar	10 bar	2 bar
CH_4 conversion	0.693	0.805	0.894
CO conversion	0.976	0.971	0.962

H_2 production[10]	7.28	7.30	7.32
CH_4 consumption	2.64	2.29	2.07

System performance at 2, 10, and 20 bar SMR pressures is shown in Table 4. Both SMR and WGS conversions were assumed to be 90% of that reached at equilibrium. The SMR temperature was set to 815°C in all cases. Methane conversion increases significantly as pressure is dropped. Solar to chemical conversion efficiency is maintained by increasing the feed rate of steam and methane. Although hydrogen production is essentially the same, natural gas consumption changes significantly.

System capital cost estimates and levelized hydrogen cost estimates are presented in Table 5 for the five H_2 plant configurations evaluated, normalized to a $\$/m^2$ concentrator area basis. As SMR pressure drops, syngas compression costs rise while natural gas consumption drops. The levelized hydrogen cost results indicate that relatively low SMR pressures will likely be preferred, but the sensitivity of cost to SMR pressure is not great.

Table 3-5 Hydrogen Plant Installed Costs ($/m2 dish aperture area)

Kg H_2/day	100K	100K	100K	1,500	200
SMR pressure, bar	20	10	2	2	2
Dish, SMR, & High-Temperature Recuperator	390	390	390	391	1172
WGS	85	85	85	85	255
Piping	55	56	57	79	97
Low-Temperature Heat Exchangers	22	33	38	38	113
Syngas Compressors	4	45	248	331	597
PSA	289	281	276	825	1364
System Total	845	891	1094	1750	3597
Levelized H_2 Cost, $/kg	1.41	1.27	1.26	1.43	1.97
$/MMBTU	10.5	9.5	9.5	--	--
Natural gas cost fraction	0.78	0.75	0.68	0.55	0.39

Natural gas is the largest component of hydrogen production cost, except for the smallest plant at low-volume solar field production. Therefore, the optimum SMR pressure will depend more on expected future natural gas prices than any other single factor. These results are based on natural gas pricing for the electric power sector as defined by EIA's 2015 Annual Energy Outlook. Specifically, natural gas was assumed to cost $4.43/MMBtu (2013$) in the first year of operation (2018) and escalate at a real (excluding general inflation) rate of 2.74%/year. Lower natural gas prices would push the optimum SMR pressure higher and vice-versa.

Of greatest importance, the results show that a solar-powered SMR could be used to produce hydrogen at a very competitive price, even at small scale. For all cases but the 200 kg/day plant based on low volume production of solar field components, the levelized hydrogen cost is less than the $2/kg goal set by the Fuel Cell Technology Office. Alternately, for the case of producing hydrogen for reinjection into the natural gas pipeline, the preliminary calculations suggest production costs as low as $9.5/MMBTU.

[10] Flow rates in Aspen Plus model; not flow rates at actual plant size.

The results shown in Table 3-5, however, are very preliminary. Not yet included is the option of using renewable electricity overgeneration, based on California's goal that 50% of its electricity would come from renewable resources. In this case, the potential use of the overgeneration at a few cents per kilowatt-hour, for example with internal electrical resistance elements within the solar SMR, can increase its annual H_2 production by perhaps more than double what it would produce using concentrated solar energy alone. Since capital costs would essentially be unchanged, preliminary calculations suggest a substantial cost advantage for hydrogen production.

In addition, ongoing production cost studies for our solar field components will likely change the cost assumptions used in calculating these figures. Nor have the systems been optimized even for the current solar component cost assumptions. For example, the PSA costs are based on sizes required to meet peak hourly production on summer solstice. Adding pressure vessels for several hours of syngas storage will likely reduce total system capital cost and levelized hydrogen production cost.

4.0 Solar Thermochemical Reaction System Development

The objective of this task was to iterate the solar thermochemical reaction system design through cycles of design, build, testing, and analysis in order to improve the system performance and to progress the system technology readiness level from TRL 3 at the start of the project to TRL 6 at the end of the project. Activities under this effort included (1) solar concentrator test stand development, (2) on-sun testing of solar thermochemical reaction systems, (3) catalyst performance testing, and (4) finite element analysis based solar reforming reactor design. In this chapter, work performed in this group of activities will be described and the results from the overall reaction system development will be given.

4.1 Reaction System Design

The design of the reaction system considered two important goals: (1) continuing to improve the performance of the reaction system (e.g., increasing the solar-to-chemical energy conversion efficiency) and (2) reducing the manufactured cost of the reaction system. The reaction system design went through three iterations during the course of this project: TRL 4 to TRL 6. Performance improvements have been made through component improvements that resulted in better heat recuperation, lower heat losses, and closer to optimal reaction zone temperature. Improvements in manufacturing costs by design have been made through the reduction in the mass of metal alloys needed for the component fabrication and through substitution of the high temperature alloys with less expensive types. In the following sections, the fundamental design approach, the progression of the design over project phases, and notable results are described.

4.1.1 General Design Approach

The dish-reactor system concept places certain mass and volume requirements on the design of the reaction system. The methane reforming reactor and its heat exchanger network need to fit within the housing of an on-sun reactor-receiver so that the reactor can be located at the focal point of a parabolic dish concentrator in sun-tracking movement. Our base design is to use micro- and meso-channel technologies (MMPT) to reduce hardware size by taking advantage of extremely rapid heat and mass transfer to achieve high transport power densities (10-100+ watts/cm^3). As a result, the reactor and the component heat exchangers in the system will be much more process-intensive (i.e., compact) and operated with high exergetic efficiencies.

MMPT describes a class of chemical and thermal systems that take advantage of the rapid heat and mass transfer rates that occur over small dimensions. A micro-channel is defined as a flow channel having at least one dimension in the sub-millimeter range—typically 100 to 500 microns. Meso-channels are slightly larger flow channels, with one dimension typically less than one centimeter. Because residence times for heat and mass transfer scale inversely of hydraulic diameter, tenfold to hundredfold improvements in these fundamental processes can be realized in micro- and meso-channel architectures. Proper design requires tradeoffs among science (maximizing transport rates), engineering (minimizing pressure drop), and economics (manufacturability). As a result, most micro- and meso-channel devices are composed of parallel arrays of short channels. These designs employ arrays of flow channels with small hydraulic diameter while keeping the flow path relatively short, resulting in acceptable pressure drops through the device even at high throughput.

4.1.1.1 Solar Methane Reforming Reactor

The design of the solar thermochemical reactor needs to satisfy multiple constrains. Size and shape constrains were mostly driven by the requirement to place the reactor at the focal point of a sun-tracking parabolic dish concentrator. Selection of the materials of construction and plate dimensions were driven by operating temperature and pressure as well as costs. Internal dimensions and reactor channel configuration required optimization to maximize conversion and heat recuperation.

The solar irradiation concentrated by a parabolic dish is focused to a nominally circular spot. A radial arrangement of substantially parallel reaction channels naturally arose out of the cyclic symmetry of the concentrator reflector panels. The concentrator chosen, i.e. dish-concentrator from the Infinia PowerDish™ III (PD3), originally developed for a dish-Stirling power generation system, has a small non-reflective center as part of mounting hub for the mirror panels. The realization that the reactor center received no direct solar flux led to an elegant design where the gas connections to the reactor were made at its center so that the valuable flux-receiving surface is optimally used to deliver heat to reaction. This general design was retained and improved throughout the course of this project.

4.1.1.2 Recuperative Heat Exchangers

To maximize the exergetic efficiency of the reaction system, a network of heat exchangers was used to recuperate heat from the product streams. The MMPT recuperative heat exchangers were designed to satisfy the space and weight constrains, similar to the SMR reactor component. The required temperature duty of these exchangers are different: further downstream from the solar thermochemical reactor the feed and product stream temperatures are lower. This leads to a general design approach to use different grade of alloy materials for these heat exchangers so that the overall cost is reduced. The performance of the recuperative heat exchangers was carefully modeled by process simulation (CHEMCAD).

4.1.1.3 Solar Concentrator

While different solar concentrators were considered as part of the manufacturing costs analysis, the development of a new dish concentrator was not part of this project. The approach adopted was to select a commercialized parabolic dish concentrator for pairing with the reaction system development. The Infinia PD3 concentrator was selected for this purpose. Limited modifications were made to enable mechanical, fluid, power, and control system interface with the reaction system. The reflector, receiver, and tracking system were not modified.

4.1.1.4 Balance of Plant

The control system and other ground equipment make up the balance of plant. The control system for the reaction system was designed to integrate with the control system of the dish concentrator for operation efficiency and safety. LabVIEW-based embedded industrial controllers were used to provide a balanced performance of robustness and flexibility. The reaction system design took into account the unique piping requirements by the sun-track dish concentrator. Rotary unions and flexible hoses were used to allow motion of the reactor along with the dish relative to the ground. These critical piping components were selected to meet the temperature, pressure and flow duty requirements by the reaction system.

4.1.2 Reactor-Receiver Energy Balance Analysis

For a design perspective, thermal losses around the reactor-receiver envelope can be a major source of efficiency loss of the reaction system and should be minimized. During Phase 1, these thermal losses were evaluated using the CIRCE2 and AEETES computer codes originally developed at Sandia National Laboratory. The CIRCE2 optical analysis code was used to define the incident flux profile within the PD3 receiver cavity. The analyses are one-dimensional. The AEETES analysis calculated the redistribution of reflected solar and thermal energy within the receiver cavity using a two-band model in which the radiative energy redistribution was determined using solar and infrared properties. View factor algebra was employed to calculate the thermal and solar energy distribution between the 49 ring elements that defined the receiver in the model. The one-dimensional temperature profile, along with the losses through the aperture is iteratively solved. Cavity natural convective losses were calculated using the Stine-McDonald correlation and were a function of the cavity geometry and the sun elevation angle. Conduction losses through the cavity insulation were also calculated. For the analysis only one-dimensional conduction through the side wall insulation was determined. Conduction losses from the back and sides of the reactor are not included in the analysis.

Thermal loss estimates for the Infinia PD3 at a representative data point, calculated with the CIRCE2 and AEETES programs, are summarized in Table 4-1 along with estimated uncertainties for the various sources of heat loss and model assumptions. The modeled data point represented typical operating conditions of the TRL 4 reactor under development during Phase 1.

Table 4-1 Receiver heat loss/efficiency uncertainty estimates

	Nominal, W	*Estimated Minimum, W*	*Estimated Maximum, W*	*Comments*
Incident Solar Power	11764	12117	11411	Dish Area = 14.85 m^2, ρ = 93% ϕ = 90%, DNI = 866 W/m^2 ,+/- 3%
Net Power	10475	10615	9185	Net thermal power delivered by the receiver/reactor assuming nominal incident power
Solar Reflection Loss	109	59	159	Solar α = 0.85 to 0.95
Infrared Radiation Loss	753	713	793	+/- 15ºC surface temp, IR ε = 0.80
Cavity Convection Loss	366	316	666	Nominal. 50 degree elevation angle, enhanced convection due to wind possible, wind speed of 0.9 m/s during test
Sidewall Conduction Loss	61	0	900	Nominal loss does not include conduction loss from back of reactor.
Total Receiver Heat Loss	1289	1149	2579	Max and min values for receiver losses.
Receiver Efficiency	89.0%	90.2%	78.1%	Nominal and expected receiver efficiency estimate
Concentrator Efficiency	83.7%	86.2%	81.2%	ρ = 93%, ϕ = 90% (reflectance and intercept)
Collector Efficiency	74.4%	77.8%	63.4%	65.4% efficiency measured

The predicted solar reflection loss and infrared radiation losses were relatively certain, especially compared with cavity convection and conduction losses. Based on the measured collector efficiency of 65.4%, conduction losses needed to be at least 500 W and was expected to be much higher. Addressing the high apparent conduction losses by the use of high performance insulation, and/or incorporating radiation shields was recommended for Phase 2 work.

The analysis also suggested that the potential to improve system efficiency through a better dish collector was significant. By improving the dish collector, receiver intercept can be improved from 90% to nearly 100%. Improved optical accuracy would also lead to a higher solar concentration ratio as well as a more uniform reactor temperature and improved performance.

4.1.3 Finite Element Reactor Modeling

Throughout the three phases of this project, high fidelity finite element (FE) analyses were performed to model the steam methane reforming reactor to evaluate various design options. The effects of reactor geometry, channel configuration, and non-uniform solar flux distribution on reaction conversion, temperature distribution, and thermos-mechanical stress were studied. The results were used to improve the reactor design over each iteration from TRL 4 to TRL 6. The FE models were implemented using COMSOL Multiphysics® software.

4.1.3.1 Reactor Model Description

The finite element model was developed using COMSOL Multiphysics® with the heat transfer, flow in porous media, and reacting flow modules. In Phase 1, a slice of reactor was modeled based on circular symmetry. In Phase 2 and 3, the entire reactor geometry was modeled in three dimensions to full field analysis of temperature and stress in the reactor. Whole reactor model was necessary because axisymmetry is always lost with realistic solar flux input: the imperfections on the dish concentrator mirror produced "hot" spots on the reactor surface.

Domain Settings

A wireframe of the TRL 5 reactor geometry is shown in Figure 4-1 as an example. Methane and steam enter the reactor through the tube located at the bottom center of the device. The reactants then flow from the center toward the periphery of the device through catalyst channels (catalyst foam) located under the top plate of the reactor. The reacted synthesis gas then flows down to recuperation channels located just below the catalyst channels, and in these recuperation channels gas flows back toward the center of the device in counterflow to the reaction channels. The recuperation channels combine and synthesis gas flows through a short channel located in the wedge shaped region without catalyst channels and is channeled out through the exit tube.

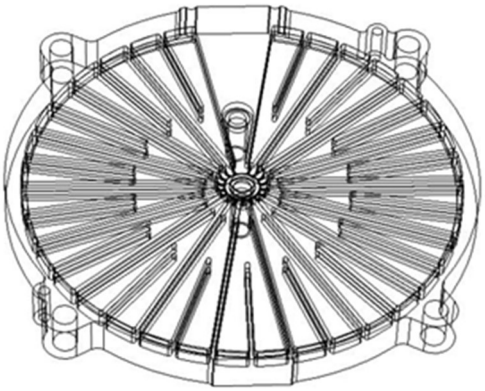

Figure 4-1 Wireframe of TRL 5 reactor/receiver geometry used for finite element model.

A description of the finite element model can be found in our previous publication [1]. In the model, Darcy's law with a temperature dependent density is used to describe convective flow through the reactor; heat transfer is modeled using convection/conduction equations with a heat sink tied to the rate of methane steam reforming and water gas shift reactions. A first order temperature dependent rate expression is used for the MSR reaction with the activation energy and pre-exponential factor fit using experimental data from experiments and data from our SMR reactor. The activation energy and pre-exponential factor was fit using laboratory data for the catalyst. Since the actual catalyst loading can differ between the laboratory tests and the felts used in the SMR reactor, the laboratory data was used as the starting point and the pre-exponential factor was adjusted such that the finite element model was in agreement with on sun experiments. The water gas shift rate expression was taken from the literature [2].

Darcy's Law was used to describe flow thorough the device in the porous catalyst and in the open recuperation channels by assigning different permeability to the different flow regions. This simplification was necessary since solving for the actual flow distribution in the open channels greatly increased model complexity; the required computational effort exceeded the capacity of the computer used for this study. Similar approximation was made to the heat transfer in portions of the modeled geometry representing high temperature alloy: the energy balance was described using a heat conduction equation without the convective transport and source terms and with a zero void fraction. Constants and material parameters used in the model are shown in Table 4-2.

Table 4-2 Values of constants used in the finite element model

Constant	*Description*	*Value*
K	Catalyst bed permeability	1e-10 m^2
$K2$	Open channel permeability	1e-9 m^2
M	Gas viscosity	1e-4 Pa s
D_{gas}	Gas phase dispersion constant (all species)	1e-3 cm^2/s
k_o	Pre-exponential factor for methane steam reforming kinetic expression	4.093 x 10^5 s^{-1}
k_1	Pre-exponential factor for water gas shift kinetic expression	4.9 x 10^9 s^{-1}
E_{msr}	Activation energy for methane steam reforming	93 kJ/mol
E_{wgs}	Activation energy for water gas shift reaction	145 kJ/mol
k_{bed}	Thermal conductivity of catalyst channel	0.73 W/(m K) *
k_{metal}	Thermal conductivity of metal	20 W/(m K) **
$C_{p,g}$	Gas specific heat	1000 J/(kg K)

*Hastelloy X at 600°C; different values were used when modeling reactors construction of other alloys.
** FeCrAlY catalyst support foam.

Boundary Conditions

In the methane steam reforming simulations the water to methane molar ratio was specified at the entrance to the device by setting the methane and water concentrations. The temperature of the gas entering the device, inlet flow velocity and exit flow pressure was also specified. The solar flux was specified using results from moon tests (see Section 4.3.1.3). This heterogeneous flux map was imported into COMSOL as an interpolated function. The magnitude of the flux was scaled such that a desired average flux was achieved. Conductive and convective heat losses from the reactor were also incorporated into the model. On-sun experiments have provided an idea of the magnitude of these heat losses, but not the exact location. In the simulation the convective heat loss from the top of the reactor was modeled by decreasing the incoming flux. The conductive losses on the back and sides of the reactor were specified as a constant outward heat flux term on these surfaces, as well as the heat loss from the rods supporting the reactor when applicable.

Mass and Energy Balance of Reactive Flow

The gas velocity obtained from Darcy's law is used in the convective flux term of the mass balance equation for each species [Eq. 1].

$$\varepsilon \frac{\partial c_i}{\partial t} + \nabla \cdot (-\varepsilon \cdot D_{i,gas} \nabla c_i - c_i \cdot \vec{v}) = Rate_i \tag{1}$$

The dispersive term in Eq. 1 describes gas phase diffusion and dispersion arising from mixing in the inter-particle flow paths. The source term ($Rate_i$) represents the creation or destruction of species *i* due to the methane steam reforming (subscript *msr*) reaction [Eq. 2] and the water gas shift (subscript *wgs*) reaction [Eq. 3].

$$CH_4 + H_2O \leftrightarrow CO + 3H_2 \tag{2}$$

(3)

$$CO + H_2O \leftrightarrow CO_2 + H_2$$

The methane steam reforming rate expression [Eq. 4] is a first order expression developed for a metal substrate catalyst developed at Pacific Northwest National Laboratory [3]. The water gas shift rate expression [Eq. 5] was taken from literature [2].

$$Rate_{msr} = \left[c_{CH_4}\right] \cdot k_o \exp\left[\frac{-E_{msr}}{RT}\right] \tag{4}$$

$$Rate_{wgs} = k_1 \exp\left[\frac{-E_{wgs}}{RT}\right] \cdot \left[c_{CO} - \frac{c_{CO_2} \cdot c_{H_2}}{\exp\left(\frac{2073}{T} - 2.029\right) \cdot c_{H_2O}}\right] \tag{5}$$

An energy balance equation that includes convection and conduction is used to model heat transfer in the catalyst bed [Eq. 6]. This equation reduces to a conduction equation in the solid metal portions of the modeled reactor section. In the derivation of this equation it is assumed heat transfer between the solid and gas phase is fast enough such that temperature equilibrium is achieved and a single temperature at each point in the porous catalyst support can be used for both the gas and solid phase.

$$\begin{aligned}&\left((1-\varepsilon)\rho_s C_{p,s} + \varepsilon\rho_g C_{p,g}\right)\frac{\partial T}{\partial t} + \nabla \cdot \left(-\mathrm{k}\nabla T\right) + \rho_g C_{p,g}\vec{v} \cdot \nabla T \\ &= q_{msr} \cdot Rate_{msr} + q_{wgs} \cdot Rate_{wgs}\end{aligned} \tag{6}$$

From Eq. 2 and Eq. 3 it can be shown that:

$$Rate_{CH_4} = -Rate_{msr} \tag{7}$$

$$Rate_{CO} = Rate_{msr} - Rate_{wgs} \tag{8}$$

$$Rate_{CO_2} = Rate_{wgs} \tag{9}$$

$$Rate_{H_2O} = -Rate_{msr} - Rate_{wgs} \tag{10}$$

$$Rate_{H_2} = 3 \cdot Rate_{msr} + Rate_{wgs} \tag{11}$$

These species rate equations [Eq. 7 – Eq. 11] are combined with Eq. 4 and Eq. 5 and incorporated into the mass balance equation [Eq. 1] for each species in the simulation. These five mass balance equations along with the energy balance Eq. 6 and Darcy's Law make up the mathematical description.

4.1.3.2 Reactor Modeling Results

Internal Heat Recuperation

Internal heat recuperation was a critical consideration in the reactor design. The flow channels inside the reactor were configured such that hot product streams exiting the catalyst channels flow counter-currently to the reacting flow streams in the bed. The heat recuperation lowers the product stream temperature so that less expensive alloy can be used in downstream heat exchangers. However, the

primary benefit is a better energy conversion efficiency because more heat is used to drive the endothermic reaction. Early analysis work in Phase 1 on a one-sixth of reactor model space confirmed that a significant amount of heat is transferred from the outgoing stream to the catalyst channels with this arrangement.

In Figure 4-2 the temperature profiles through the entire reactor thickness at various radial locations are shown for the TRL 4 and TRL 5 reactors modeled with the top surface receiving a homogeneous solar flux totaling 8 kW. In reality the solar heat flux will have non-uniformities and will likely fall off toward the outside edge of the reactor and the center of the reactor. However, this departure from reality used for this modeling study is useful for understanding the heat transfer within the device, and where heat flow is constrained. The temperature profiles for both reactors show active internal heat recuperation along the catalyst bed (2 to 12 cm radial distance). It is also clear from the profiles that the 60% thinner TRL 5 top plate resulted in a 90-100°C reduction of the surface temperature compared to the thicker TRL 4 reactor.

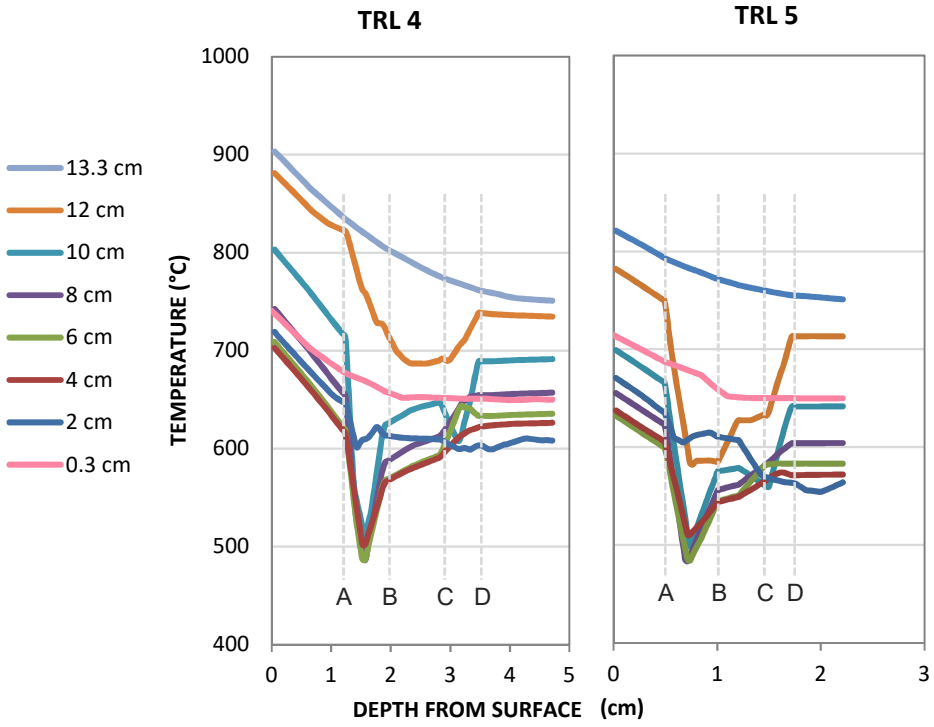

Figure 4-2 Comparison of TRL 4 and TRL 5 reactor temperature profiles (A to B: reaction channel; C to D: heat recuperation channel).

Thermal Spreading of Inhomogeneous Solar Flux

The incident solar flux at the reactor surface was distributed non-uniformly because of imperfections in the concentrator reflector panels. Some local hot spots are inevitable even with the best concentrators, thus it is important that the solar thermochemical reactor is able to cope with the hot spots. Localized hot spots are detrimental to the reactor performance in two important ways. First of all, an excessive operating temperature reduces the reactor rupture life time. Secondly, it is believed that the reaction channel under the hot spots tend to have higher methane conversion, resulting in higher product stream

velocities. This would force more reactant to flow into colder channels and leave the hotter channel even hotter. The end result would be lower overall chemical conversion.

Mitigation of the hot spots depends on the thermal spreading ability of the reactor, which depends on the reactor plate thickness. Table 4-3 summarizes the key dimensions of a number of reactor configurations that were modeled. The modeling results showed that a thicker top plate promoted better thermal spreading. However, a thicker top plate such as the one in the TRL 4 reactor resulted in large temperature differences between the receiver surface and the reaction channel, making it difficult to operate below the alloy temperature rating at high solar flux. As will be shown in the next section, the rigidity of the reactor and the resulting thermal stress are also sensitive to plate thickness. For the above reasons it is critical to perform multi-physics modeling in order to evaluate a particular set of design dimensions. In Figure 4-3, the surface temperature results from several reactor designs are shown.

Table 4-3 Reactor plate thickness and channel heights analyzed by reactor modeling.

Reactor	*TRL 4*	*TRL 5 Mesochannel*	*TRL 5 Microchannel*	*TRL 6 Mesochannel*
Top Plate Thickness	0.500” (12.7)	0.200” (5.08)	0.110” (2.79)	0.175” (4.45)
Reaction Channel Height	0.250” (6.35)	0.250” (6.35)	0.040” (1.02)	0.210” (5.33)
Separation Plate Thickness	0.375” (9.52)	0.125” (3.18)		0.040” (1.02)
Return Channel Height	0.250” (6.35)	0.200” (5.08)	0.040” (1.02)	0.080” (2.03)
Back Plate Thickness	0.500” (12.7)	0.200” (5.08)	0.080” (2.03)	0.055” (1.40)

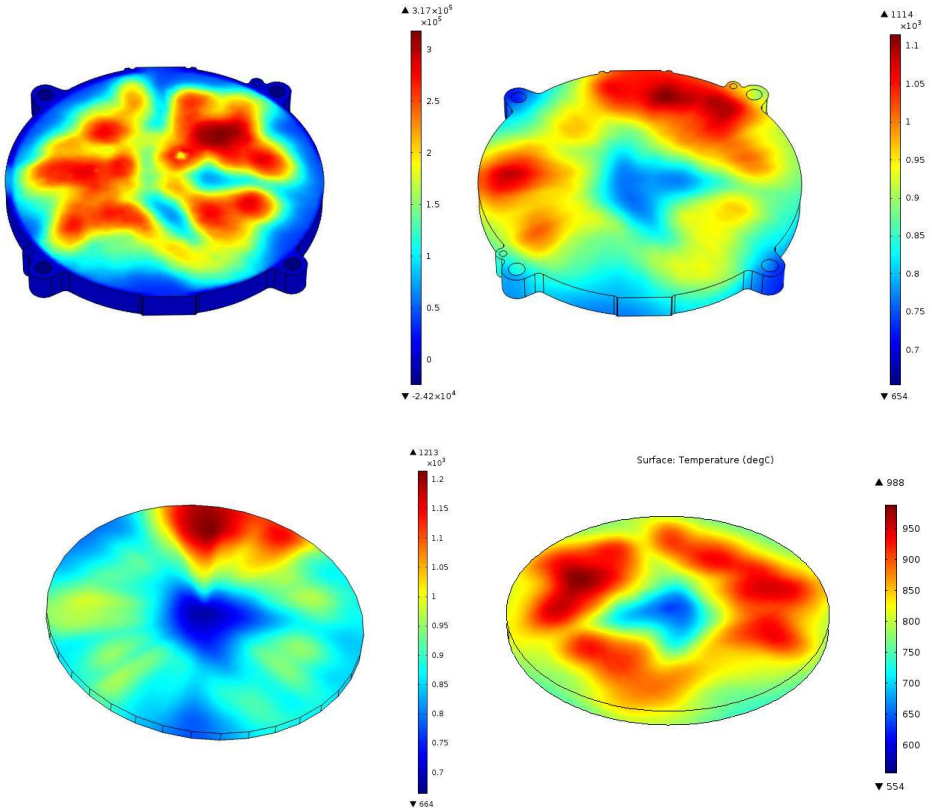

Figure 4-3 Inhomogeneous heat flux and simulated reactor surface temperature fields (Note: color bar scales are different for each subplots; **top left**: heat flux distribution used in modeling

boundary conditions, scaled from a measured moon flux map with the actual parabolic dish, unit: watts/m^2; **others**: reactor surface temperature distribution at high flux high conversion conditions, 9.6 kW solar total and >80% conversion, 0.032 mol/s CH_4 flow, steam to carbon ratio of 3; **top right**: TRL 5 mesochannel geometry; **bottom left**: TRL 5 microchannel geometry; **bottom right**: TRL 6 mesochannel geometry).

In these simulations, an inhomogeneous flux distribution was applied to the reactor front surface as boundary condition. This flux distribution was based on the flux map obtained from a moon test on the actual dish concentrator. Among the reactor geometries modeled, the TRL 5 and TRL 6 mesochannel versions were built out to physical prototypes. The TRL 5 microchannel version was evaluated by simulation only. The difference between TRL 5 meso- and micro-channel versions was in plate and channel thickness: the microchannel geometry had much thinner dimensions. The TRL 6 mesochannel version had slightly thinner plates and smaller channels than TRL 5 mesochannel version. However, the internal channel geometry in TRL 6 was designed very differently to optimize thermal spreading. While the details of this design will not be disclosed in this report due to pending patent application, the thermal spreading performance can be compared here.

The microchannel design (bottom left image in Figure 4-3) had a reduced thermal spreading ability than the mesochannel design (top right image). The maximum temperatures with the thinner plates in the TRL 5 microchannel design were just over 1200°C, about 100°C higher than the TRL 5 mesochannel case with thicker plates. The thinner top plate was not able to provide enough thermal spreading next to the hottest spots where the most intense solar flux was. The improvements in TRL 6 channel structure were able to reduce the maximum surface temperatures by about 100°C from the TRL 6 mesochannel case even though the TRL 6 plate thickness was 25% thinner. This result contributed to the selection of the novel TRL 6 design as the final prototype. As will be shown in the next sections, the thermal stress and reaction performance were also important factors in the design tradeoff. Nonetheless, the improvement to thermal spreading by the TRL 6 structured channel configuration was one significant achievement.

In these simulations, an inhomogeneous flux distribution was applied to the reactor front surface as boundary condition. This flux distribution was based on the flux map obtained from a moon test on the actual dish concentrator. Among the reactor geometries modeled, the TRL 5 and TRL 6 mesochannel versions were built out to physical prototypes. The TRL 5 microchannel version was evaluated by simulation only. The difference between TRL 5 meso- and micro-channel versions was in plate and channel thickness: the microchannel geometry had much thinner dimensions. The TRL 6 mesochannel version had slightly thinner plates and smaller channels than TRL 5 mesochannel version. However, the internal channel geometry in TRL 6 was designed very differently to optimize thermal spreading. While the details of this design will not be disclosed in this report due to pending patent application, the thermal spreading performance can be compared here.

The microchannel design (bottom left image in Figure 4-3) had a reduced thermal spreading ability than the mesochannel design (top right image). The maximum temperatures with the thinner plates in the TRL 5 microchannel design were just over 1200°C, about 100°C higher than the TRL 5 mesochannel case with thicker plates. The thinner top plate was not able to provide enough thermal spreading next to the hottest spots where the most intense solar flux was. The improvements in TRL 6 channel structure were able to reduce the maximum surface temperatures by about 100°C from the TRL 6 mesochannel case even though the TRL 6 plate thickness was 25% thinner. This result contributed to the selection of the novel TRL 6 design as the final prototype. As will be shown in the next sections, the thermal stress and

reaction performance were also important factors in the design tradeoff. Nonetheless, the improvement to thermal spreading by the TRL 6 structured channel configuration was one significant achievement.

Thermal Stress

In Phase 2 and 3, COMSOL Multiphysics was used to perform a temperature dependent structural analysis of the reactor conceptual designs to gain a better understanding of thermally induced stresses. The model used COMSOL's Solid Mechanics module along with the Heat Transfer module. These were coupled to model the thermal expansion of the SMR during operation. The coefficient of thermal expansion was set to 15.6×10^{-6} 1/K, and the materials modulus was set to 161×10^{9} Pa (typical properties of Hastelloy X at 700°C). The temperatures calculated using the previously described reacting flow model were used as input to the structural mechanics model. Figure 4-4 shows the calculated stress in the SMR reactor for the temperatures simulated for the high-flux high-conversion case same as for the temperature results in Figure 4-3.

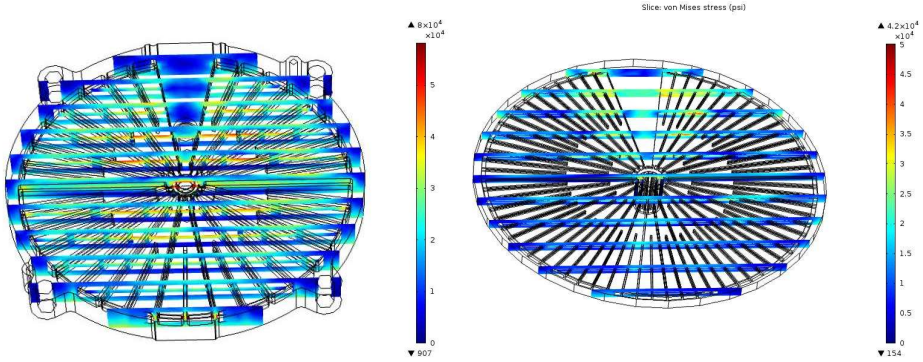

Figure 4-4 Simulated thermal stress in TRL 5 mesochannel (left) and microchannel (right) designs under high flux high conversion conditions (domain min and max von Mises stress shown next to color scale bars).

As can be seen in Figure 4-4, the thermally induced stresses can be very large. The maximum stresses calculated for the TRL 5 mesochannel design approached 80 ksi (the plot on the left in Figure 4-4). These high stress regions corresponded to portions of the reactor near hot spots and adjoin the wedge with no flow channels. The largest stresses were in the wall separating the reaction channels from the recuperation channels. This wall was lower in temperature compared to the top surface, but may still approach temperatures around 800°C. The high stresses in this wall were a result of the displacement caused by the hot top plate being constrained by the cold bottom plate. This tended to make the reactor bow like a potato chip and place stresses on the wall separating the reforming and recuperation channels. One method for reducing these stresses is to decrease the thicknesses of the top and bottom plates. This makes the reactor less stiff, enabling deformation without inducing high stress. Thinner thicknesses also reduce the amount of high temperature alloy used, and heat losses due to conduction through the metal. However, competing considerations are that the use of thinner plates reduces the spans that can be supported at a given pressure (can reduce pressure capability) and reduces heat spreading effects.

The von Mises stress plot on the right side of Figure 4-4 was simulation results on the TRL 5 microchannel design with thinner plates. Although this case had higher overall temperatures compared to

the mesochannel case (Figure 4-3), the highest stress levels were half of those seen with the thicker mesochannel geometry. In both cases, the highest stress levels were seen in the plate separating the reforming and recuperation channels in areas adjacent to the region of the reactor without reforming channels. These areas also corresponded to the hottest portion of the reactor. The above results show that moving toward a thinner reactor structure and the use of microchannels has the anticipated beneficial effect on thermally induced stress. However, the earlier discussion related to Figure 4-3 shows a less than desired impact on reactor temperature with the use of microchannels. Part of this was due to the decreased amount of catalyst and shorter residence time inherent in the use of microchannels.

The latest TRL 6 reactor with the improved channel configuration was also modeled to evaluate thermal stress. The reactor detailed geometry is not disclosed in this report due to pending patent application, thus a similar plot of stress overlay on channel structure for the TRL 6 reactor is not included in Figure 4-4. However, the range of the thermal stress can be reported: maximum stress in the TRL 6 design was lower than the TRL 5 design but slightly higher than the microchannel design. Combined with the desirable thermal spreading shown earlier, the TRL 6 design with the special channel configuration offered the best performance when temperature field and thermal stress are both considered.

Chemical Conversion Performance

The finite element model was used to examine the performance of the TRL 5 reactor geometry. Two test cases corresponding to high conversion and low conversion experimental results were chosen to examine if the simulation accurately predicts performance. Table 4-4 shows the experimental results along with model predictions. These results indicate that the finite element model did a good job predicting the conversion for a given inlet flowrate and solar flux. The largest discrepancy was the outlet temperature for the low conversion case. However, this could be explained by differences in the distribution of the solar flux and heat losses.

Table 4-4 Comparison of TRL 5 reactor experimental results with the finite element model.

Description	*Methane Conversion*	*Temperature In (°C)*	*Temperature Out (°C)*	*Solar Flux (kW)*	*CH_4 Flow (mol/s)*	*Steam /Carbon*
	Low Conversion Experiment 2014-11-07					
Measurement	0.207	556.3	651.77	4.45	0.0518	2.49
Model Output	0.200	556	602	4.45	.0508	2.57
	High Conversion Experiment 2014-11-17					
Measurement	0.8782	664.5	692.4	3.855	0138	2.99
Model Output	0.866	664	698.4	3.842	0.01385	2.99

The reactant concentration distribution from the simulations are shown in Figure 4-5 for both the TRL 5 meso- and micro-channel geometries. Some distribution in the methane conversion existed from channel to channel. The source of the variations was the spatial fluctuations of the flux distribution: some channels intercepted more solar flux, became hotter, and had higher methane conversions. The simulation results show that the reactors had the ability to cope with the inhomogeneous solar fluxes. This was in part because of the ability of channels with high solar flux to absorb additional heat by means of the reverse water gas shift reaction as well as sensible heating. For the microchannel geometry, the reduced channel dimensions led to a decreased amount of catalyst and shorter residence time. This caused larger variations in methane concentration from channel to channel. This finding led to a TRL 6

reactor design decision to increase the catalyst loading per unit volume to compensate the smaller channels.

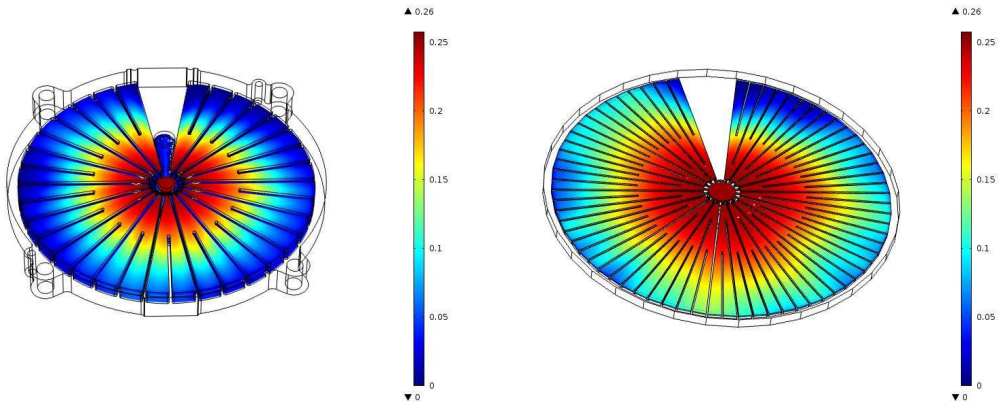

Figure 4-5 Simulation results showing methane mole fraction in the TRL-5 reactor for a high flux high conversion condition (left, mesochannel geometry; right, microchannel geometry).

4.1.4 Catalyst Durability Studies

Experimental catalyst durability studies were performed in Phase 1 to understand the limitations of a rhodium-based ("benchmark") catalyst by evaluating the effect of key process variables such as temperature and steam-to-carbon (H_2O/C) molar feed ratios on catalytic performance. A natural gas simulant (94.5% CH_4, 4.0% C_2H_4, 1.0% CH_3H_6, and 0.5% C_4H_{10}) was used as model feed. During Phase 2, the durability studies were extended to longer durations. In addition, a number of additional catalyst formulations with the potential for improved performance and/or decreased cost were also investigated. Rh-based catalysts with varying metal loadings, Ir-based catalysts, and IrNi and RhNi bimetallic catalyst formulations developed under prior research programs were explored with the potential for enhanced catalyst durability. Furthermore, a catalyst regeneration approach was successfully identified.

4.1.4.1 Benchmark Rh Catalyst Stability

Stability investigations for CH_4 steam reforming were initially performed at temperatures between 700 and 900°C for 24 hour durations and operating with a steam-to-carbon ratio of 2. The contact time was chosen to ensure equilibrium conversion for each run. No catalytic deactivation was observed in these short term (24 hour) stability tests at operating temperatures of 500 to 850°C. At 900°C some deactivation was observed.

Catalyst durability was then evaluated for longer duration 100 hour tests. The results are shown in Figure 4-6. At a relatively high operating temperature of 850°C stability was evaluated as a function of molar steam-to carbon feed ratios ranging from 1.5 to 4.0. All of the runs exhibited relatively stable results for an initial period of approximately 30 hours. However, after running for approximately 100 hours, slight deactivation of the catalyst was observed. On the contrary, when operating at 700°C, conversion was quite stable for the duration of the run. The stability of the benchmark Rh catalyst was further studied in Phase 2 for longer durations.

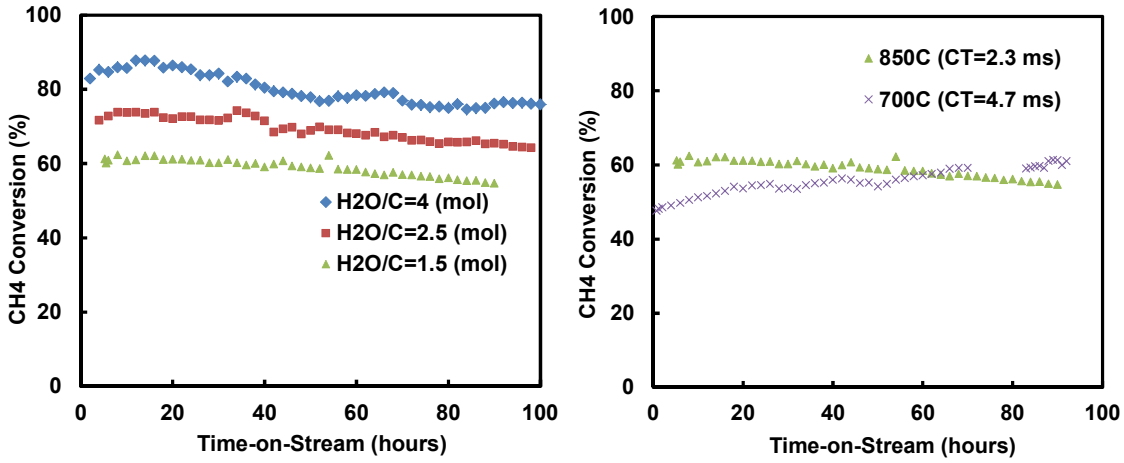

Figure 4-6 Methane conversion 100 hours stability profile (left, variable S/C, 850°C, 2.3 ms contact time, 1 atm; right, variable temperature, S/C = 1.5, 1 atm).

4.1.4.2 Catalyst Stability under Bi-Reforming Conditions

The combination of steam methane reforming and dry reforming with CO_2 is called bi-reforming. The individual and net reactions involved in bi-reforming are listed below.

$CH_4 + H_2O \rightarrow CO + 3H_2$ $\Delta H = 206$ kJ/mol Steam Reforming (12)

$CH_4 + CO_2 \rightarrow 2CO + 2H_2$ $\Delta H = 247$ kJ/mol Dry Reforming (13)

$CO + H_2O \rightarrow CO_2 + H_2$ $\Delta H = -41$ kJ/mol Water-Gas-Shift (14)

$2CH_4 + CO_2 + H_2O \rightarrow 3CO + 5H_2$ Bi-reforming (15)

In Phase 1, a preliminary evaluation of the benchmark Rh catalyst for bi-reforming conditions was performed at 850°C, atmospheric pressure, a feed molar ratio of 2.5:1.0:2.0 ($CH_4/CO_2/H_2O$). The effect of contact time was investigated at a constant molar feed ratio of 1.2 for $(H_2O+CO_2)/CH_4$. The results indicated that under these conditions—with a particular feed blend of natural gas, CO_2, and H_2O— the catalyst stability was relatively favorable when operating at 800°C. However, at 850°C rapid catalytic deactivation became problematic. Thus, careful temperature control is important. It was also found that CH_4 conversion slightly decreased with the addition of CO_2 to the feed.

4.1.4.3 Effects of Rhodium Loading on Catalyst Performance

In Phase 2 various rhodium metal loadings with the same $MgAl_2O_4$ spinel support were investigated. A reduced amount of precious metal loading is attractive for economic considerations. Catalytic activity was evaluated at 600 to 850°C for catalysts with 2.5%, 5%, 10%, and 20% Rh metal mass loadings. As illustrated in Figure 4-7 the catalyst activity increased with metal loading. When operating at 850°C the contact time was decreased from 4.5 ms to 2.3 ms in order to ensure kinetic control and to further accelerate aging effects. It should be noted that this temperature (850°C) and S/C ratio (1.5) presented relatively severe process conditions that induce carbonaceous deposition of the catalytic active sites (e.g., catalyst coking). It can be seen in Figure 4-7 that the 2.5% metal loading exhibited poor catalytic stability

as compared to the 5%, 10%, and 20% metal loadings. The difference in stability was attributed to structure sensitivity. That is, the 2.5% Rh catalyst had smaller average crystal structures. Coking reactions could be facilitated by uncoordinated active sites (e.g., step and edge sites) more prevalent with smaller crystal sizes.

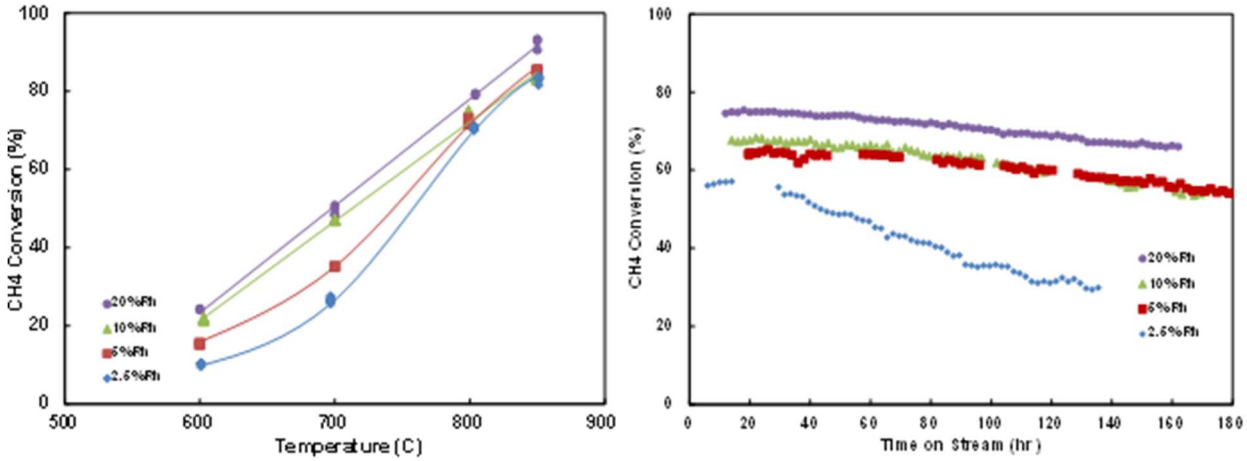

Figure 4-7 Methane conversion obtained with different Rh catalyst loadings at steam to carbon ratio of 1.5 (**left**, as a function of temperature; **right**, as a function of time-on-stream at 850°C and residence time from 4.5 to 2.3 ms).

4.1.4.4 Rh Catalyst Durability at High S/C Ratio

Select catalysts were evaluated for prolonged duration at a higher steam to carbon ratio of 3 in the feed stream. Prior experiments had been performed at S/C of 1.5. With the higher S/C feed ratio there was some deactivation observed for all of the catalysts evaluated, albeit to a lesser degree. Thus, the catalytic deactivation mechanism was believed to primarily stem from coking. Key results are illustrated in Figure 36 where it can be seen that the benchmark catalyst is more stable when operated with increased S/C feed ratio.

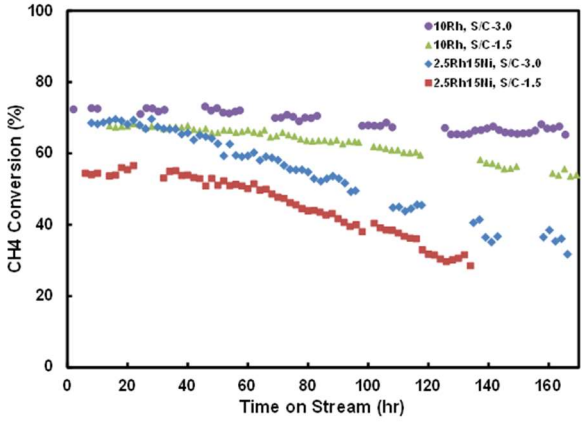

Figure 4-8 Methane conversion as a function of time-on-stream at increased S/C ratio of 3 (850°C, 1 atm, and 2.3 ms residence time).

Regardless, the results provide justification in using a catalyst with a minimum rhodium loading that is necessary for enhancing catalytic stability. However, increasing metal loading, at least up to 20% Rh, offers increasing kinetic activity with negligible difference in catalyst stability. Trade-off in the activity requirements for the integrated solar thermochemical device and economics could dictate what metal loading is ultimately utilized

4.1.4.5 Effects of Methane vs. Natural Gas Feeds

Experiments were also performed when using methane in lieu of the natural gas simulant. This was done in order to elucidate the effects that the higher hydrocarbons (e.g., ethane, propane, butane) present in the natural gas simulant have in facilitating coking reactions as compared to with methane alone. Not surprisingly, deactivation was mitigated when using only methane (and water) as reactant. It should be noted that prior studies utilizing pure methane as feed yielded more stable results. It is well known that higher hydrocarbons – present in this study - induce coking to a greater extent as compared to methane alone. However, deactivation still occurred for all of the catalysts investigated. The culmination of all of the tests, which include varying S/C feed ratio, temperature, and hydrocarbon feed type, suggest that high temperature of operation (> 800°C) is problematic for all of the catalysts investigated. Thus, future stability investigations will take place at reduced operating temperatures in order to understand the upper operating temperature limit, particularly if lower S/C feed ratios than 3 are desired.

4.1.4.6 Evaluation of Bimetallic Rh-Ni Catalysts

Bimetallic RhNi-based catalysts were also investigated for catalytic performance. Rhodium is known to be both more active and stable than nickel for methane steam reforming, albeit significantly more costly. However, previous research programs at PNNL found that combining Rh and Ni together offered stability enhancement for systems employing methane conversion in the presence of tars (i.e., polyaromatic hydrocarbons). In Phase 1 one RhNi-bimetallic catalyst was evaluated and results provided successful proof of concept for natural gas steam reforming. In Phase 2 multiple RhNi bimetallic formations were tested and also evaluated under longer time durations. The bimetallic catalyst initially did appear to offer enhanced stability as compared to the benchmark catalyst. However, when evaluating under prolonged time durations (e.g., 160 hours) and when operating at a high temperature of 850°C, deactivation was observed. Due to the lack of stability enhancement at the target conditions, development of the RhNi bimetallic formulations were not continued.

4.1.4.7 Evaluation of Ir-Based Catalysts

In prior research at PNNL it was found that Ir was more active than Rh for methane steam reforming at operating temperatures greater than 600°C on a turnover per site basis. Thus, Ir catalysts with varying metal loadings were evaluated at 850°C, 1 atm, S/C=1.5, and 4.5 ms contact time. All of the Ir-based catalysts studied were found to have less activity than the benchmark Rh-based reforming catalyst. Additional investigation showed that while Ir is more active than Rh for methane steam reforming, they are less active for higher hydrocarbon steam reforming (e.g. ethane). Furthermore, these Ir-based catalysts did not appear to offer improved catalytic stability. In prior research at PNNL it was also found that IrNi bimetallic catalysts offered stability enhancement for methane steam reforming in the presence of tars. Thus, IrNi bimetallic formulations were also investigated in this work. Similar to Ir-alone they

were not found to offer any activity or stability benefit under conditions of this study. No further investigation of Ir or IrNi catalyst formulations was carried out.

4.1.4.8 500-Hour Stability Evaluation

The benchmark Rh catalyst was operated at 750°C for 500 hours in a prolonged duration demonstration (see Figure 4-9, left). Slight deactivation in CH_4 conversion from approximately 50% to 43% was observed after the first 300 hours' time-on-stream. Then the catalyst was stable without any observable deactivation for an additional 200 hours' time-on-stream. The 500-hour stability test was repeated at 800°C (Figure 4-9, right). At the higher operating temperature, conversion only slightly decreased from approximately 88% to 85% after 300 hours' time on-stream. A rapid climb of reactor back pressure at this point indicated coke build-up. The catalyst was then regenerated under a mild oxidation treatment. After the regeneration, the pressure build-up disappeared and the catalyst regained most of the activity back. This demonstrated a successful application of a catalyst decoking procedure. These results, together with those from Phase 1, suggest that catalytic performance for the benchmark catalyst can be quite stable provided the operating temperature does not exceed 750-800°C. Furthermore, if coke build-up of the catalyst occurs, a regeneration approach developed here can be applied.

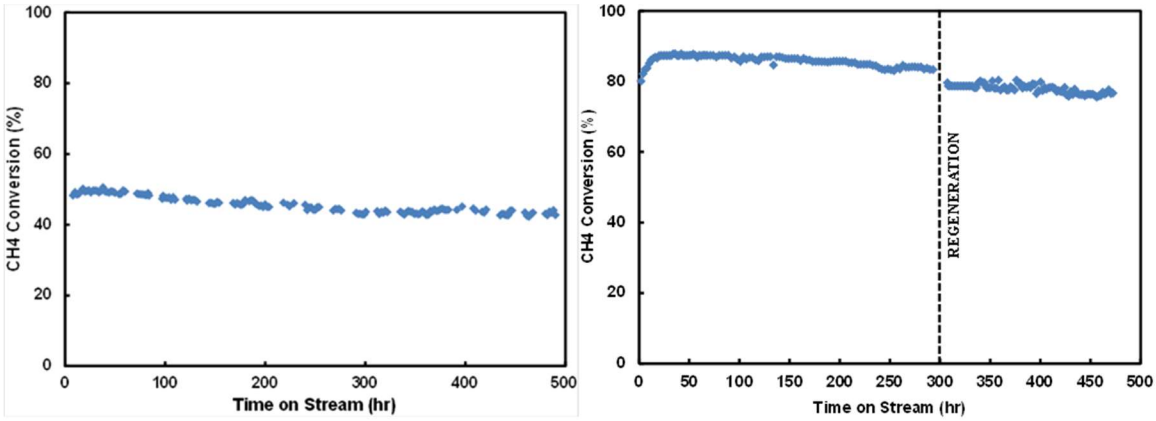

Figure 4-9 Methane conversion 500 hours stability profile operating at S/C=2 and 1 atm (**left**: 750°C; **right**: 800°C).

4.2 Reaction System Fabrication

Three generations of prototype reaction systems ranging from TRL 4 to TRL 6 were evaluated under this program. The design approach has been described in the previous section. This section focuses on the fabrication methods and issues relevant to the selected designs. The reactor and heat exchanger fabrication are described in more details in subsections. The following is a brief summary of the evolution of the reaction systems. In Phase 1, a new high temperature recuperator was fabricated by additive manufacturing using Inconel 625 alloy. The new recuperator was combined with the Haynes 230 solar SMR reactor that had been fabricated on a previous project. The resulting reaction system was tested on-sun at TRL 4 level.

The TRL 5 reactor design was started in Phase 1 and finished in Phase 2. Improvements included to optimize the plate thickness so that reactor mass was reduced while maintaining working pressure and

temperature ratings. Reactor materials was changed to Hastelloy X with a tradeoff of some high temperature strength for decreased material cost. The reactor was also re-designed to reduce the complexity of assembly and the fabrication time. The number of parts on the TRL 5 reactor was reduced from 9 on the TRL 4 version to only 5 parts (see Figure 4-10). Machining from both side of a plate was avoided. The total weld length was also reduced. A reactor prototype was fabricated in Phase 2 to this new design using the same CNC machining and diffusion bonding process used for the TRL 4 reactor. A set of new recuperative heat exchangers were fabricated out of Inconel 625 by additive manufacturing with an updated design. These new reactor and exchangers were assembled into a TRL 5 reaction system and tested on-sun in Phase 2.

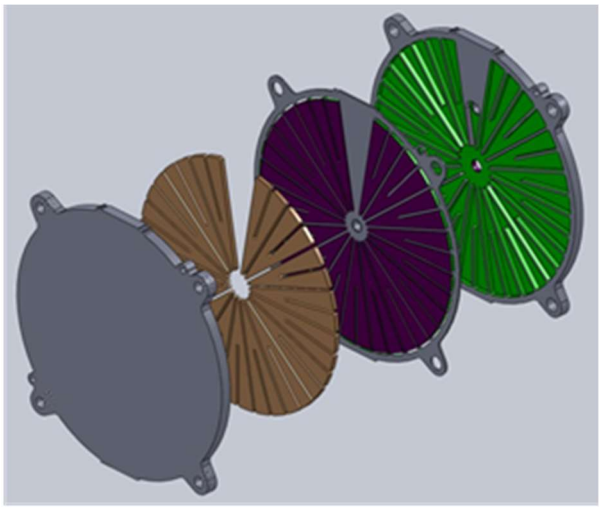

Figure 4-10 Phase 2 TRL 5 steam methane reforming (SMR) reactor design showing the machined channel (green) and the catalyst insert (brown).

Additional improvements were made to reactor design in Phase 2: plate thickness was further reduced and a novel flow channel structure was developed to enhance internal heat recuperation. Based on previous analysis and on-sun performance tests, Haynes 230 was re-selected as the best material of construction for the new TRL 6 reactor. The reactor was fabricated similarly by conventional CNC plate milling and diffusion bonding. New Inconel 625 recuperative heat exchangers were again fabricated by additive manufacturing with designs updated for TRL 6 reactor. The new components were assembled into the TRL 6 reaction system and tested on-sun in Phase 3. Some key components in the TRL 4 to TRL 6 reaction systems are listed in Table 4-5 with basic fabrication information. More detailed description of the fabrication steps are given in subsections that follow.

Table 4-5 List of some fabricated reaction system components.

	Reactor (CNC Milling, Diffusion Bonding)			*Recuperator HX (Additive DMLS)*
TRL 4	Haynes 230	22.0 kg	∅10.75”×1.875”	Inconel 625
TRL 5	Hastelloy X	8.65 kg	∅11.00”×0.975”	Inconel 625
TRL 6	Haynes 230	4.58 kg	∅11.00”×0.560”	Inconel 625

4.2.1.1 Steam Methane Reforming Reactor

The fabrication of SMR reactor prototypes was a multiple step process involving the fabrication of reactor plates and catalyst foam inserts, the assembly and bonding of the parts, finish machining and welding, and leak tests. It should be noted that the manufacturing process and costs for the production of the reactors at volume are the subject of a separate task for manufacturing development. Nonetheless, it is possible that the eventual manufacturing process may have at least some steps to those described here for the reactor prototypes tested in this project.

Reactor Plates

The reactor plates were fabricated from high temperature alloy by conventional machining processes. First, plate stocks were cut by abrasive waterjet into a net shape close to the finished outer profile (some small edge features needed for alignment during fabrication may be eventually cut off). The top and bottom faces of the cut plates were then ground by dual disc grinding to within surface roughness and parallelism tolerances. Next, the ground plates were machined by CNC mills to produce lateral flow channels as well as header openings at both ends of the channels. Shallow channel features may also be produced by photo chemical etching. Tube connection ports were welded to the middle and back plate after the above machining step. Photos of the TRL 5 reactor plates after machining are shown in Figure 4-11 as examples. These parts were ready for assembly and final bonding.

Figure 4-11 Photos of TRL 5 reactor front plate (left), middle plate (center), and back plate (right) after CNC machining.

Catalyst Foam

The solar steam methane reforming reactor used a rhodium-based catalyst supported on a metal foam. FeCrAlY alloy foams (Selee Corporation) were selected as the catalyst support material for good temperature properties, high surface area, and good catalyst adherence. The FeCrAlY foam product specification had a relatively loose thickness specification (±0.02”). Actual batches received were 0.213±0.002” in thickness. The stock foam boards were cut to net shape of channel inserts by wire electrical discharge machining. The freshly cut foam inserts were cleaned in a sonication bath of 50:50 acetone aqueous solution. The clean foam inserts were air dried and then calcined at 900°C for two hours.

Rhodium catalyst powder was prepared by incipient wetness impregnation of spinel $MgAl_2O_4$ by a rhodium (III) nitrate aqueous solution (Colonial Metals). The impregnated material was calcined and

made into a water slurry by ball milling. Foam inserts were dip-coated to desired mass loading with the catalyst slurry in special container conforming the insert shape, followed by a final calcination step.

Assembly and Bonding

The assembly and bonding of the reactor plates into a hermetic unit was performed by a diffusion bonding service vendor (Vacuum Processing Engineering). The plates were cleaned and coated with a thin layer of nickel by electrolytic plating. Catalyst inserts were installed into the reaction channels on the front plate. The component plates were then stacked in alignment. The stack assembly was diffusion bonded under a pressure load between graphite blocks inside a high vacuum furnace. After diffusion bonding, a helium leak check was performed to better than 10^{-9} std-cc/sec bond to verify hermetic bonds. Photos of the TRL 5 reactor plates during the assembly and diffusion bonding process are shown in Figure 4-12 as examples.

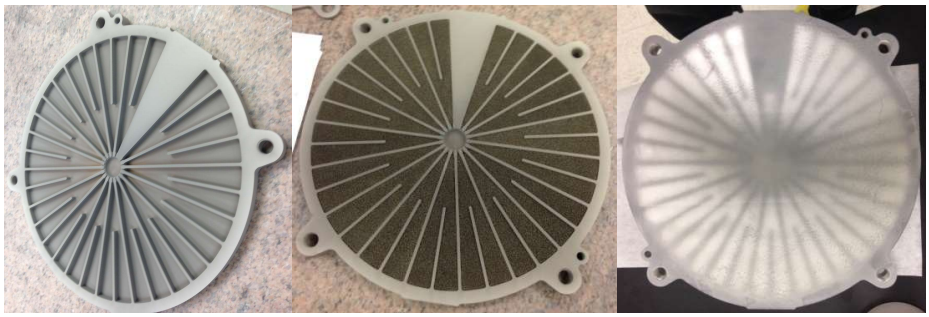

Figure 4-12 Photos of TRL 5 reactor plates during assembly and bonding (**left**, front plate after nickel plating; **center**, front plate with catalyst inserts; **right**, reactor front face after diffusion bonding).

4.2.1.2 Heat Exchangers

Direct metal laser sintering (DMLS), an additive manufacturing method, was chosen for the fabrication of the recuperative heat exchangers on the reaction systems. DMLS enabled rapid prototyping of these heat changers specifically tailored to match each generation of the SMR reactors under development, avoiding long lead times of the conventional approach using photochemical machining and diffusion bonding. During Phase 1, the high temperature recuperator (HTR) was re-designed with the constraints of manufacturability by the DMLS fabrication method. For example, overhangs greater than 45 degree angle from vertical cannot be built without support structure, which narrowed down the feasible build orientations of these heat exchangers to a few possibilities. Inconel 625 was chosen as the material of construction based on its high temperature properties and the capability of DMLS vendors.

Proof-of-concept microchannel test pieces were built to determine the minimum channel and wall thicknesses resolvable by DMLS. After build quality, hermeticity, means of powder removal were verified using subscale device builds, DMLS fabrication was determined to be viable for full scale heat exchangers. The high temperature recuperator and the additional recuperative heat exchangers operated at lower temperatures to preheat the water and methane stream were subsequently fabricated by DMLS additive manufacturing for each of the TRL 4, TRL 5, and TRL 6 reaction systems.

4.2.1.3 Reactor On-Sun Assembly

The on-sun unit of the reaction system consisted of the solar SMR reactor, recuperative heat exchanger network, and onboard process instrumentation. An electrical vaporizer was also part of the on-sun assembly for steam generation. The reactor, heat exchangers and vaporizer were connected through welded fittings and pressure leak-checked prior to on-sun tests. The instrumentation included pressure and temperature sensors at inlets and outlets of all individual devices. In Figure 4-13, 3D models of the on-sun section of the reaction system from TRL 4 to TRL 6 are compared. The TRL 6 was the most compact unit but the overall connectivity was similar. The reduction in reactor mass enabled more efficient reactor mount: earlier reactors (TRL 4 and TRL 6) were suspended at corner tabs while TRL 6 was supported at center by connection tube. This change reduced conduction heat loss through the mounting rods (not shown).

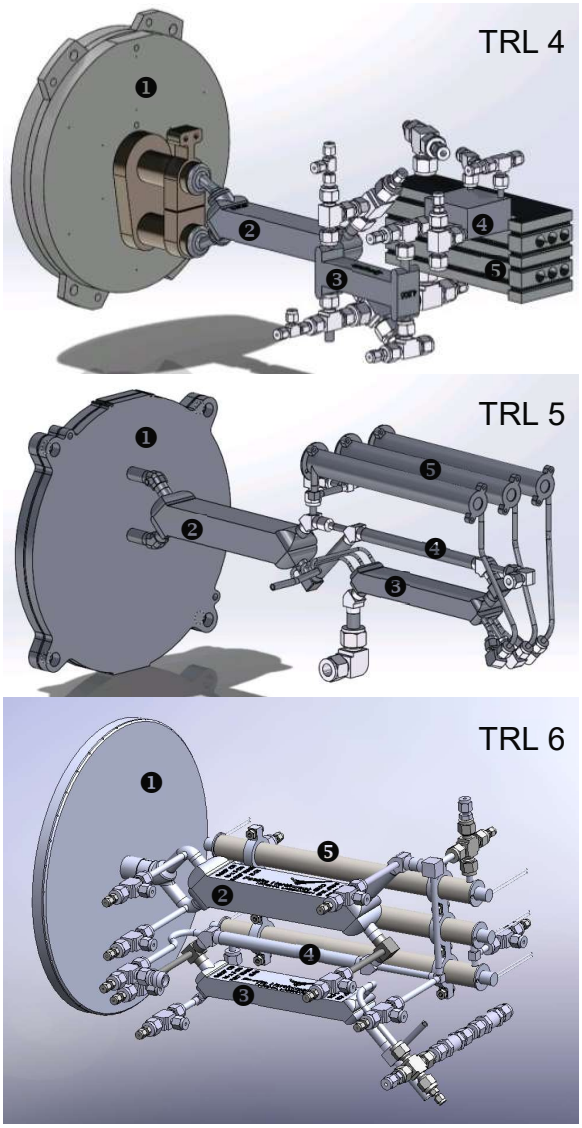

Figure 4-13 Reactor on-sun assembly (**1**, SMR reactor; **2**, high temperature recuperator; **3**, water preheater; **4**, methane preheater; **5**, vaporizer).

4.3 On-Sun Performance Testing

This task was responsible for establishing reactor test facilities, performing shakedown tests and on-sun operation of the prototype reaction systems, and collecting system performance data. The on-sun test results were used to validate reaction system designs and to identify potential improvements. Operation protocols for efficient handling startup, turn-down, and transients were also developed as a part of these activities.

4.3.1 Reactor Test Stand Development

4.3.1.1 On-Sun Test System Configuration

The configuration of the solar thermochemical reaction system tested under this project is given in Figure 4-14. The system consisted of a PD3 solar dish concentrator, an on-sun unit located at the focal point of the PD3 dish, and the balance of plant located on the ground. Feed gas system, water pump, process analytical equipment, and tail gas flare were parts of the latter group. The on-sun reactor unit included the SMR reactor, recuperative heat exchangers, water vaporizer, and onboard process controllers.

The feed gas was controlled using a mass flow controller. The methane stream was preheated by the network of recuperative heat exchangers using the product stream. Concentrated solar energy was absorbed by the reforming reactor to convert methane to syngas catalytically. The syngas product stream was cooled by the feed gas stream and additional air cooling. The compositions of the product gas were analyzed by a process gas chromatograph. The product stream was vented through a flare after condensed water was separated.

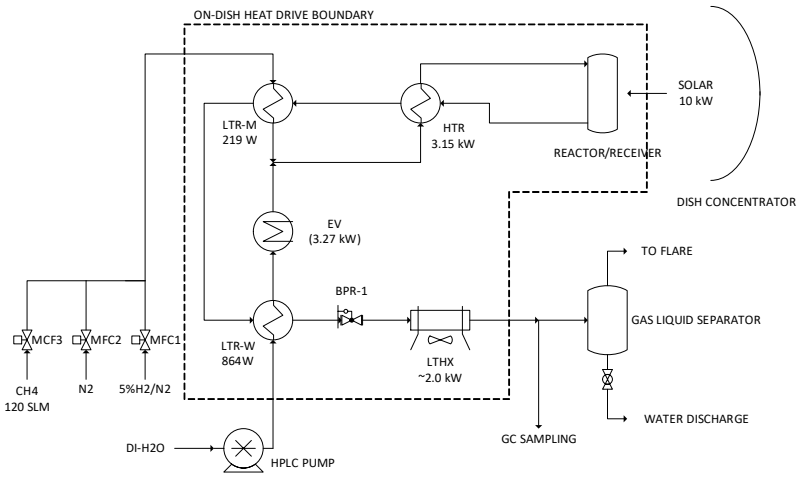

Figure 4-14 Process diagram of the solar thermochemical reaction system (HTR, high temperature recuperator; LTR-M, low temperature methane recuperator; LTR-W, low temperature water recuperator; LTHX, low temperature radiator; EV, electrical water vaporizer; MFCs, mass flow controllers; BPR, back pressure regulator).

4.3.1.2 Dish Solar Concentrator Test Sites

Two solar concentrator test sites were established during the course of this project, one in Washington State and one in California. Both were based on the Infinia PowerDish III (PD3) parabolic dish concentrators (total reflector area: 14.85 m^2). Basic characteristics of the PD3 system are summarized in Table 4-6. All on-sun performance testing under this project was done at these two test sites.

Table 4-6 Infinia PowerDish III concentrator characteristics.

Parameter	*Description*
Reflector Type	Parabolic
Tracker System	Precision Dual-Axis
Dish Diameter	15.4 feet (4.7m)
Height	21 feet (6.4 m)
Weight	1,900 lb (860 kg)
Total Reflector Area	14.85 m^2

Richland WA Test Site

During Phase 1, a new solar concentrator test site was established on the PNNL main campus located in Richland, WA. A photo of this test site is shown in Figure 4-15. The original PD3 receivers were modified for integration with PNNL's solar SMR reactors. This pairing was used for all on-sun testing. The performance of the Richland solar concentrator test stand was validated using an in-house design cold-water calorimeter as well as flux map evaluation by operation during full moon. The balance of plant, mainly ground equipment for gas supplies, tail gas flare, and control room facility were put in place. Process analytical instruments critical to reactor performance measurements, such as gas chromatograph and mass spectrometer, were also set up.

The Richland test stand was commissioned in the summer of 2013 and operated through the end of Phase 2 in 2015. The annual average solar resource at this location is about 5 $kWh/m^2/day$. Summer testing was enhanced by long days and generally good weather conditions. Winter months were hampered by cloud cover and freezing temperatures. Both TRL 4 and TRL 5 reaction systems were tested on this test stand.

Figure 4-15 PNNL solar thermochemical reactor test stand photos (**left**, Richland, WA; **right**, Brawley CA).

Brawley CA Test Site

During Phase 3 of this project, a second solar concentrator test site was established at the San Diego State University's Center for Energy Sustainability on its campus in Brawley, CA. An additional PD3 dish concentrator was set up using original equipment developed by Infinia. The system was a containerized twin-PD3 dish unit suitable for compact shipment in a standard container and rapid field deployment. The performance of the new dish concentrator was checked by cold-water calorimeter tests. Similar balance of plant to the Richland test site was set up in Brawley.

The new test site was commissioned in the summer of 2016 and operated through the end of Phase 3 on-sun testing. Great annual average solar resource was available at this location: 7-8 kWh/m^2/day. Reliable clear sky weather allowed year-round testing.

4.3.1.3 Dish Concentrator Flux Mapping

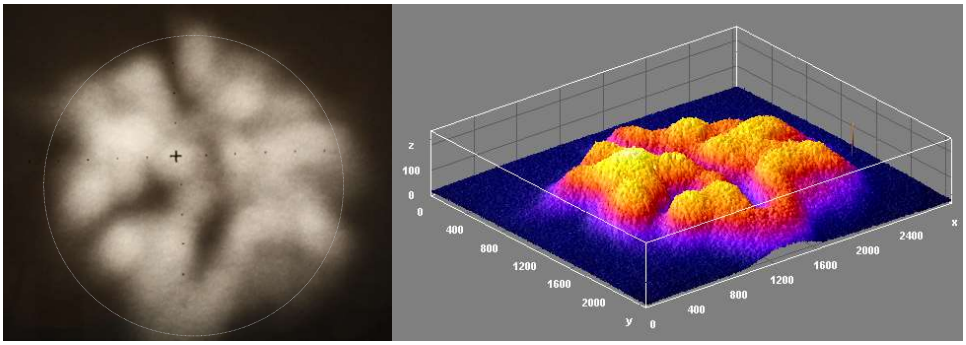

Figure 4-16 Moon flux photograph at the reactor plane (circle: reactor boundary) and corresponding flux map (x and y: pixel numbers; z: percentage of the maximum flux density observed).

The PD3 dish concentrator was evaluated by moon flux mapping during the start of Phase 1. The objective of the on-moon test was to characterize the flux distribution of the dish concentrator at the focal plane and the receiver-reactor plane. While on-sun testing can produce quantitative flux maps, on-moon testing is safer with an uncharacterized dish and relatively simple without the requirement of a cooled or refractory target. The dish concentrator was set up to track movements of a full moon. Photographs of

the focused lunar light projected onto a screen were taken. The flux distribution at the screen location was then approximated by the image light intensity variation. The resulting flux map (Figure 4-16) captured the inhomogeneity characteristic of the dish concentrator used in subsequent on-sun tests. This flux map was used in all reactor modeling as part of the boundary conditions.

4.3.1.4 Evaluation of Intercept Factor

The intercept factor of the dish concentrator system is the ratio of the irradiation intercepted by the receiver to the irradiation reflected by the reflector. It is an important parameter for the calculation of the energy conversion efficiency of the reaction system. A cold water flow calorimeter (Figure 4-17) was built in-house during Phase 1 and was used to calibrate the dish concentrator intercept in all on-sun tests. The calorimeter was constructed with coils of copper tubing forming a deep cavity inside an original PD3 receiver housing. The surface of the copper tube cavity was painted black to minimize reflection loss. The intercepts of the PD3 dish concentrators used in on-sun tests were determined to range from 0.83 to 0.87 with 1-2% uncertainty in individual measurements and with an assumed 0.93 reflectance of freshly washed dish reflectors. Three metal screens with different opening ratios were also calibrated to have transmission factors of 0.659, 0.443, and 0.800 with 1% uncertainty. These screens were used during on-sun tests as insolation limiting devices to allow testing at low solar flux conditions when actual direct normal irradiation was high.

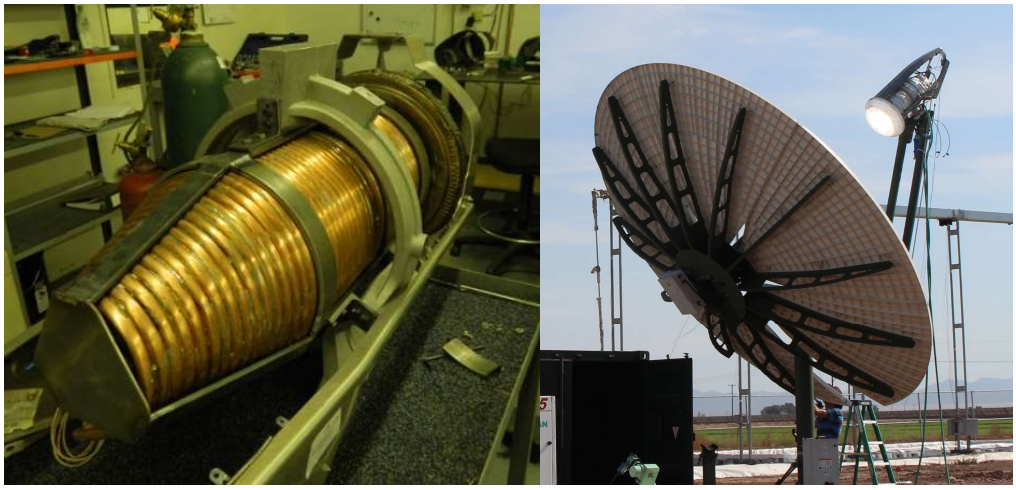

Figure 4-17 Cold water flow calorimeter (left) and intercept evaluation of the dish concentrator at the Brawley CA test site (right).

The PD3 dish concentrator installed at the Brawley CA test site was evaluated using the cold water flow calorimeter during Phase 3 as part of the concentrator commissioning. The mirror panels on this dish concentrator were re-used parts from a previous project and had been in service for a long time. As a result, relatively larger optical errors were observed on the Brawley dish than the Richland dish. The intercept factor of the Brawley dish concentrator was estimated to be 0.83, lower than the 0.87 to 0.89 measured intercept of the Richland dish, meaning that the concentrator at Brawley delivers about 5% less of the available direct-normal solar energy to the reactor/receiver compared to the dish used in Phases 1 and 2 of the project.

4.3.2 On-Sun Test Activities

4.3.2.1 Phase 1 On-Sun Tests

Initial on-moon flux map test and on-sun calorimeter test on the Richland test stand revealed that the dish reflector efficiency was lower than expected. The cause of the low efficiency and non-optimal flux distribution were determined to be aging and outgassing of the adhesive bonding under the mirror panels, causing movements from the original true parabolic contour. Subsequently, the mirror panels were replaced with a new set that were manufactured with an improved adhesive formula. Additional calorimetry measurements and moon flux map tests confirmed improved performance of the new mirrors. From July to September 2013 a parametric study of reactor energy efficiency and heat loss at various test conditions was conducted using the TR4 reaction system. The variables studied included the solar direct normal irradiance, reactor temperature, feed flow rate, and steam-to-carbon ratio.

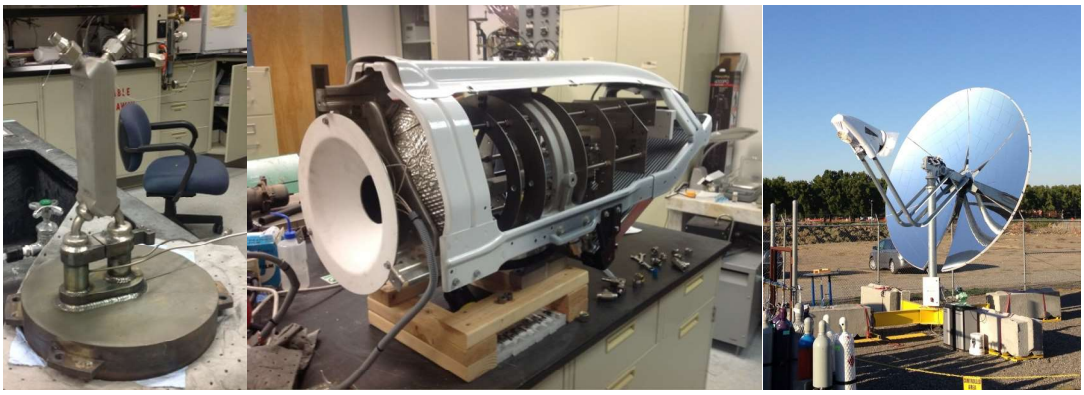

Figure 4-18 TRL 4 on-sun testing photos (**left**, reactor and heat exchanger weld assembly; center, on-sun reactor unit; **right**, TRL 4 reactor tested on dish concentrator in Richland, WA).

4.3.2.2 Phase 2 On-Sun Tests

A number of upgrades were performed at the Richland test site including a new control system. The reactor/dish concentrator control logic was enhanced to enable automatic cycling of the dish tracking modes. This allowed the reactor temperature ramp rate to be controlled easily to an acceptable level during start-up while allow fast transition from startup mode to normal operation mode or recovery from transient clouds.

In September 2014, shakedown testing of the solar concentrator test stand and reactor control system were performed using the TRL 4 reactor from Phase 1. In October 2014, the TRL 5 reactor and heat exchanger weld assembly was completed and assembled into the on-sun reactor unit (Figure 4-19). On-sun testing of the TRL 5 system was performed in the months of October and November to evaluate the effects of the design changes on the system efficiency metrics.

Figure 4-19 TRL 5 on-sun testing photos (**left**, reactor and heat exchanger weld assembly; **center**, on-sun reactor unit; right, TRL 5 reactor tested on dish concentrator in Richland, WA).

A new high-temperature infrared imaging camera was purchased from FLIR Systems, Inc., and configured for on-sun tests. Test protocols and data/image analysis algorithm were developed to capture reactor face IR images at different available angles and to build a composite temperature maps of the reactor sun-side skin. The FLIR IR camera was used in the above on-sun tests to examine the temperature profile of the reactor front face. The TRL 5 reactor had 5 additional intrinsic thermocouples on its front skin to measure sun-side surface temperature directly. The TRL 4 reactor had 2 such face surface thermocouples installed. Another significant difference from the TRL 4 reactor was that there was one thermocouple at the end of each reaction channel (36 in total) on the TRL 5 reactor. The end of channel temperature data were used to evaluate the effect of inhomogeneous flux distribution on individual reaction channels.

4.3.2.3 Phase 3 On-Sun Tests

During the fall months of 2015, additional on-sun tests were carried out at the Richland test site on the TRL 5 reaction system. This was the continuation of the TRL 5 on-sun tests performed in 2014, which were mainly at low solar conditions. On-sun performance data at relatively higher solar flux were collected in 2015 together with more reactor thermographs under operating conditions. A new reaction system, TRL 6, was designed and fabricated in 2016, incorporated an advanced internal heat spreading and recuperation channel structure. The TRL 6 reactor on-sun unit assembly was completed in August, 2016 (Figure 4-20). TRL 6 on-sun tests were performed in September and October under medium to high solar flux conditions. Extensive IR thermographs of the reactor solar surface were collected to aid the evaluation of thermal performance.

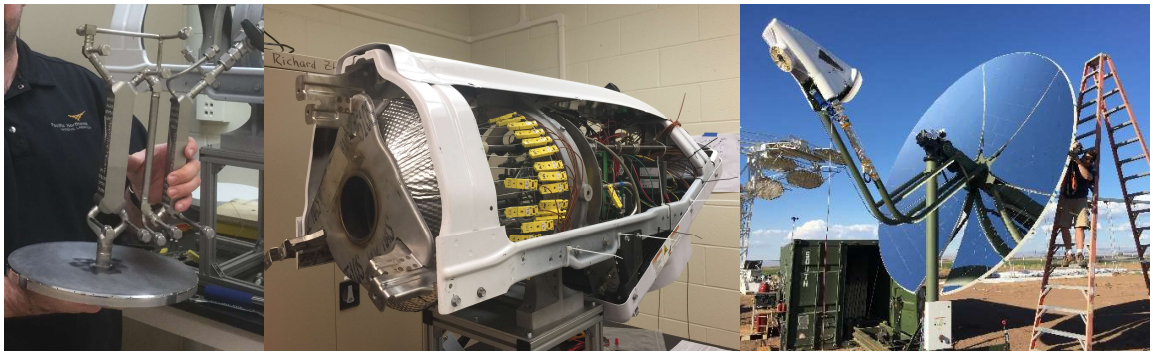

Figure 4-20 TRL 6 on-sun testing photos (left, reactor and heat exchanger weld assembly; center, on-sun reactor unit; right, TRL 6 reactor tested on dish concentrator in Brawley, CA).

4.3.3 On-Sun Test Technical Results

Three reaction system prototypes were tested on-sun during this project. These prototype systems were described earlier in the reaction system fabrication section. The on-sun testing activities were summarized in the previous section. In this section, the on-sun test results are provided and main findings are summarized.

4.3.3.1 Dynamic Operation Characteristics

The on-sun testing was focused primarily on the steady state performance of the reaction systems in terms of the methane steam reforming conversion, the solar to chemical energy conversion efficiency, and the reactor temperature distributions. However, during the course of testing, start-ups and shutdowns and response to cloud transients were naturally part of the experimental steps taken to get to a system steady state. Data collected and understandings obtained about the system operation characteristics during these dynamic processes are important to the eventual commercial solar thermochemical reaction system product, both because the plant productivity will depend on how fast it can be started up and responded to transients and because the operation cycles may play a large role in reactor life time due to cycle fatigue effects.

Start-Ups and Shutdowns

A start-up example is illustrated in Figure 4-21 by early data from 2014 with the TRL 5 system (CH_4 flow at 0.062 mol/s and steam to carbon ratio at 2). The green solid curve is the direct normal irradiance (DNI) measurements in W/m^2 from about 8 am to 4 pm, with a peak DNI around 850 W/m^2 at noon. The small variations in DNI around noon were from thin clouds at high altitude. The blue square wave profile reflects the changes in the reaction system on-sun status in arbitrary unit: an initial short standby (the lowest level), followed by shadow tracking (the dish following a small angle above with the sun so no flux was directed to the reactor), then cycling to sun tracking between shadow tracking to control the amount of reactor heat input during ramp-up, and finally steady state sun tracking at full reactor duty. Other curves are plots of various reactor temperature readings. The red curve with large fluctuations is the reading from a thermocouple fixed to the sun-facing surface of the reactor, the hottest spot on the reactor. The double-weight red solid curve is the average temperature in the reactor channels.

Heating the reactor to an operating temperature greater than 600°C was accomplished at a controlled average ramp rate by cycling the dish concentrator on-sun and off-sun. For this on-sun run, a dwell time of one hour at 200-250°C was used to flow a dilute H_2/N_2 gas through the reactor to ensure the catalyst was reduced after a long period not in operation (days). For a routine daily start-up to 600°C without the catalyst reduction step, the temperature ramp up period (mark #1 to #2) took about two hours for this reaction system.

The methane and steam reactant flow was ramped up in the next one and half hours (mark #2 to #3). The increasing reactor heat duty was matched by shifting the dish concentrator mode from cycling between on-sun/off-sun to a constant on-sun circle tracking mode, where the focus of the concentrated

sun light was moved around the reactor center in circles at a small constant angle offset to spill some incident flux. The reduced insolation allowed the operation at partial duty. This was necessary if the full flux condition required too high a reactor duty that would have caused reactor surface temperatures to exceed rating.

The reactor was operated at the reduced insolation for about one hour (marks #3 to #4) until the DNI dropped to 800W/m^2 level at about 2 pm. At this point, the dish concentrator was set to sun-tracking without spillage (after mark #4). The full flux from the dish concentrator was directed to the reactor for endothermic methane steam reforming. Typically, the reactor was operated for a period of time at steady state to obtain performance data (mark #4 to #5). Usually, more data points were collected by repeating the full flux steady state operation at other conditions.

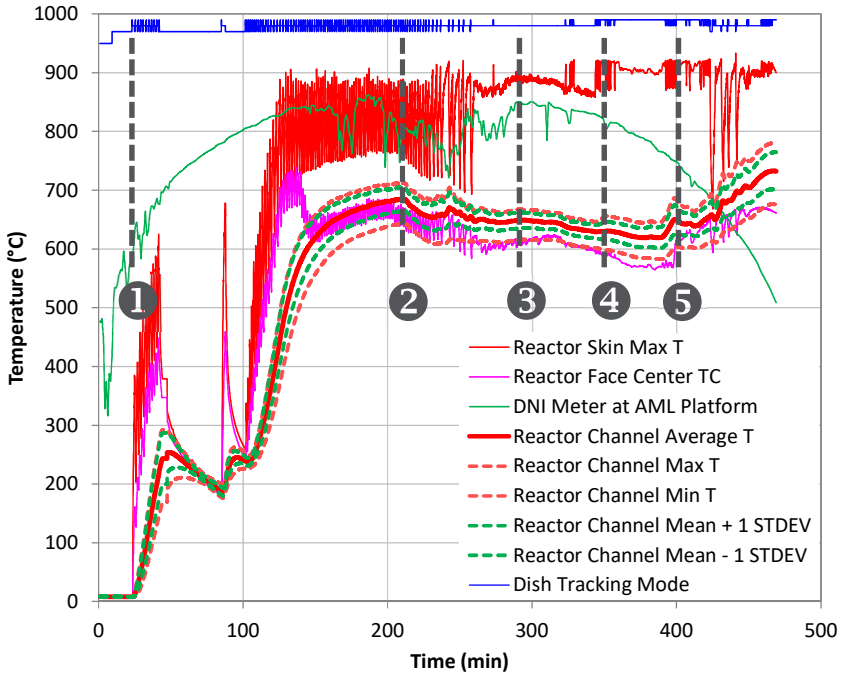

Figure 4-21 Typical on-sun reactor startup temperature profiles (TRL 5, 2014-11-10, methane flow 0.062 mol/s, S/C=2)**.**

Several findings were apparent from the reactor start-up operations. First, while a fast ramp-up is highly desirable in order to maximize the usage of daily available solar resources, a conservative ramp rate limit was set during testing, e.g. less than 20°C/min by the average reactor channel temperature. A detailed thermomechanical stress and cycle fatigue analysis may lead to a relaxation of this constraint and a more rapid ramp-up. Such analysis was beyond the scope of this project. However, in later phases, a small auxiliary electrical heater was added to the back of the solar reforming reactor. The back heater provided up to 1 kW capacity to preheat the reactor prior to sunrise, thus adding potentially 1 to 2 hours of on-sun production. The back heater also helped warming the reactor more evenly during preheating with solar flux because heat input was applied to both front and back of the reactor, leading to less thermal stress and a more favorable cycle life time. The auxiliary startup heater is therefore recommended for addition to the next commercialization reactor development.

The second finding from the start-up experiences was that the reactors manufactured from alloys that could handle higher temperatures (e.g., Haynes 230 compared to Hastelloy X, combined with a thinner

cover plate and better internal heat spreading capability, such as was designed into the TRL 6 reactor, offered much better start-up performance: the start-up times needed to ramp up both the reactor temperature and the reactant flow were reduced significantly. The thinner plates, critically, reduced the reactor surface temperature adequately during full flux such that the reactor was easily able to operate at full duty for all day time hours. The start-up performance of the TRL 6 reactor at high solar DNI is illustrated in Figure 4-22. The back heater was operated during start-up after sunrise. The temperature ramp was reduced to less than one hour, a value that can be further reduced through procedural and control system improvements. The reactor was brought to full flux operation in less than 45 min afterwards. This was a significant improvement from the start-up performance of earlier reactors. If preheating is done prior to sunrise, at most 45 min of early morning solar energy at relatively low DNI would be lost during start-up – a loss that could be offset by activating the supplemental heating during non-peak solar hours.

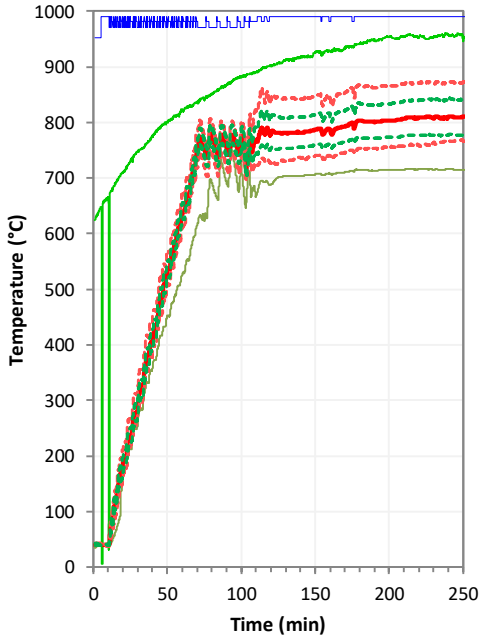

Figure 4-22 TRL 6 reactor start-up temperature profiles (2016-10-21, methane flow 0.046 to 0.059 mol/s, S/C=2.2, peak duty 14kW solar; legends and color coding are the same as in **Figure 4-21**).

Response to Cloud Transients

The solar reaction systems were able to operate with some high clouds. The cloud cover reduced the direct normal solar irradiation available at the dish concentrator. By reducing the reactant flow during cloud transients, the reactor duty could be reduced to match the heat input. During Phase 1, a feedback control loop was developed for reactor temperature control. The control system was successfully used during Phase 2 and Phase 3 testing to maintain constant reaction zone temperature. The ability of the control system depended on the reactor's thermal mass. The heavier early reactor prototype with thicker plates had more thermal mass, thus was easier to operate in terms holding constant reaction zone temperature during brief cloud transients. By tuning the control loop parameters, similar performance was achieved with later reactor prototypes with lighter mass and thinner plates. The cutoff point of the

control loop depended on overall system heat loss, which will be discussed in the next section. Typically, when DNI dropped below a few hundred watts/m^2, standby of the reactor was usually needed.

4.3.3.2 Reaction System Energy Balance

The energy efficiency of the reaction system is determined by the energy losses. Conduction, convective, and radiative heat losses all contributed to the overall system heat loss. The relative order of magnitudes of these loss terms had been evaluated by a receiver-reactor model (see Section 4.1.2). As part of the on-sun testing, the heat losses were evaluated experimentally based on system energy balance. The results and their implications to the reaction system designs are given this section.

System Fixed Heat Losses

Among the reaction system heat losses, the radiative heat loss largely depends on the receiver design and the reactor surface temperature. In this project, the commercial Infinia PD3 receiver was used with little modification because the dish concentrator was not the focus of the system development. On the other hand, the reactor surface temperature is a function of the reactor design and operating conditions. The convective heat loss depends mostly on wind speed, reactor orientation (related to sun position), and reactor temperature. The conduction heat loss depends both the receiver and the reactor designs. Again this project was focused the reactor design, such as thermal performance of the reactor mounting structuring.

The reactor heat duty, $Q_{reactor}$, when plotted against the thermal input delivered by the concentrator, $Q_{receiver}$, over a range of thermal inputs can be used to estimate the overall thermal losses across the receiver-reactor boundary. Because the receiver thermal losses are largely independent of input power, the x-axis intercept is a good estimate of the receiver's thermal losses. The reactor and receiver heat duties are calculated as follows,

$$Q_{reactor} = h_{reactor,out} - h_{reactor,in} \tag{16}$$

$$Q_{receiver} = \rho\varphi Q_{solar} \tag{17}$$

$$Q_{solar} = A_{dish} B_n \tag{18}$$

where $h_{reactor}$ is the enthalpy of the streams flowing into and out of the reactor, including the chemical enthalpy content, ρ is the concentrator mirror reflectance, φ is the concentrator intercept factor (measurements from cold water flow calorimetry, see Section 4.3.1.4), Q_{solar} is the total solar energy input to the dish concentrator, A_{dish} is the dish concentrator area, and B_n is the direct normal irradiance of the sun.

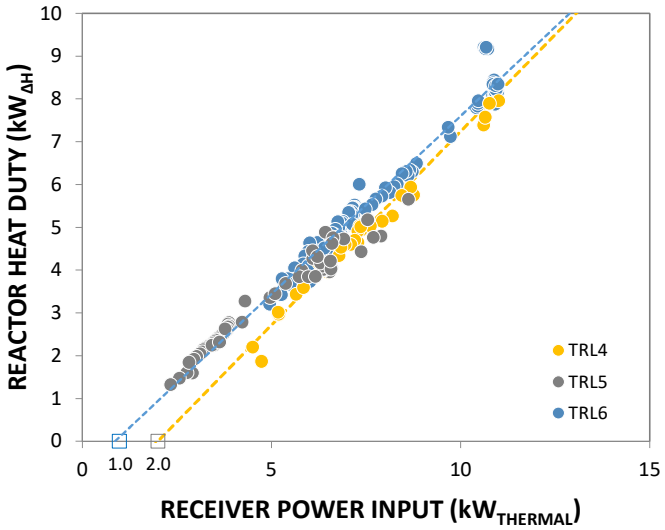

Figure 4-23 Reactor heat duty vs. receiver heat input plots for the solar thermochemical reaction systems.

In Figure 4-23, the reactor heat duty is plotted against the receiver heat input for all reaction systems developed under this project. Across a large range of input power, the relationship between the reactor duty and receiver heat input can be described well by a linear fit, where the x-axis intercept reflects the system fixed thermal loss, i.e. the minimum amount of solar power the reactor/receiver must receive before there can be a net output after heat loss.

From Figure 4-23, the early system, TRL 4, had a fixed heat loss about 2 kW. This value was comparable to the 2.5 kW total heat loss estimate from the CIRCE2/AEETES model results for this reactor configuration. Among the major thermal losses, conduction was estimated to be at least 0.9 kW. Additional loss through convection was estimated to be in several hundred watt range. The design changes in the later prototypes, TRL 5 and TRL 6, were made to address these losses. Specifically, this convection loss was reduced by eliminating a cooling fan on the on-sun unit. A smoke tube air flow test had confirmed that there was a small air connection from the hot receiver cavity to behind the TRL 4 reactor, which provided a heat leak when the fan was operated. The conduction heat loss through reactor mounting hardware was reduced on the TRL 5 reactor by the use of smaller mounting brackets. The TRL 6 reactor eliminated the mounting brackets and used small ceramic standoffs to isolate the reactor from restraining devices. These measures resulted in a reduction in the overall heat loss. As seen in Figure 4-23, the TRL 5 and TRL 6 systems had similar heat losses at about 1 kW, which was a 50% improvement from the TRL 4 fixed heat loss.

Obviously, the fixed heat loss will have a large significance in the system efficiency, the topic of the next section. Less obviously, it is also important to system control strategy: when a cloud cover causes the DNI to drop below an equivalent heat input equal to this value, stable reactor operation becomes impossible regardless of the flow rate. This threshold DNI was estimated to be between 100 to 200 W/m^2, for these reaction systems.

Thermal Efficiency

The thermal efficiency of the reactor-receiver, $\eta_{reactor\text{-}receiver}$, which is defined as the ratio of the net increase in reactor stream enthalpy, i.e. the reactor duty, to the receiver heat duty,

$$\eta_{reactor-reci} = Q_{reactor}/Q_{receiver}. \quad (19)$$

As defined above, the thermal efficiency accounts for thermal losses across the reactor-receiver boundary but does not include the optical losses due to imperfect concentrator mirrors or the receiver's intercept.

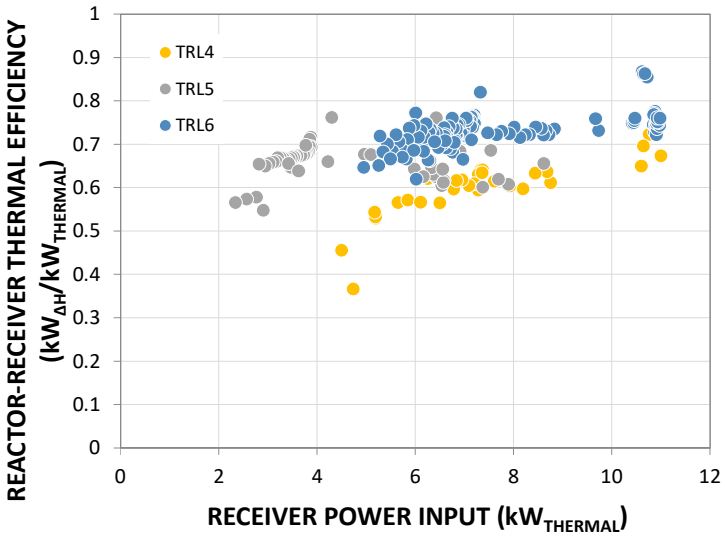

Figure 4-24 Receiver-Reactor thermal efficiency of TRL 4 to TRL 6 reaction systems over broad operating conditions.

In Figure 4-24, the measured reactor-receiver thermal efficiency over broad operating conditions were plotted as a function of the receiver input power for all reaction systems evaluated. The TRL 5 system was not operated at high flux conditions because of the reactor alloy material temperature limit. In the TRL 6 system, the reactor temperature rating was increased by using the same Haynes 230 alloy as on the TRL 4 system. The thermal efficiency, a measure of the reactor-receiver's efficiency according to the first law of thermodynamics, was generally in the range from 55% to 75%. Especially of interest is average 75% thermal efficiency of the TRL 6 system operating at high flux, as this is the most relevant configuration for next phase commercialization development. Peak thermal efficiency just over 85% had been experimentally observed on the TRL 6 system at close to 11 kW heat input.

4.3.3.3 Reactor Temperature Distribution

The temperature distribution in the reactor plays a critical role in the efficiency of the reactor system. It also impacts the reactor life time. On the reactor sun-facing surface, the temperature distribution is predominantly determined by the incident concentrated solar flux distribution. The solar flux incident upon the reactor produced local hot spots where local flux level could be several times higher than the surrounding mean level. Infrared thermography of the reactor face as well as direct temperature

measurements using thermocouples (TCs) were performed during reactor on-sun tests in order to understand the extent of inhomogeneous distributions at the reactor surface and inside the reaction channels, the ability of the reactor to spread out local flux concentrations, and the effects of temperature distribution on reactor system efficiencies. The results are summarized in this section.

The TRL 4 reactor had 10 TCs installed at various locations and depths from surface. Two additional instrinic were also spotwelded to the surface. On the TRL 5 and TRL 6 reactors, a TC was installed at the end of each of the 36 reaction channels. The TRL 5 reactor also had 5 additional intrinisc TCs for surface temperature measurments. The reactor skin temperature distribution was also evaluated using a high-temperature FLIR infrared camera. Because only portion of the reactor surface was visible through the aperture, IR images were collected at multiple angles to the dish axis. The image set were later processed by a software algorithm to reconstruct a composite image covering a larger portion reactor surface. The IR camera had been calibrated to NIST-traceable temperature references. The black Pyromark painted reactor surface was assumed to have an emissivity of 0.95.

TRL 5 Reactor

Initial IR thermography confirmed the existence of local hot spots. For example, two hot spots in the 900°C range were observed generally in area on the surface between 1/3 and 2/3 of the reactor radius on the thermograph in Figure 4-25. Only the top half of the reactor surface was imaged because this was the half visible by the camera from ground. The hot spot locations agreed with what were indicated by the flux maps based on ray-tracing performed on similar PD3 dish systems. These TRL 5 trials proved the feasbility using the IR camera to track the reactor on-sun temperature.

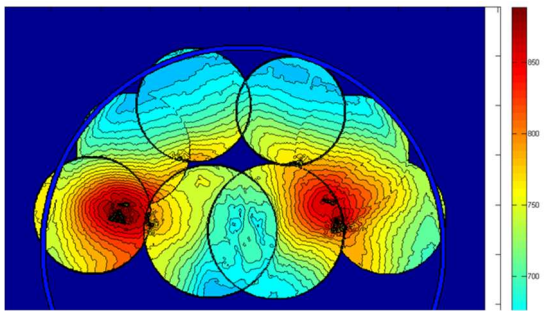

Figure 4-25 IR thermograph of TRL 5 reactor operating on-sun on 2014-11-17 with methane flow 0.011-0.015 mol/s and S/C 3.0 (color bar unit: °C; small circles: individual infrared images; large circle: boundary of the reactor surface inside the receiver cone).

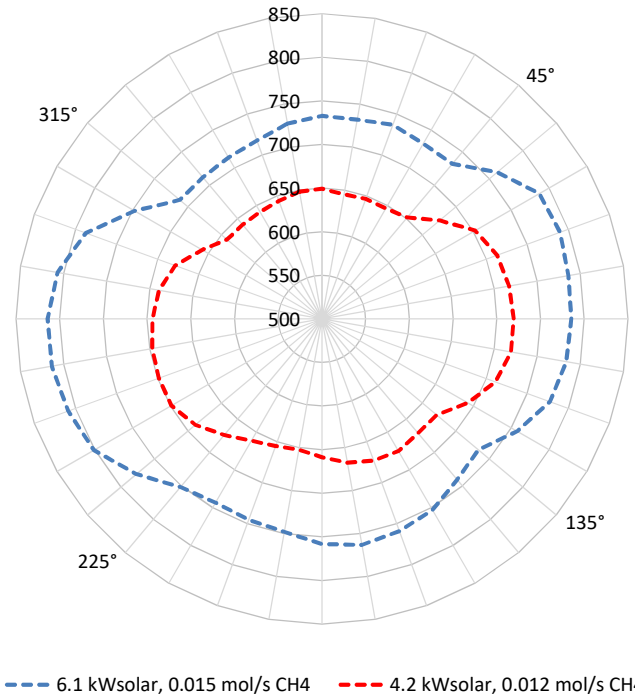

Figure 4-26 TRL 5 reactor channel temperature distribution during on-sun test 2014-11-17 (unit: °C).

The variation of reactor channel temperature distribution over time at different average reactor temperatures is shown in Figure 4-26 in radar plot format. In this plot, the reactor channel TCs were indexed from 1 to 36. The channel temperature variations were 80°C to 100°C when reactor channel average temperature was from 670°C to 760°C. The variation was consistent with the reactor surface temperature distribution from the IR thermography. The channels passing under the identified hot spots were hotter than the adjacent channels. The change in channel temperature at these hot channels was gradual, indicating thermal spreading. It was also observed that the reactor channels near the four reactor mounting brackets at 45, 135, 225, and 315 degrees from reactor top were generally colder than their adjacent channels. The temperature depression at these locations was attributed to conduction heat leaks along the reactor mounting structures. This finding led to the modification the TRL 5 reactor mount to reduce the heat leak. Additional on-sun data showed improvements in reducing the TRL 5 reactor channel temperature variations (Figure 4-28) under similar surface temperature inhomogeneity (Figure 4-27). The channel temperature variations were less than 50°C when reactor channel average temperature was from 650°C to 690°C. The improved reactor mount with thermal standoffs was therefore used on the next generation TRL 6 reactor.

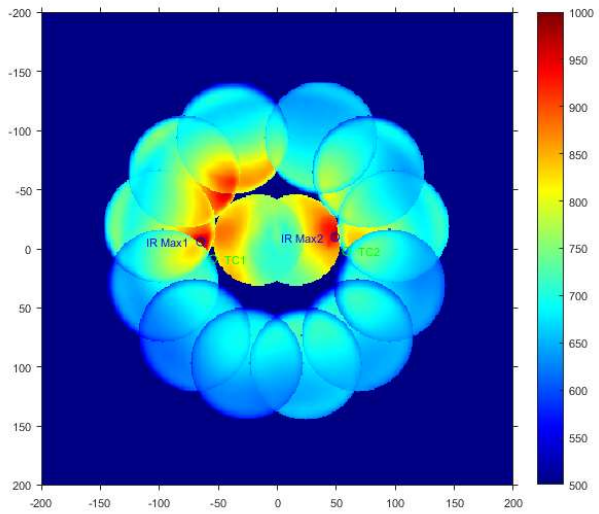

Figure 4-27 IR thermograph of TRL 5 reactor operating on-sun on 2015-11-10 with methane flow 0.014-0.038 mol/s and S/C 2.5 (color bar unit: °C; x and y coordinates: mm from reactor center).

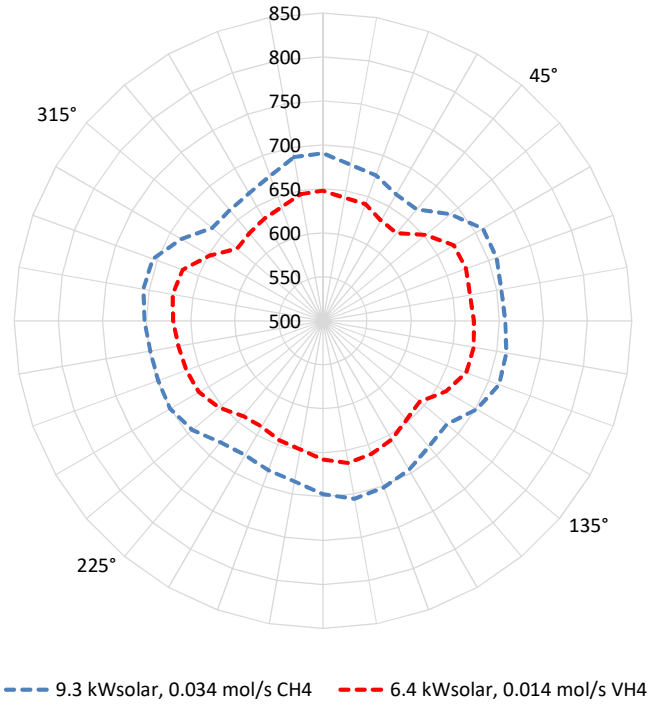

Figure 4-28 TRL 5 reactor channel temperature distribution during on-sun test 2015-11-10 (unit: °C).

TRL 6 Reactor

Similar evaluation of reactor temperature distribution by on-sun IR thermography was also conducted on the TRL 6 reactor. An IR thermograph of the reactor surface obtained under high flux conditions is shown in Figure 4-29. Snapshots of the reaction channel distribution at two time points are shown in

Figure 4-30. The TRL 6 on-sun tests were performed with a different dish concentrator from the previous reactors, thus the flux map and the location of surface hot spots were both different. It was observed that a ring shaped hot zone existed on the surface close to the edge of the reactor. This was attributed to a ceramic foam insulation ring around the TRL 6 reactor edge. The insulation was relatively thin (0.25") but had higher reflectance than the rest of the cavity. The hot zone was due to reflected radiative heat that would have had been absorbed and re-emitted over larger area.

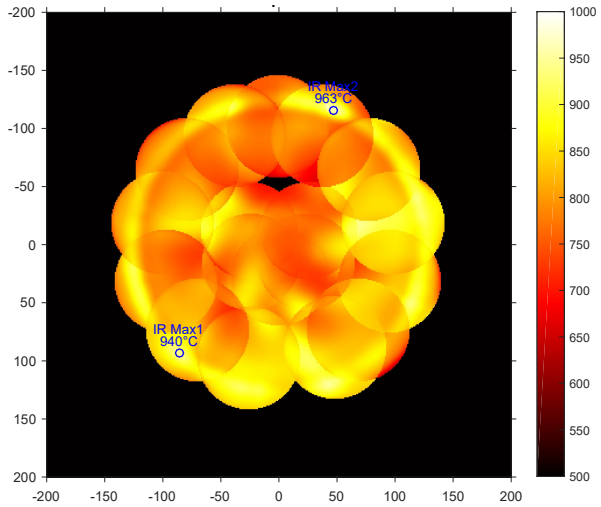

Figure 4-29 IR thermograph of TRL 6 reactor operating on-sun on 2016-10-18 with methane flow 0.052-0.055 mol/s and S/C 2.3-2.5 (color bar unit: °C; x and y coordinates: mm from reactor center; IR max: maxima on left and right halves).

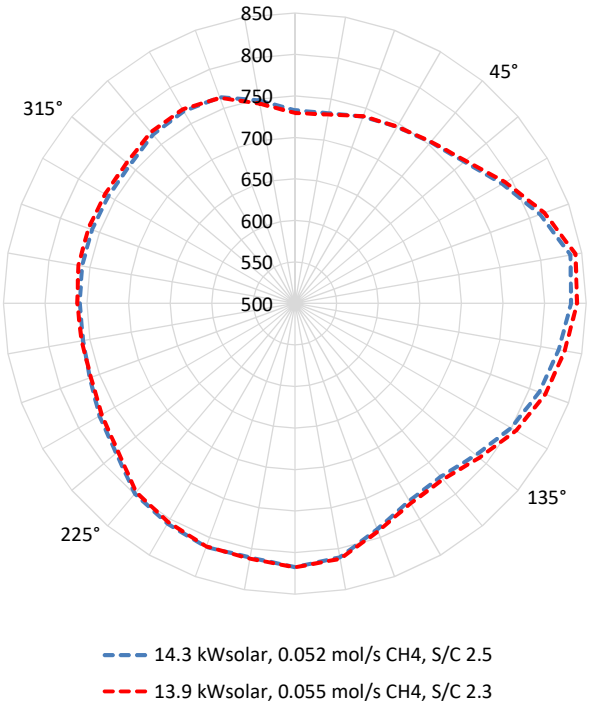

Figure 4-30 TRL 6 reactor channel temperature distribution during on-sun test 2016-10-18 (unit: °C).

A parametric study was performed with the TRL 6 reactor to evaluate the effect of reactor average temperature over a range from 785°C to 820°C. The reactor chemical conversion performance will be given in the next section. Here, the effect on the surface and channel temperature distributions are given. A series of IR thermographs of the reactor face are shown in Figure 4-31. It was observed that the overall pattern of hot spots was relative constant over wide range of reactor body temperature but the locations and magnitude of the hottest spots changed. The change in reaction channel temperature distribution is plotted in Figure 4-32. Similarly, the overall distribution pattern was relatively constant but some subtle shifts in local maixma were observed. Note that the camera angles for the IR thermographs in Figure 4-31 and for the channel distribution plot in Figure 4-31 were 180° apart due to experimental setup, i.e. view in front of the reactor vs. behind, thus the hot region on the right hand side of Figure 4-32 can be correlated to the hot spot on the left hand side in Figure 4-31.

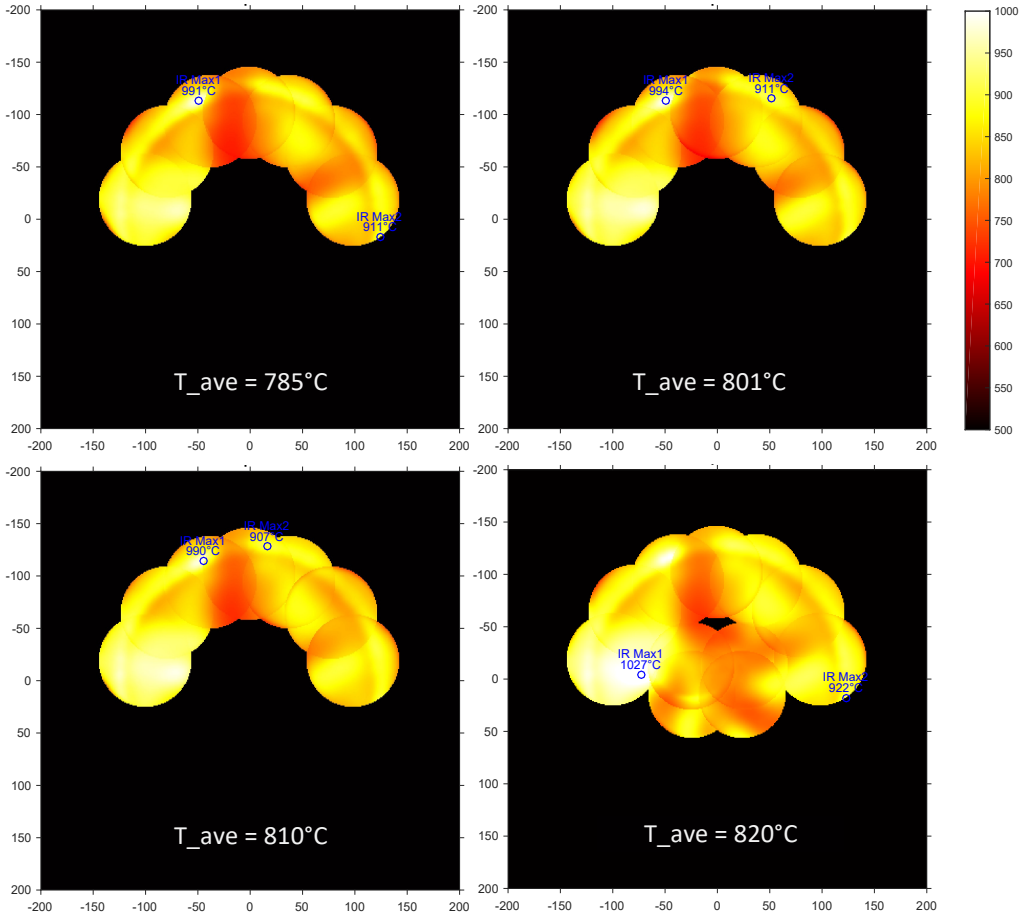

Figure 4-31 IR thermographs of TRL 6 reactor operating on-sun on 2016-10-21 with 13.6-14.3 kWsolar, methane flow 0.046-0.059 mol/s, and S/C 2.2 (color bar unit: °C; x and y coordinates: mm from reactor center).

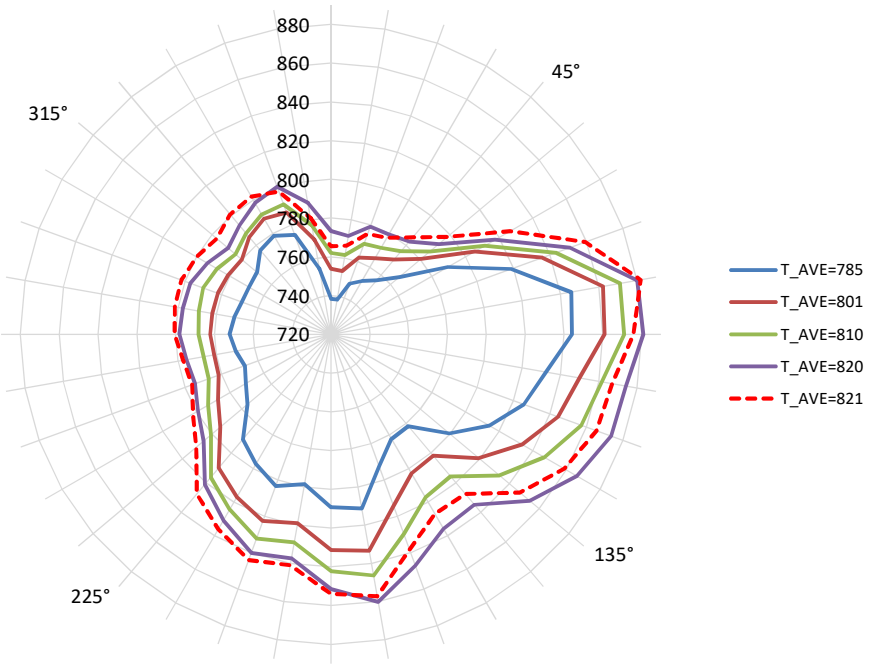

Figure 4-32 TRL 6 reactor channel temperature distribution at different reaction zone temperatures during on-sun test 2016-10-21 (unit: °C; 13.6-14.3 kWsolar, 0.046-0.059 mol/s CH_4, S/C 2.2; dash line: small adjustments of dish tracking parameters).

4.3.3.4 Chemical Conversion Performance

Solar Thermochemical Energy Conversion Efficiency

As a goal of the project was to augment the natural gas energy content with solar energy, it is important to evaluate the reaction system's solar energy conversion efficiency on a product gas higher heating value (HHV) basis. The solar to chemical energy conversion efficiency based on higher heating value, $\eta_{solar\ to\ HHV}$, is defined as:

$$\eta_{solar\ to\ HHV} = \left(\Delta H_{HHV,out} - \Delta H_{HHV,in}\right)/Q_{solar} \quad (20)$$

where $\Delta H_{HHV,out}$ and $\Delta H_{HHV,in}$ are the reactor outlet and inlet stream higher heating values, respectively, and Q_{solar} is the direct normal solar energy incident upon the dish, all in kW units. The above solar-to-chemical efficiency accounts for all system losses including optical errors of the dish concentrator and thermal losses at the reactor-receiver. Similar chemical energy efficiency can be defined for the reactor-receiver unit, excluding the dish concentrator:

$$\eta_{thermal\ to\ HHV} = \left(\Delta H_{HHV,out} - \Delta H_{HHV,in}\right)/Q_{receiver} \quad (21)$$

It is obvious that the reaction system's solar to chemical energy efficiency is related to the reactor-receiver's chemical energy efficiency and the dish concentrator's optical performance:

$$\eta_{solar\ to\ HHV} = \rho\ \varphi\ \eta_{thermal\ to\ HHV} \quad (22)$$

where ρ is the reflectivity of the dish surface, typically 0.93-0.94, and φ is the solar intercept, which is the percentage of reflected energy that enters the receiver cavity through the nacelle opening.

The solar to chemical energy conversion efficiency $\eta_{solar\ to\ HHV}$ for the TRL 4 to TRL 6 reaction systems (dish concentrator plus the reactor-receiver unit) over broad operating conditions are plotted on the left side of Figure 4-33 as a function of input solar flux. System solar to chemical energy efficiency as high as upper 60% was achieved with these reaction systems. The TRL 6 system was able to consistently achieve the high efficiency over medium to very high flux conditions. The thinner cover plate and the excellent heat spreading capacity of the TRL 6 reactor design allowed the reaction channel to be at higher temperature when the reactors were operated with the same surface temperature limit. The higher thermodynamic efficiency of the endothermic reaction at higher temperature is thought to be able to make up any additional radiative heat lost, thus the overall high solar to chemical conversion efficiency of TRL 6 reactor was able to extend to the high flux region.

For the thermochemical reactor-receivers, significant improvements in their chemical energy efficiency were made from TRL 4 to TRL 6, as revealed by the chart on the right side of Figure 4-33. The early TRL 4 reactor achieved close to 80% thermal to chemical energy (HHV-based) conversion efficiency. The TRL 5 improved upon the TRL 4 performance but was limited to low to medium flux operation due to the reactor alloy material. With the most advanced TRL 6 reactor, thermal to chemical energy conversion efficiency as high as 85% was achieved in the high flux region. Some data points suggest even close to 90% level performance may be possible.

Further energy efficiency improvement can be potentially be made by pairing the TRL 6 reactor with a dish concentrator with better intercept: the current concentrator intercept was approximately 83-87%. An intercept φ in the mid- to upper 90% range is possible with different dish concentrators. Therefore, a dish with an intercept of 0.95, combined with our TRL 6 system, could be expected to obtain a solar to chemical energy conversion efficiency of 75% and, we believe, values as high as 80% are achievable with additional improvements.

Ultimately, the economic tradeoff between the cost and performance of the reaction system and the dish concentrator system should determine the optimal design, which is beyond the scope of this project. For the reaction system alone, the solar to chemical energy conversion efficiency accomplished by this work was considered adequate for the next phase of technology commercialization.

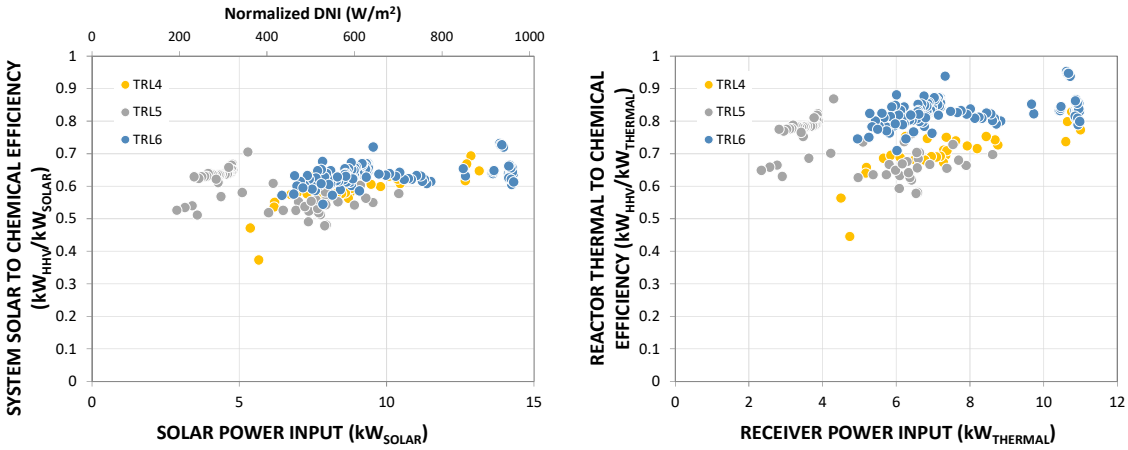

Figure 4-33 Reaction system and reactor chemical energy conversion efficiencies of TRL 4 to TRL 6 reaction systems over broad operating conditions (normalized DNI based on a hypothetical concentrator, $\rho = \varphi = 1$, $A_{dish} = 14.85$ m^2).

TRL 6 Parametric Study – Effect of Steam to Carbon Ratio

The effects of steam to carbon (S/C) were evaluated as part of the parametric study conducted using TRL 6 reaction system on-sun. At a higher S/C, more complete methane conversion at equilibrium is favored by the thermodynamics of the steam methane reforming reaction but higher S/C also requires a larger reactor for the additional mass flow and generally lower system efficiency due to the exergy destruction associated with the additional steam generation. The performance of the TRL 6 reactor was measured at a relatively high solar flux, 8.5 to 9.4 kW_{solar}, while controlling the average reaction channels within 790±1°C. The results are plotted in Figure 4-34.

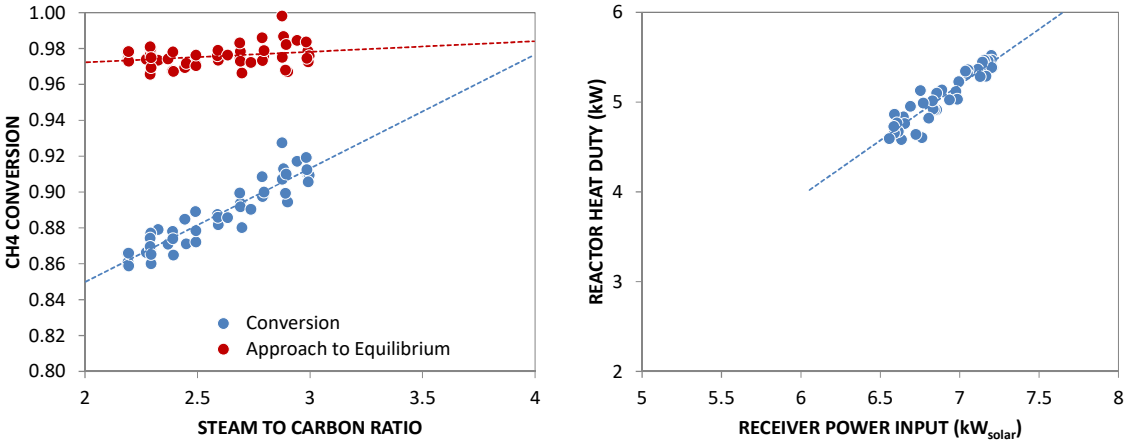

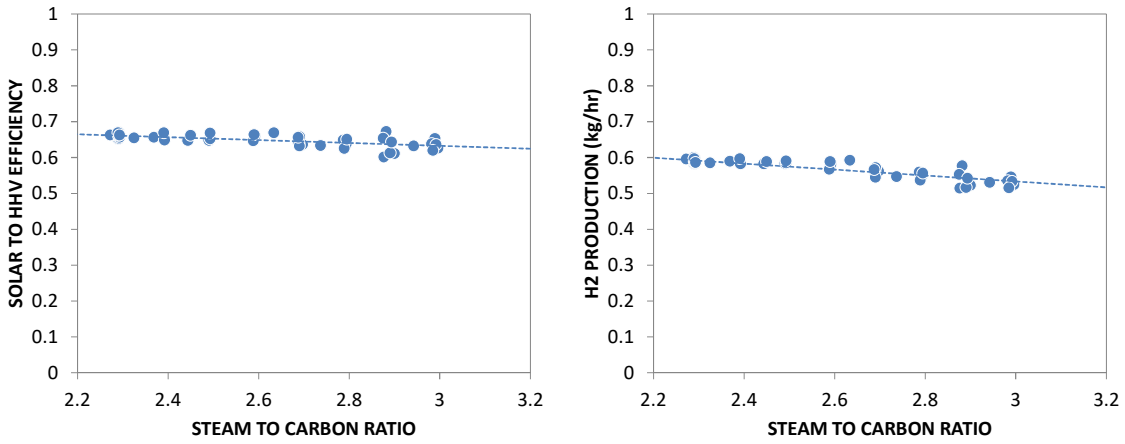

Figure 4-34 Effects of steam to carbon ratio on TRL 6 reaction system performance (2017-10-20 on-sun test, methane and water flow variations around 0.03 and 0.07 mol/s, respectively).

As expected, higher S/C produced higher methane conversion. The approach to equilibrium conversion was mostly constant at about 97% over the S/C range tested, 2.2 to 3.0. Overall, the TRL 6 reaction system was able to achieve over 90% conversion. The solar-to-chemical energy conversion efficiency and H_2 product flow were relatively insensitive to S/C increase but both slightly decreased with S/C from 2.2 to 3.0. Solar to chemical conversion efficiency of 63% to 67% were obtained. The weak dependency on S/C under test conditions was likely due to reduction in residence time at high steam flow. If this holds true for all operation conditions, optimal S/C can be selected based on catalyst stability requirement alone.

TRL 6 Parametric Study – Effect of Reaction Zone Temperature

The effects of reaction zone temperature, as measured as the average at the exits of all reaction channels, were evaluated as part of the parametric study of the TRL 6 reaction system performance. The reactor temperature was varied from 759°C to 789°C at S/C of 2.5 and from 783°C to 819°C at S/C of 2.2. The results are shown in Figure 4-35.

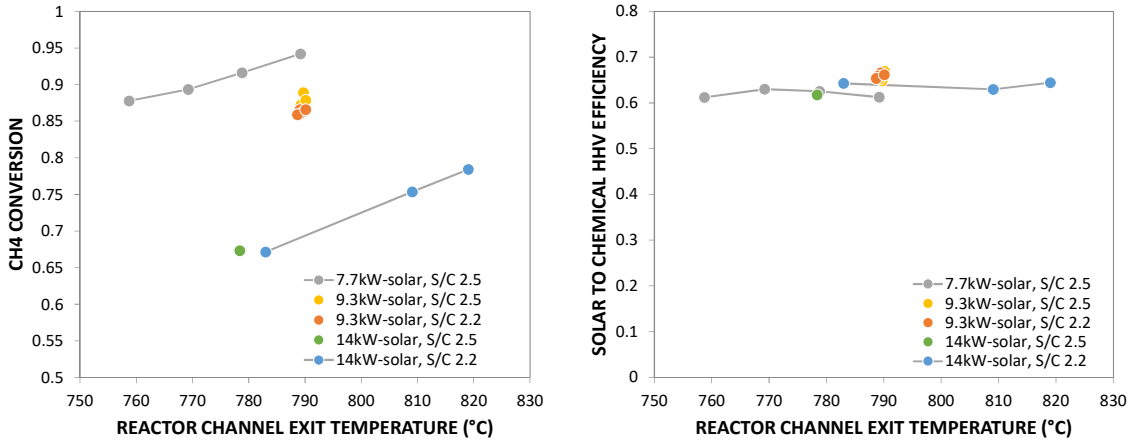

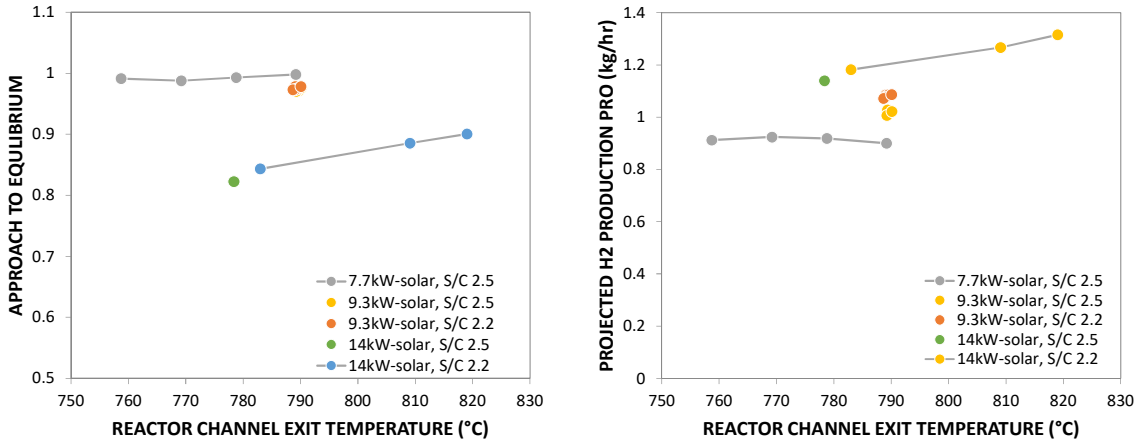

Figure 4-35 Effects of reaction zone temperature on TRL 6 reaction system performance (on-sun data sets from 2017-10-18 to 2017-10-21; projected hydrogen production assumes additional H_2 from complete CO conversion by WGS reaction).

The methane conversion increased with reactor temperature, as expected based on the higher reaction equilibrium conversion at higher temperature. The approach to equilibrium was nearly 100% at a steam to carbon ratio of 2.5 at these relatively high temperature tested. The equilibrium approach at a lower steam to carbon ratio of 2.2 was about 90% and improved with higher temperature. The solar-to-chemical energy conversion efficiency was relatively insensitive to temperature, indicating thermodynamic efficiency gain was on par with additional on-sun heat loss at higher temperature. This is a desirable attribute to achieve in terms of reactor design for high flux operation.

Generally, at a given flux and a fixed reactor design, operating at higher temperature requires decreased reactant flow, which tends to decrease product flow. On the other hand, higher methane conversion can be achieved, as shown in Figure 4-35, which tends to increase the H_2 and CO content in the product. The overall effect of higher reactor temperature on the hydrogen production flow was calculated assuming CO conversion to additional H_2 would be accomplished by a separate WGS reactor. The results, as plotted in the last panel in Figure 4-35, show that at medium flux an increase in reaction zone temperature had minimum effects on the projected hydrogen production because the CH_4 conversion already approached equilibrium. At the highest flux level, increasing the reaction zone temperature led to higher hydrogen production. This is attributed mainly to the shift of reaction equilibrium to higher CH_4 conversion at higher temperatures.

4.3.3.5 Reaction System Exergy Destructions

Throughout the project, exergy calculations provided design guidance and aided in developing a highly efficient reaction system.

In Phase 3 of the project, an exergy analysis was conducted based on TRL 6 on-sun performance data. The objective was to evaluate the reactor and the heat exchanger's second law efficiencies and to identify the sources and magnitudes of exergy destruction. In the exergy analysis, the exergy destruction at the reactor front surface was estimated by approximating the surface temperature with an average value based on IR thermography measurements. The reference environment was chosen as 25°C and 1 atm with chemical compositions as proposed by Szargut et al. [4]

An example of the results from the exergy analysis is given in Figure 4-36 as a Sankey diagram of the exergy flows. The reactant and product streams' chemical exergy content was left out for purposes of clarity. The magnitude of the chemical exergy is much larger than the exergy destructions and transfers within the system. Only the net change in chemical exergy is plotted for the product stream (in color of green). The thermomechanical exergy streams are shown in orange color. Exergy destruction streams are shown as purple. The corresponding component exergy efficiencies and rate of exergy destruction are given in Table 4-7.

Table 4-7 Reactor and heat exchanger exergy efficiencies and rates of exergy destruction (20161021 on-sun data, 820°C, 0.048 mol/s CH_4, S/C 2.2).

Symbol	*Component*	*Exergy Efficiency*	*Rate of Exergy Destruction, kW*
EV	Vaporizer	22.9%	5.39
SMR	Solar Methane Reformer	90.2%	5.34
LTR-M	Methane Preheater	99.2%	0.734
HTR	High Temperature Recuperator	99.8%	0.226
LTR-W	Water Preheater	99.7%	0.152

From Figure 4-36, the solar methane reforming reactor hosts the largest exergy destruction. Certain amount of exergy destruction cannot be avoided when photons are absorbed by the reactor and converted to heat. The magnitude of this destruction is determined by surface temperature, which is constrained by material properties. Better concentrators can potentially operate the reactor at higher temperature but reactor materials of construction will pose a limit. At the particular on-sun test conditions that were plotted, this first stop exergy destruction was about 2.9 kW, or 26% of the incident solar power.

Additional exergy destruction occurs inside the reactor due to departure from reaction equilibrium in the catalyst channel and departure from reversible heat transfer at the internal recuperative heat transfer interface. Some small amount of exergy loss was flow related. Other heat exchangers in the reaction system have much smaller exergy destruction. The contribution by the reactor accounts for about 70% of all these combined, excluding the initial photo-to-heat exergy destruction and the portion at water vaporizer.

While future versions of the system will receive heat from other sources, the heat for water vaporization in this prototype system came from electrical resistance heating. Because the steam generation was done at a fairly low temperature of 150°C to 200°C, large exergy destruction is inevitable when heat input was provided by electricity. From Table 4-7, clearly steam generation had the largest exergy destruction, followed by the SMR reactor itself. In follow-on projects, such as one where we will optimize the system for hydrogen production, we intend to provide heat from a water-gas shift reaction and from additional latent heat from the reformate stream.

From the above analysis, it is clear that the solar methane reforming reactor and steam generation should be the focus of further development for reaction system exergetic efficiency improvements. In addition, improvements to the dish-concentrator will be investigated. All existing recuperative heat exchangers, including the HTR, already performed very well at exergetic efficiencies over 99%. However, as their cumulative exergy destruction was in excess of 1 kW, additional improvements in efficiencies may be possible.

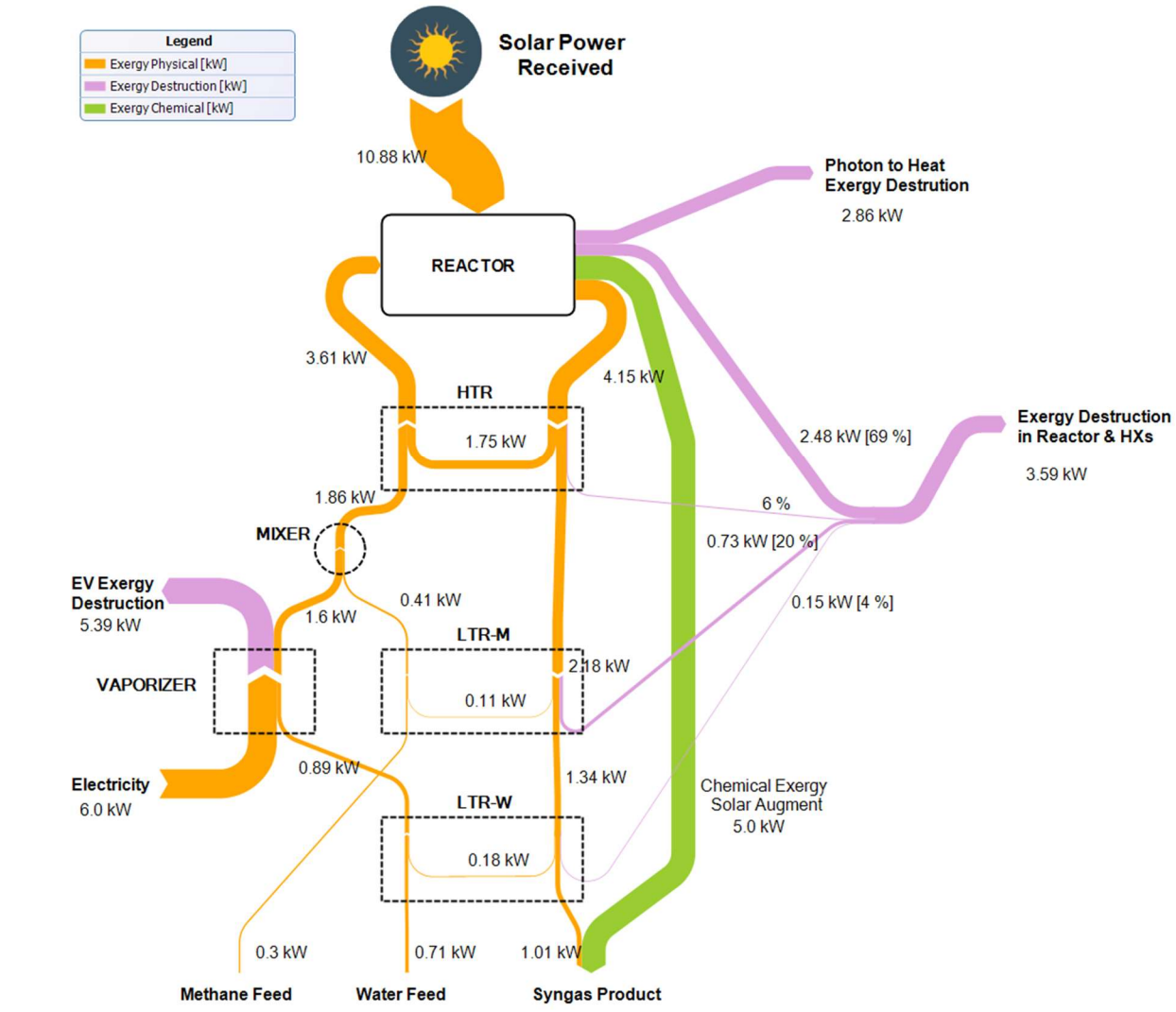

Figure 4-36 TRL 6 reaction system exergy flows and destructions (stream data from 20161021 on-sun measurements at 820°C, 0.048 mol/s CH_4, S/C 2.2).

5.0 Manufacturing Development

The general approach for manufacturing development is to develop process-based cost models for the custom components. By comparing cost-volume curves for alternative manufacturing processes, the low cost option can be selected for a given production volume. Cost models for key components of the solar thermochemical reaction system were developed under this task. The general approach is outlined in the next section and the results are given for each key component type: reactors, recuperative heat exchangers, and dish concentrators.

5.1 Approach

The cost model development starts with identifying the sequence of manufacturing steps starting from raw materials to a completed component. Costs are identified for each step including raw materials, equipment and maintenance, facility (based on footprint), labor, consumables, and utilities. Costs for each step are rolled-up into a cost-of-goods sold that is a function of production volume, which can then be used to produce cost-volume curves. Process-based cost models are needed for optimizing cost-performance in designing components and of the overall SMR system.

The process-based cost models assume dedicated line manufacturing of high production volumes of a mature market. However, in the near-term, lower volume manufacturing is needed for product and market development, which will favor established supply chains, lower capital outlays, and flexible manufacturing processes that can adapt to evolving designs and product evolution.

Both long-term and near-term manufacturing development and equipment cost estimates rely on detailed designs of components. Manufacturing cost estimates had been generated previously, based on evolving reaction system design from TRL 4 to TRL 6 with feedback to the component development task. Cost models results based on earlier designs had been reported in project phase reports. This report provides the latest TRL 6 design and its associated cost estimates.

Validation of manufacturing cost models and process capability is performed through building and testing of Process Development Vehicles (PDV) and Technology Development Vehicles (TDV) using candidate fabrication processes. The objective of PDVs is to perform statistically relevant experiments in order to validate process capability—the ability for a process to meet design requirements such as tolerances—and to validate cost model parameters, such as cycle times, processing speeds, or process yields that impact manufacturing costs.

5.2 Overview of Phase 1 Manufacturing Development

5.2.1 Manufacturing Development

Manufacturing development was continued through all three phases of this project. In Phase 1, manufacturing development activities were initiated. A baseline system cost estimate for a commercial solar thermochemical reforming system at a scale projected for a 100 kWt solar parabolic dish concentrator was developed. The projection was based on scale-up of components in the TRL 4 demonstration system where appropriate and a bill-of-materials for components needed in a commercially

mature system. A pareto analysis of the cost breakdown revealed that the equipment cost was dominated by the two high-temperature components, the reactor-receiver and the high temperature recuperator (HTR), both requiring construction from expensive alloys to operate above 750°C.

For the reactor-receiver, two approaches for cost reduction were identified to reduce the amount of material and to enhance performance instead of refining or considering alternative manufacturing processes. As a consequence, further manufacturing development of the reactor-receiver was deferred to Phase 2 when the reaction system design was improved.

For the HTR heat exchanger, the other dominant system cost driver, microchannel process technology was used to reduce the size and weight of the device in order to meet the compact footprint requirement necessary for installing near the focal point of the dish concentrator. Phase 1 activities were focused on reducing cost of the HTR through an alternative design concept, called "half array" architecture, as described below. This began with an apples-to-apples cost comparison of equivalent heat exchanger designs that showed significant cost savings of over 70% associated with higher material utilization. PDV work was initiated and focused on manufacturing process development for this alternative design approach with the aim of continuation to TDV and prototype development in the next phases of the project.

5.2.2 Solar Thermochemical Reaction System Cost

A bill-of-materials (BOM) was compiled in order to generate a baseline equipment list for an on-sun thermochemical reforming system and to derive costs for components and for assembly that can be rolled up into a manufactured system cost estimate. The BOM was derived by starting with the component list of the TRL 4 demonstration system and removing those components determined as unnecessary for a mature, commercial system and retaining those that are critical for operating and controlling the system. Costs were also reduced by replacing high cost components of versatile functions suitable for research and development with dedicated industrial components.

Baseline cost-of-goods-sold (COGS) for the system based on the TRL 4 system design was developed. Purchase costs were used for off-the-shelf components based on catalogue or vendor quotes with no attempt to take credit for volume pricing at this stage. Assembly cost was estimated by estimating hours and labor rate. The highest cost items identified were the unique systems components, which were estimated using process-based cost modeling tools and the TRL 4 component designs.

The unique components of the system were the steam methane reforming reactor-receiver, the high-temperature recuperator (HTR), the water vaporizer, and the low-temperature water and natural gas preheaters. These items were not off-the-shelf components and a manufacturing supply chain will be required for transitioning the technology to market. The two highest cost components in the system were identified as the reactor-receiver and the HTR heat exchanger, which must be made from expensive high-temperature alloys such as Haynes or Inconel. The TRL 4 demonstration system was estimated at $324/kWt. However, over 80% of the costs were associated with the two high-temperature components. The substantial opportunities to reduce these component costs through design evolutions and design for manufacturing were the focus of the next phases of the project.

5.2.3 Cost Modeling of the HTR Heat Exchanger

HTR cost-volume curves were generated using cost models developed for laminate architectures. While the component in the TRL 4 prototype system was made using a selective laser sintering process, the design can be manufactured using stacked laminate processes, such as photochemical machining and stamping to pattern the shims and diffusion brazing for assembling the stack of lamina into a hermetic component.

The costs were built bottom-up from detailed process cost models for each step in the manufacturing process. In this case, photochemical machining was selected for patterning the lamina and diffusion brazing was used to bond the shim stack into a hermetically sealed device. The cost model assumed a green-field facility and a dedicated manufacturing line. Costs associated with tools, facility space, labor, consumables, utilities, and maintenance were identified for each processing step and rolled up into for the entire manufacturing cost. The end result was an estimate for cost-of-goods-sold that was highly dependent on and sensitive to the original component design. The microchannel HTR cost curve suggested that production reached high tool and labor utilization when volume exceeded about 1000 devices/year. Over 90% of the HTR manufacturing cost was associated with raw material costs. This implied that future designs should target higher raw material utilization and/or low-cost materials of construction.

5.2.4 Alternative HTR Design Concept

Approaches considered for reducing the cost of the HTR included using a lower cost material than Haynes high temperature alloys; utilizing alternative manufacturing processes that have lower material waste, such as additive manufacturing; or considering alternative heat exchanger designs.

The project chose to pursue an alternative heat exchanger concept that was developed for higher material utilization and lower cost manufacturing processes. The ‘half-array’ design concept was invented by Oregon State University on another project. In addition to higher material utilization and lower-cost manufacturing processes, the design also has better mechanical durability in temperature cycling. In the OSU prior work, a detailed cost model was developed for the half-array design that uses stamping and laser welding manufacturing processes. Equivalent designs with comparable thermal performance and pressure drop were completed for both the microchannel laminate architecture and the half-array concept. Dramatic reduction of starting raw material needed was achieved with the half-array design compared to conventional microchannel laminate design. Cost estimates showed a 70% reduction in equipment cost. The cost per kW of duty decreased from $631/kW to $192/kW. The savings were almost all due to increased material utilization with the half-array design.

While the comparison was not performed with specifications for the solar thermochemical system, the conditions and duty were reasonably close and the cost savings were expected to be representative. Based on these results, the half-array concept was chosen as the technology to carry forward in HTR manufacturing development.

5.2.5 Process Development Vehicles

PDV work in Phase 1 focused on the half-array technology for the HTR with the purposes of validating parameters having the highest sensitivity in the cost models and developing those processing steps with the most uncertainty. The manufacturing steps for a half-array device were to form the parts for the half-array stack (plates and microchannel flow inserts); stack and join the plates together at the seams and around the headers; form the housing; and assemble the half-array assembly into the housing. The steps that were selected for the PDV work were the welding of the plates and the forming of the microchannel flow inserts. These steps were the most unique to half-array manufacturing and were the least well-developed steps. They were very critical to the structural and thermal performance of the device and were also important cost drivers.

In Phase 1, a PDV study for laser welding process development was designed. A test plan was developed to investigate the effects of laser power and weld speed on hermiticity, weld strength, and weld quality. A second PDV study was designed to focus on the forming of the microchannel flow inserts. The half-array technology places unique requirements on the strength and tolerances of fabricating the microchannel flow inserts. The testing was started in Phase 1 and scheduled to finish by the end of Phase 2.

5.3 Overview of Phase 2 Manufacturing Development

5.3.1 Down Select Manufacturing Processes

Down-selections of manufacturing processes were performed at the outset of Phase 2 for the reactor-receiver and HTR heat exchanger for low-volume production at 10-1000 per year and longer-term at volumes greater than 1000 per year. The processes were selected based on the then current TRL 5 and alternative designs, prior experience from comparing costs of alternative manufacturing processes, and cost modeling results from Phase 1.

For the reactor, the selected process for both near-term and long-term manufacturing was conventional CNC machining of parts, diffusion bonding of the reactor plates, and welding on of interconnects. Other processes required for the reactor were automated calcining, dip-coating, and heat treating of the catalysts pieces, and insertion of the catalyst pieces into the reactor. These processes were used for fabricating both the TRL 4 and TRL 5 reactors. Alternative processes that had been considered included selective laser melting (SLM) and injection molding and sintering to make the parts, which both require more expensive metal powder as the raw material but have lower material waste. The reactor design evolved significantly between TRL 4 and TRL 5 with substantial cost savings due to substantial reduction in raw material cost and switching to a lower cost alloy. This change diminished the appeal of the alternative process such as SLM from the raw material cost perspective. In addition, by remaining consistent with the fabrication of the TRL 4, TRL 5, and likely TRL 6 reactors, risks associated with adopting alternative manufacturing methods for the commercial products are avoided. There are established vendors for performing most of the steps, thereby minimizing the capital outlays required for creating in-house manufacturing in the near-term. In the longer-term costs can be reduced by bringing processes in-house by investing in manufacturing equipment including CNCs and vacuum-press furnaces.

For the high temperature recuperative (HTR) heat exchanger, the process selected for near-term manufacturing was SLM, an additive manufacturing technology, which is highly versatile and does not require 'touch' tooling that typically drives tooling and tool maintenance costs. The trade-off is higher material costs associated with the expensive metal powders used by the process, but material utilization is high compared to subtractive technologies. The versatility of the process makes it attractive for adopting design changes as the technology evolves. For long-term high-volume manufacturing of the HTR heat changers, the half-array heat exchanger technology was selected. The half array architecture was identified in Phase 1 as having a lower cost for high-volume production than conventional diffusion-brazed microchannel heat exchangers.

5.3.2 Cost Modeling

In Phase 2, cost model components for the selected reactor manufacturing processes were developed. Development of a cost model for CNC milling was initiated. Cost models for diffusion brazing and welding were identified as available from previous efforts. The completion of CNC milling cost models and the application of all of the component cost models to the reactor design was scheduled to finish in Phase 3.

Parameters for the SLM process cost elements were obtained, including raw materials, equipment and maintenance, facility (based on footprint), labor, consumables, and utilities, from vendor quotes, literature, and actual procurements of SLM heat exchangers used for reaction system testing. Preliminary SLM cost calculations were made for TRL 5 HTR heat exchangers. Development of a complete SLM cost model as well as applying the cost model to the HTR heat exchangers and the reactor-receiver was scheduled to complete during Phase 3.

A detailed cost model for stamping and laser welding of the half-array HTR heat exchangers was developed in Phase 1. Progress was made in Phase 2 to validate the cost model through interactions with a stamping vendor and through TDVs.

5.3.3 Technology Development Vehicles (TDV)

Phase 2 work scope included building and testing TDVs to validate that components built using the selected manufacturing processes will meet performance requirements and also to validate cost model parameters. TDV work was initiated during Phase 2 and completed in Phase 3.

5.4 Overview of Phase 3 Manufacturing Development

5.4.1 Reactor and HTR Heat Exchanger Cost Models

The manufacturing development activities initiated from previous phases were completed in Phase 3. These included the development of reactor and HTR heat exchanger cost models and the application of these models to the TRL 6 reactor design. The TDV performance and cost model validation was completed for the selected manufacturing processes.

5.4.2 Dish Concentrator Cost Models

New in Phase 3, baseline cost models of the PD3 dish concentrator with original Infinia mirror segments were developed. Cost models of additional dish concentrator configurations were also developed, including the large PD4 dish with better optical performance and variations of PD3 and PD4 on mirror size and types.

5.5 Reactor and HTR Heat Exchanger Cost Models

The reactor cost models described below were based on the latest TRL 6 design, which was paired to the PD3 dish concentrator. The reactor material of construction was Haynes 230 alloy. The HTR heat exchanger material was Inconel 625 alloy. Alternative manufacturing methods were modeled for both the reactor and the HTR exchanger. Fabrication of the reactor plates was by conventional machining or by additive manufacturing. The HTR exchanger was evaluated for both additive manufacturing and the half-array concept.

5.5.1 Reactor Manufacturing with Machining

In this reactor cost model, annual production of 10 to 10,000 units per year was evaluated. Reactor plates were fabricated by machining, laser cutting, and photochemical machining. Joining of the parts were accomplished by laser welding of interconnects and diffusion brazing of the plates. The cost model results, cost per good assembly and capital investment at different annual production rates, are shown in Figure 5-1. Cost breakdown by process steps and cost categories are shown in Figure 5-5 and Figure 5-3, respectively, at 50 to 10,000 units per year. At low volume production, material costs are not very important because fabrication tooling costs dominate the reactor cost. As product volume increases from medium to high volume, material costs rises to nearly half of the reactor unit cost. Machining process takes up about 50% of the reactor cost. Other fabrication costs such as diffusion bonding and laser cutting and welding drop to less than 10% of total costs as the tooling utilization of these high capital cost items improve.

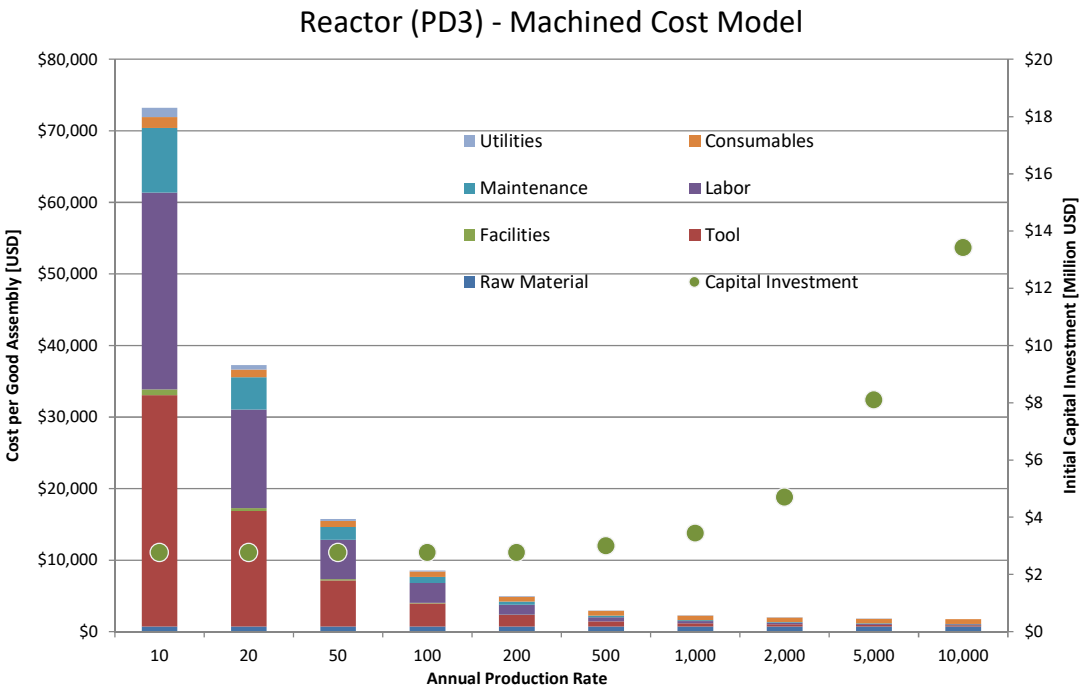

Unit Cost	$73,230	$37,301	$15,743	$8,557	$4,964	$2,940	$2,288	$1,996	$1,807	$1,735
Ave. Tool Utilization	7%	7%	8%	9%	12%	14%	16%	16%	18%	21%
CNC Milling	13%	17%	27%	44%	79%	96%	96%	96%	96%	98%
Visual Inspection	5%	5%	5%	5%	5%	6%	7%	9%	15%	24%
PCM Chemical Etch	10%	10%	10%	10%	10%	11%	12%	14%	20%	29%
Diffusion Brazing	6%	6%	8%	11%	18%	37%	70%	70%	86%	97%
Labor Utilization	0%	0%	1%	2%	5%	11%	20%	32%	52%	67%

Figure 5-1 Reactor cost model results based on machining manufacturing and PD3 reactor size.

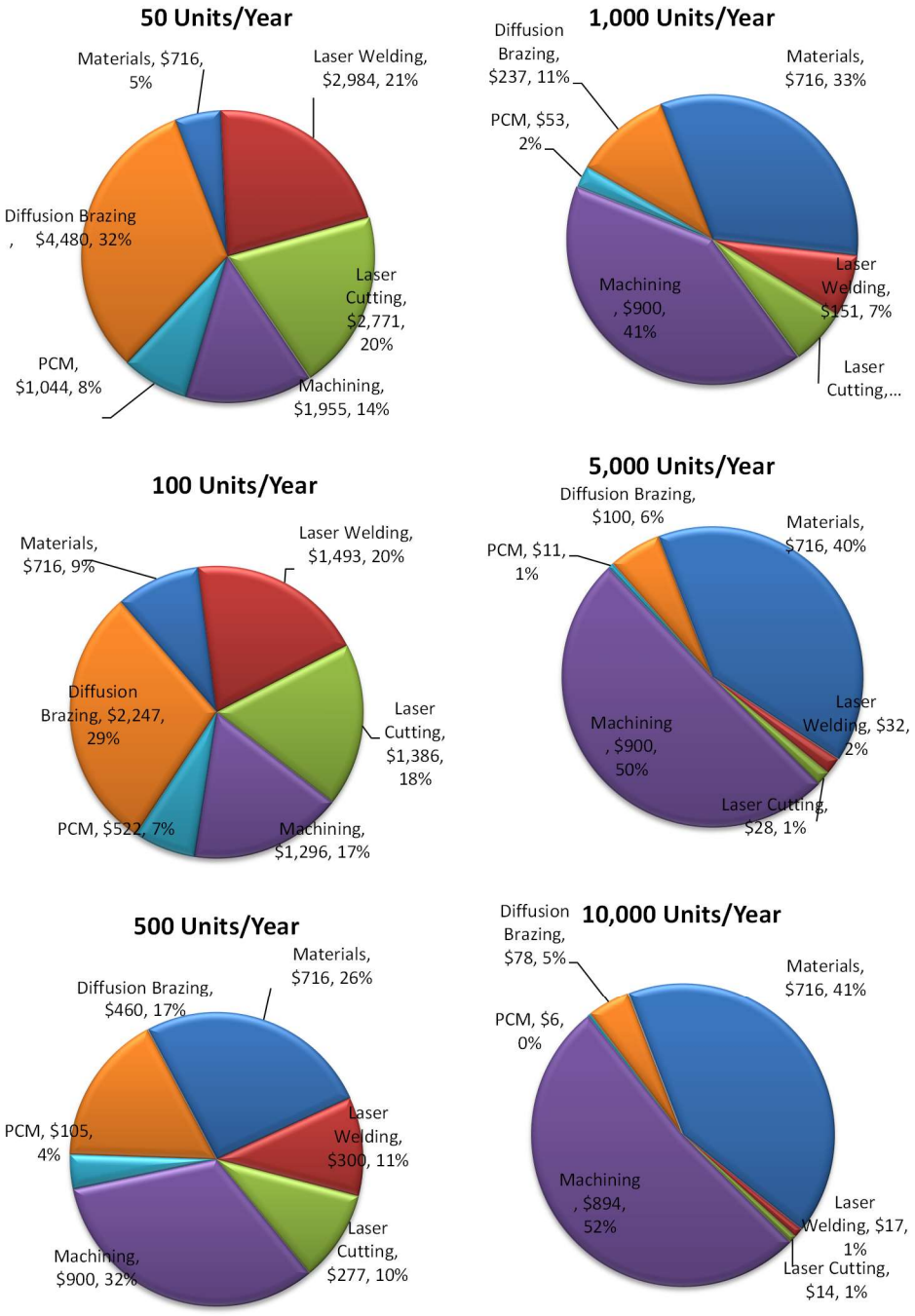

Figure 5-2 Reactor cost breakdown by manufacturing steps (machining manufacturing and PD3 reactor size).

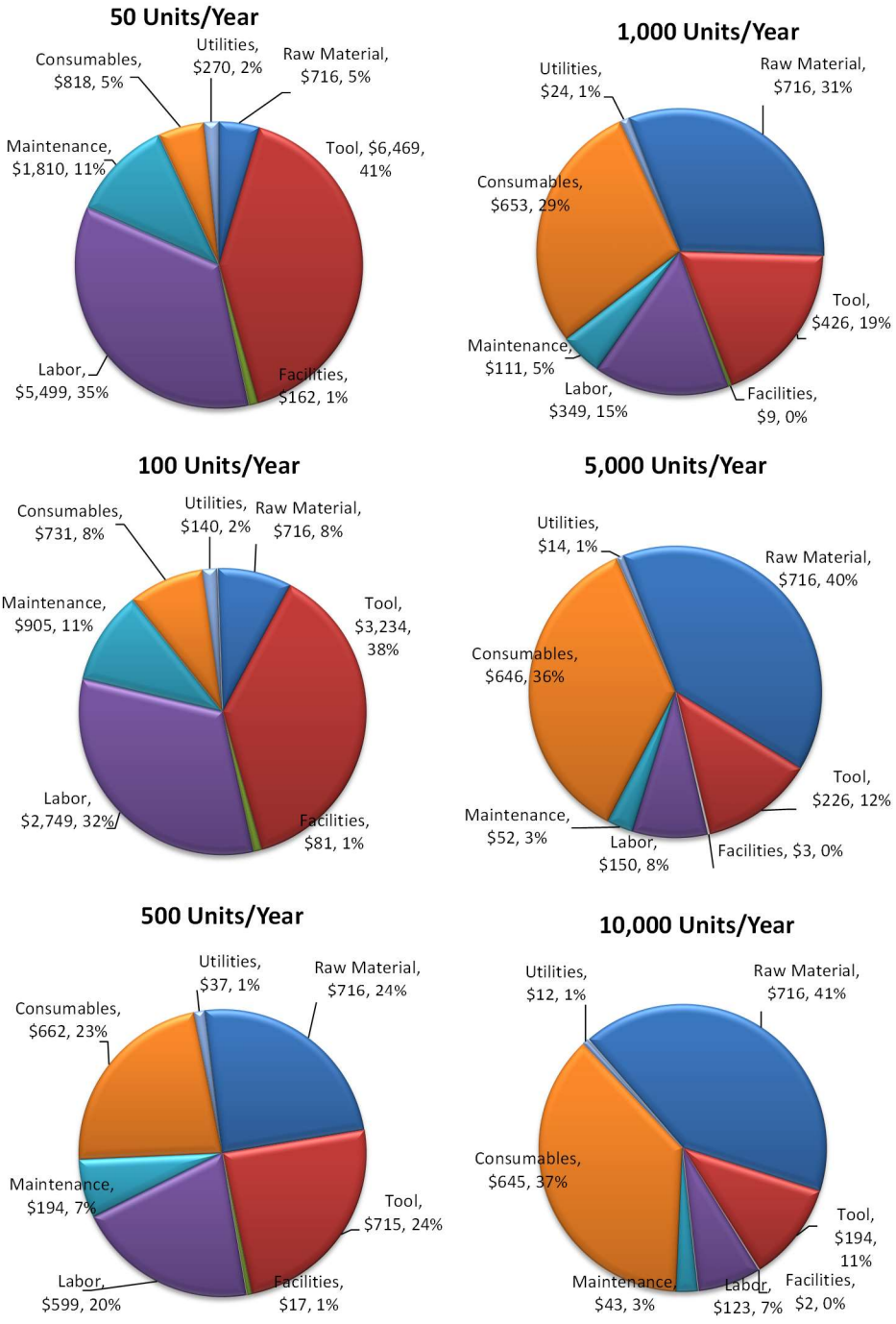

Figure 5-3 Reactor cost breakdown by cost categories (machining manufacturing and PD3 reactor size).

5.5.2 Reactor with Additive Manufacturing

In this reactor cost model, annual production of 10 to 10,000 units per year was evaluated. Reactor plates were fabricated by machining, laser cutting, and photochemical machining, with the exception of

the front plate being fabricated by additive manufacturing. Joining of the parts were accomplished by laser welding of interconnects and diffusion brazing of the plates, same as previously described. The cost model results, cost per good assembly and capital investment at different annual production rates, are shown in Figure 5-4. Cost breakdown by process steps and cost categories are shown in Figure 5-5 and Figure 5-6, respectively, at 50 to 10,000 units per year. The fraction cost due to raw materials scales up with production volume, similar to the machined reactor case.

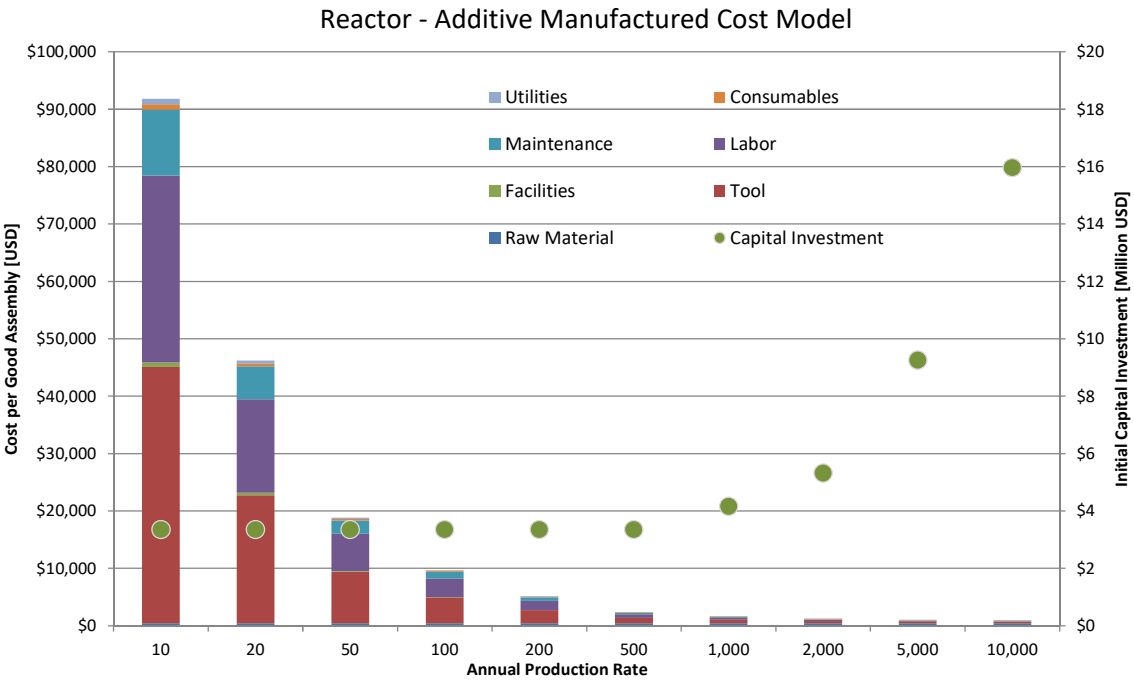

Unit Cost	$91,833	$46,218	$18,849	$9,727	$5,165	$2,428	$1,682	$1,269	$1,037	$969
Average Tool Utilization	7%	7%	7%	8%	9%	12%	14%	16%	20%	23%
CNC Milling	10%	10%	10%	11%	12%	15%	19%	29%	57%	57%
Additive Manufacturing	11%	12%	16%	22%	34%	70%	70%	89%	95%	95%
PCM Chemical Etch	10%	10%	10%	10%	10%	11%	12%	14%	20%	29%
Diffusion Brazing	6%	6%	8%	11%	18%	37%	70%	70%	86%	97%
Labor Utilization	0%	0%	0%	1%	2%	4%	8%	15%	31%	47%

Figure 5-4 Reactor cost model results based on additive manufacturing and PD3 reactor size.

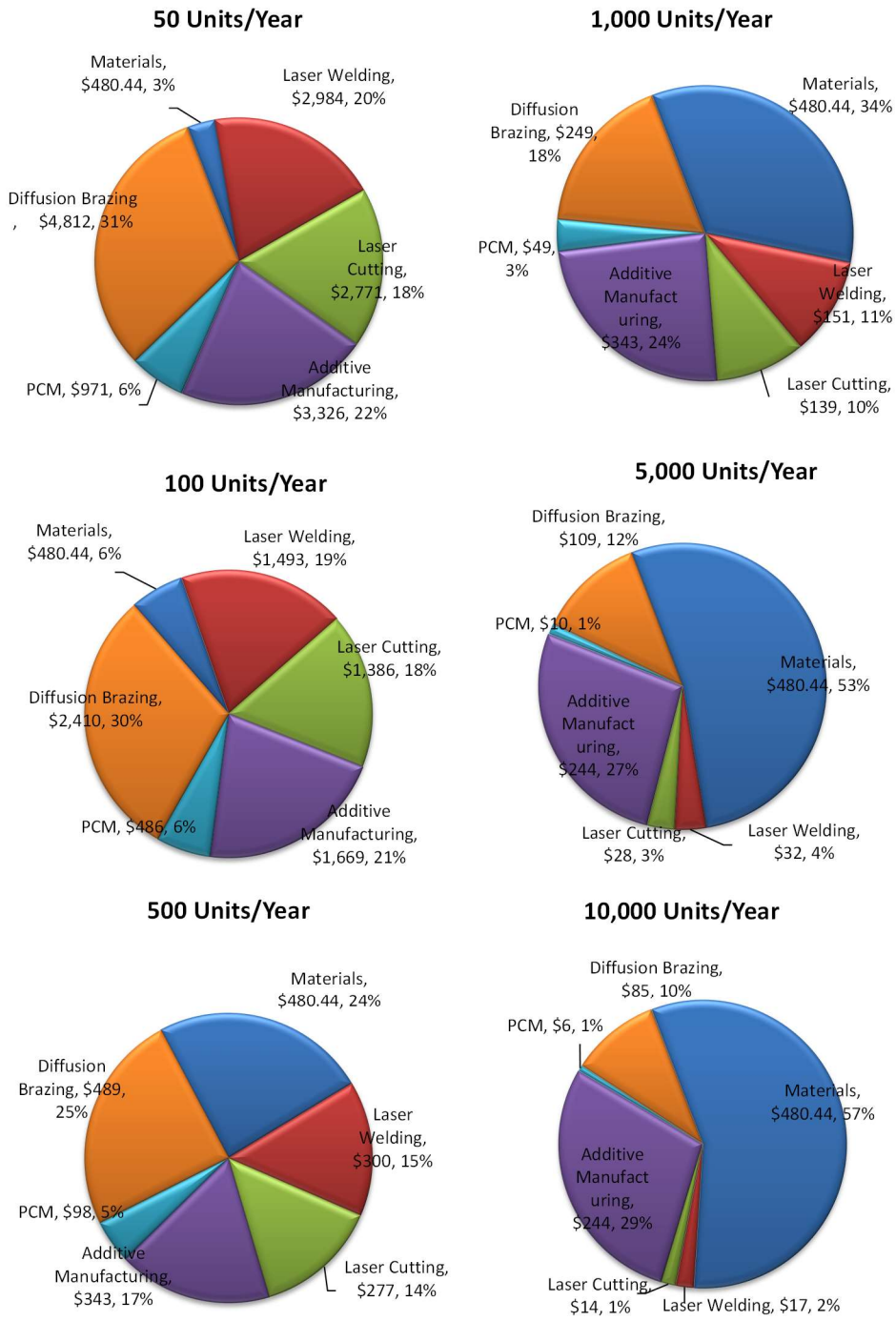

Figure 5-5 Reactor cost breakdown by manufacturing steps (additive manufacturing and PD3 reactor size).

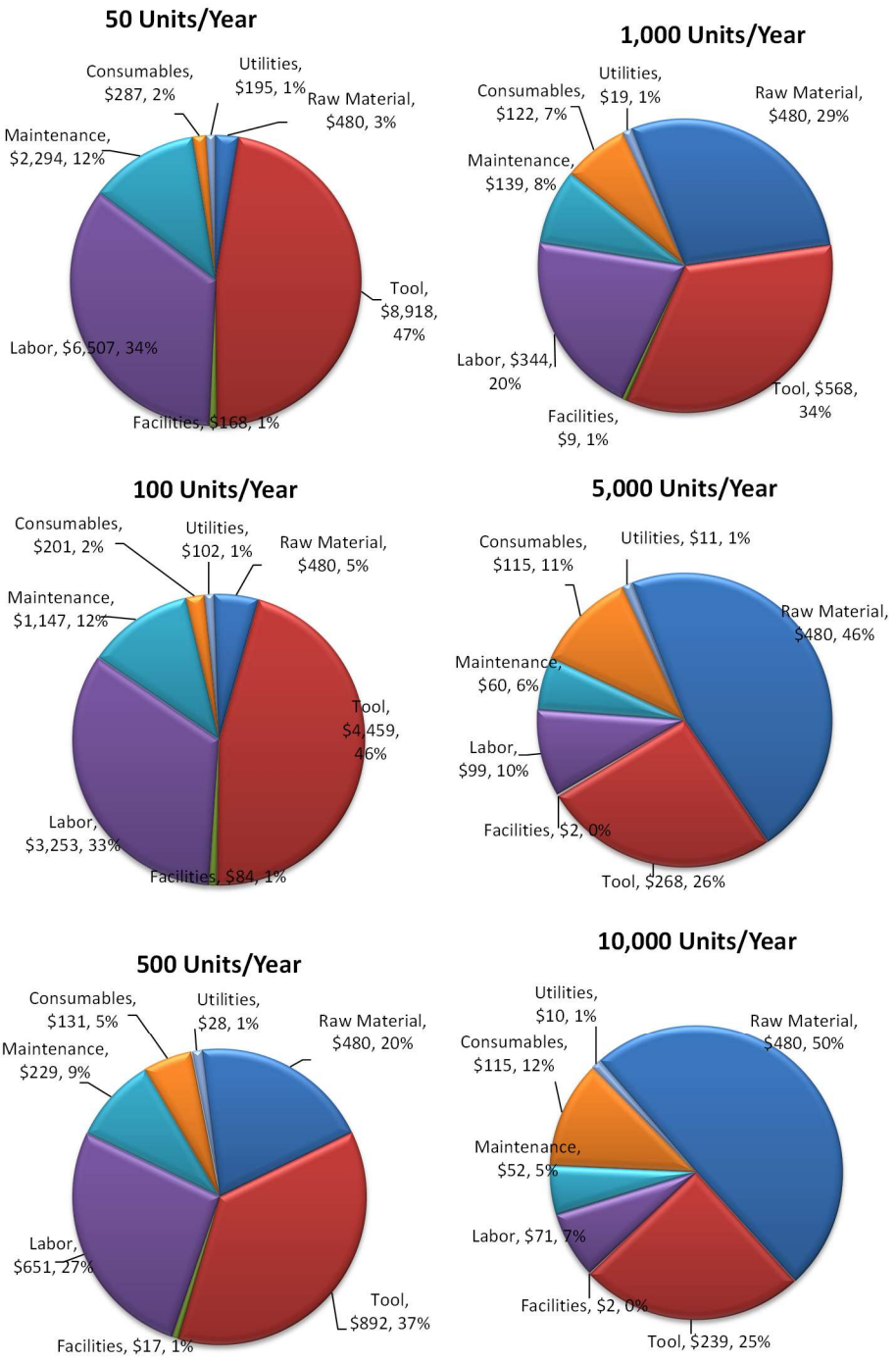

Figure 5-6 Reactor cost breakdown by cost categories (additive manufacturing and PD3 reactor size).

5.5.3 HTR Heat Exchanger with Additive Manufacturing Method

In the HTR heat exchanger cost models, annual production of 10 to 10,000 units per year was evaluated. The HTR devices were fabricated by additive manufacturing and post processing EDM cutting. The cost model results, cost per good assembly and capital investment at different annual

production rates, are shown in Figure 5-7. Cost breakdown by process steps and cost categories are shown in Figure 5-8 and Figure 5-9, respectively.

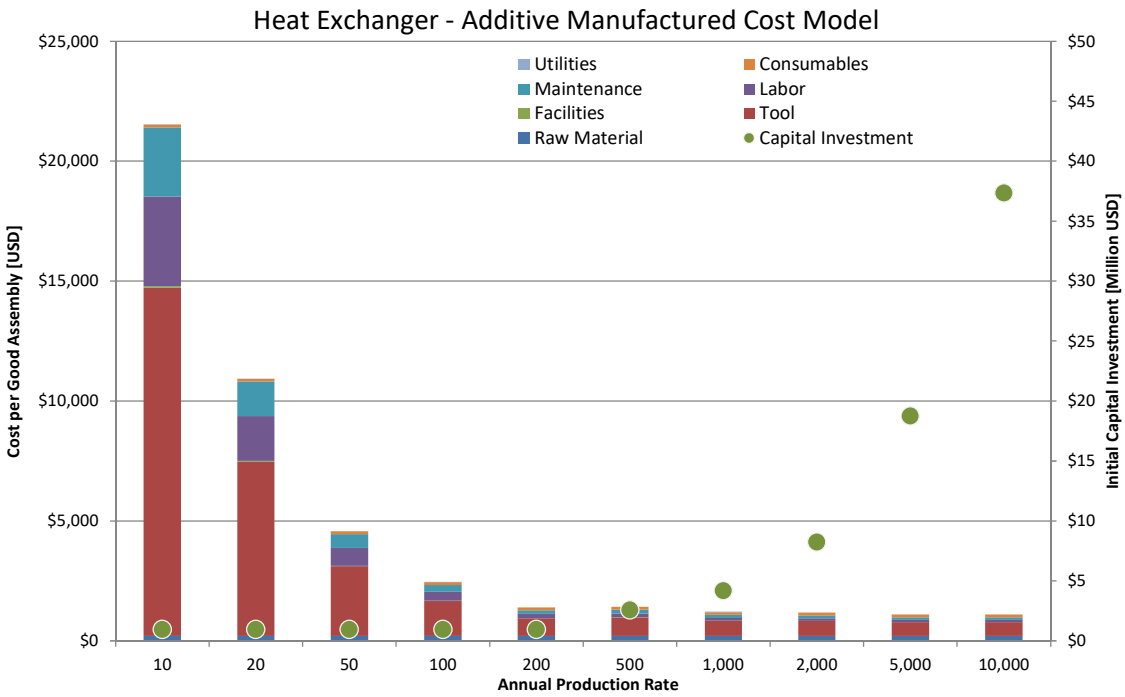

Unit Cost	$21,538	$10,937	$4,577	$2,457	$1,397	$1,424	$1,212	$1,189	$1,109	$1,104
Additive Mfg	9%	14%	27%	48%	91%	73%	87%	86%	93%	93%
Post processing	5%	5%	5%	5%	5%	5%	5%	6%	7%	10%
Labor Utilization	2%	4%	11%	22%	43%	54%	72%	78%	89%	91%

Figure 5-7 HTR cost model results based on SLM additive manufacturing.

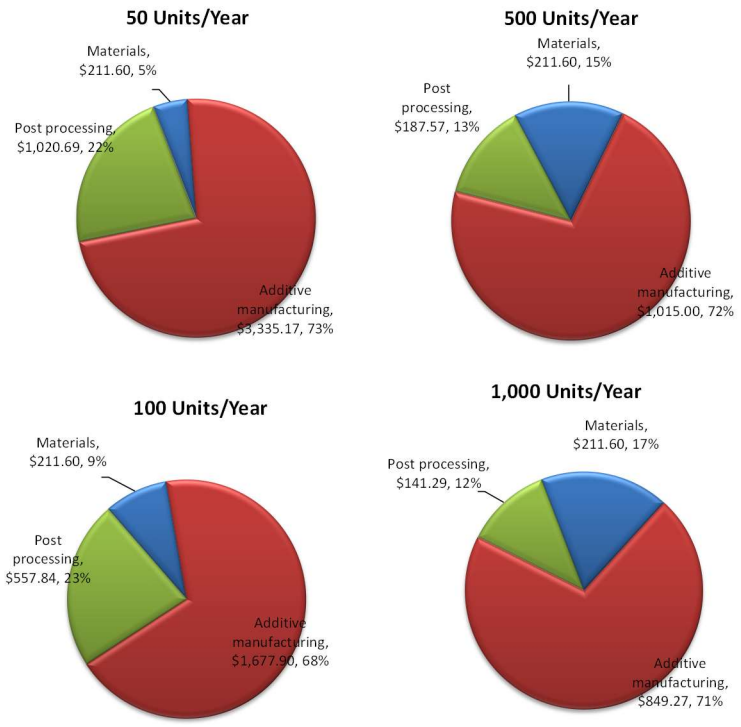

Figure 5-8 HTR cost breakdown by manufacturing steps (additive manufacturing).

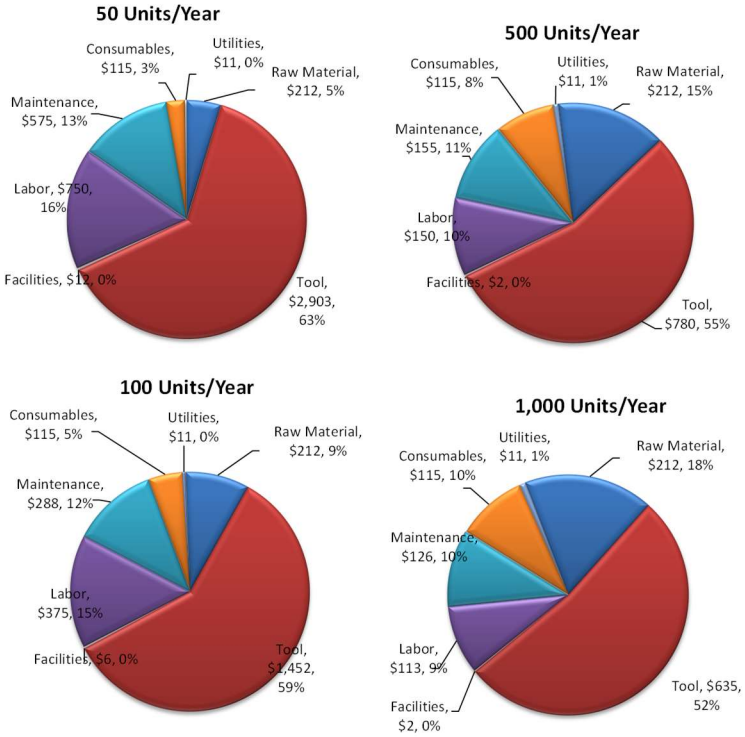

Figure 5-9 HTR cost breakdown by cost categories (additive manufacturing).

5.5.4 HTR Heat Exchanger Manufacturing with Half-Array

In the HTR heat exchanger cost models, annual production of 10 to 50,000 units per year was evaluated. HTR devices were fabricated by the half array architecture involving high volume forming and laser welding. The cost model results, cost per good assembly and capital investment at different annual production rates, are shown in Figure 5-10. Cost breakdown by process steps and cost categories are shown in Figure 5-11 and Figure 5-12, respectively.

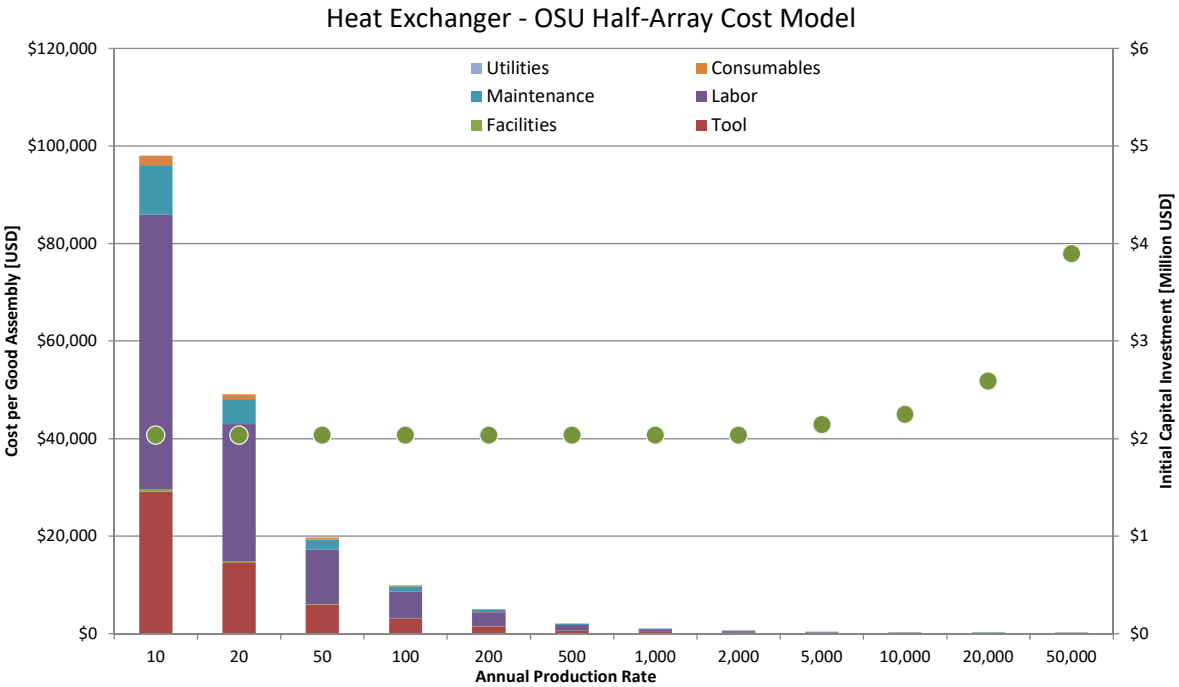

Total	$98,001	$49,055	$19,687	$9,898	$5,003	$2,066	$1,087	$598	$316	$218	$174	$149
Average Tool Utilization	5%	5%	5%	5%	6%	6%	8%	11%	15%	22%	28%	40%
MFI Press Utilization	5%	6%	6%	8%	10%	18%	30%	56%	68%	89%	89%	95%
4-Post 70 Ton Press	5%	5%	5%	5%	5%	6%	7%	9%	16%	26%	47%	58%
MFI Annealing Furnace	5%	5%	5%	6%	6%	8%	10%	15%	30%	56%	56%	89%
Weld Cleaning Station	5%	5%	5%	5%	5%	6%	7%	10%	16%	28%	50%	61%
Labor Utilization	0%	0%	0%	0%	1%	1%	3%	5%	13%	24%	38%	61%

Figure 5-10 HTR cost model results based on half array architecture.

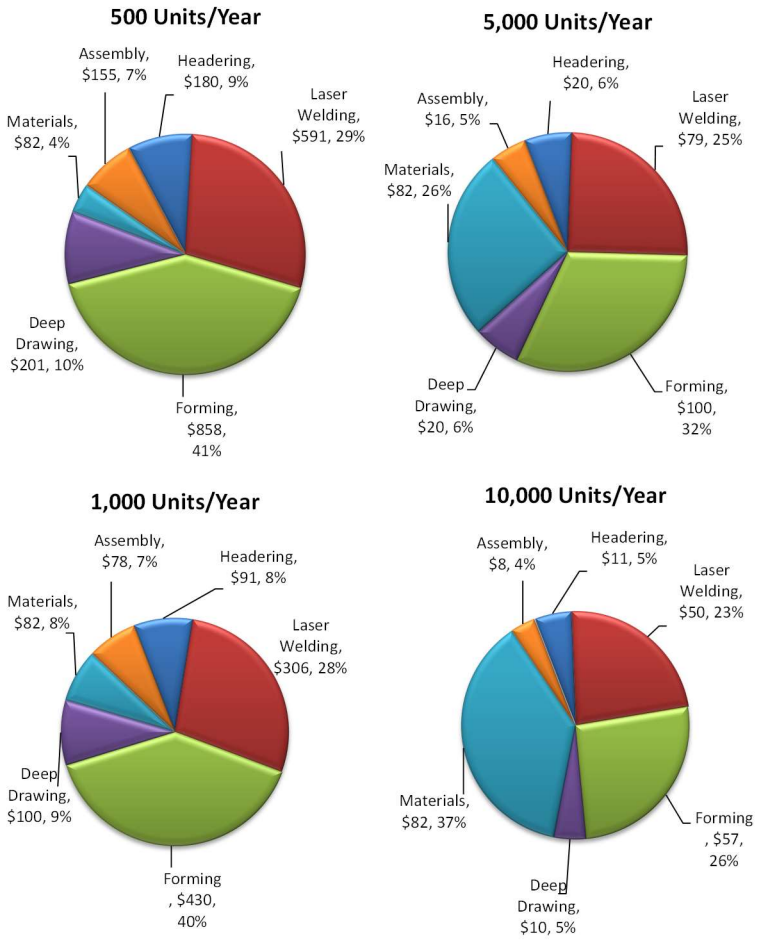

Figure 5-11 HTR cost breakdown by manufacturing steps (half array architecture).

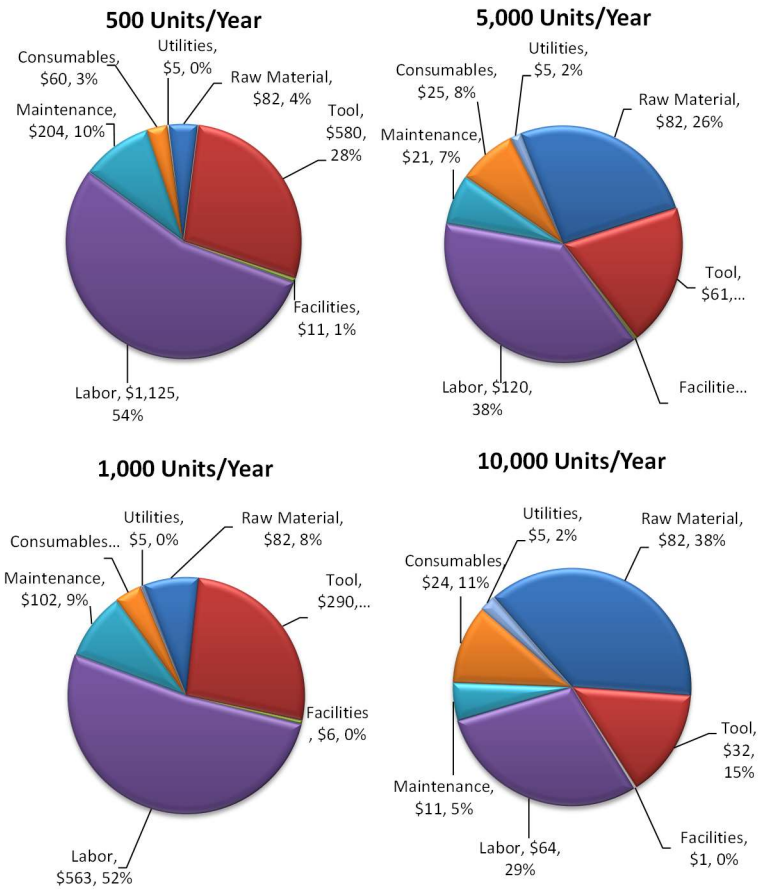

Figure 5-12 HTR cost breakdown by cost categories (half array architecture).

5.5.5 Combined Reactor and HTR Heat Exchanger Models

It is useful to examine the previous cost-volume estimates from the TRL 6 based reactor and HTR heat exchanger cost models together. Because these two components are of the highest costs among reactor system components, the reactor system cost-volume curve can be reasonably well understood from the collection of individual cost curves, as shown in Figure 5-13.

The costs per good assembly of both the reactor and the HTR exchanger drop rapidly when scaling the production rate from low to medium volume. The "knee" of the reactor cost curve based on the selected manufacturing method, i.e. by machining, is at about 1,000 units per year. The cost model for reactors partially built with additive manufacturing produced a "knee" on the cost curve at several thousand units per year. According to the projections by the HTR heat exchanger cost model for the selected near term manufacturing method, i.e. additive, the HTR costs are not sensitive to production rate beyond about 200 units per year. Base on the above results, a production volume of 1,000 systems per year is thus a good scale target for initial field demonstration and market development. Ramping to 1,000 – 10,000 systems per year, the half array HTRs and additive manufactured reactors provide additional cost savings to help the technology to become adopted at commercial scale.

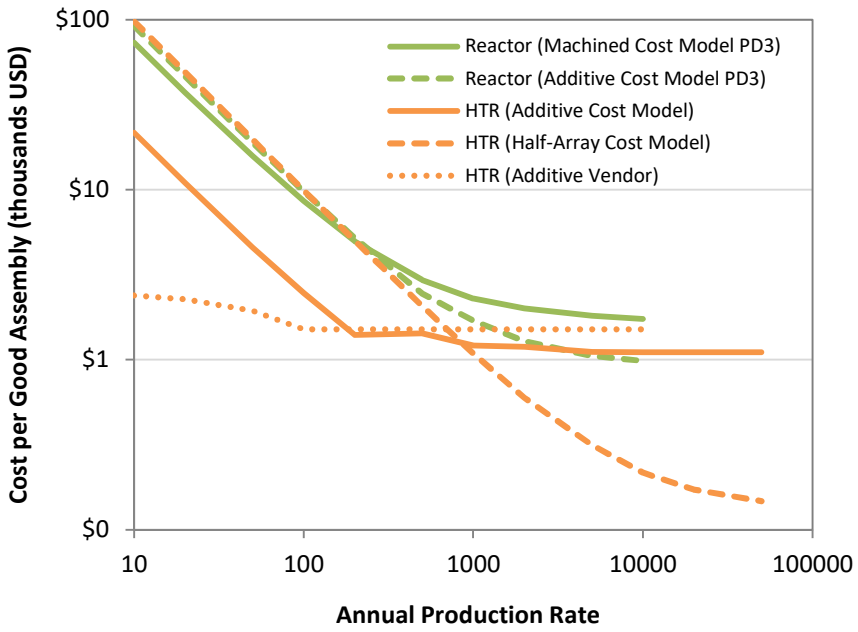

Figure 5-13 Comparison of volume-cost curves of reactor and HTR heat exchangers.

5.6 Dish Concentrator Cost Models

The dish concentrator cost models were developed for the Infinia PD3 baseline system and a number of other configurations. The modeled systems are listed in Table 5-1. The 3D CAD models of the PD3 and PD4 dish concentrators are shown in Figure 5-14 for comparison. PD4 cost data were compiled from previous work by Infinia. The PD4 installation costs were reworked by removing electrical infrastructure not needed by the PNNL solar thermochemical reaction system. The PD3' is a scaled down version of the PD4 to match PD3's mirror size. The Solartron cost curves are included for comparison: its 4.5m dish is similar in size to PD3; the 9m dish is somewhat larger than PD4. Also included is a curve for the PD4 concentrator, but scaled to use the Solartron cost curve. The cost-volume curves are shown in Figure 5-15. The costs per square meter of concentrator vs. production volume are shown in Figure 5-16.

The cost curves suggest that PD4 provides significant cost advantage over the PD3 and the PD5. Scaling up the reaction system developed on this project from PD3-size (14.85 m^2) to PD4-size (23.5 m^2) appears to be a relatively small leap. PD4 size dish may be a good candidate for follow-on development of the first commercial field demonstration.

However, it should be noted that the optimal selection for the dish concentrator also depends on the performance trade-off between the dish and the reaction system, which was not considered by the dish concentrator cost models here, neither by the reactor component models in earlier sections. An example of such trade-off is that the concentrator peak flux and flux gradient specifications determine the severity of hot spots on the reactor face, thus a better but more expensive concentrator may enable the use of a less expensive alloy with lower temperature rating. On the other hand, a reactor built from more expensive high temperature alloys can operate with a lower performance, presumably less expensive dish concentrator. More analysis of the integrated dish-reactor system will be needed to understand these

tradeoffs, which is beyond the scope of this work and is thus recommended for further investigations in follow-on projects.

Table 5-1 List of dish concentrator configurations for cost model development.

	Infinia PD 3	*Infinia PD 4*	*Scaled Down PD 4*	*Infinia PD 5*	*Solartron 4.5m*	*Solartron 7m*
Slope Error (mrad)	4.02	2.95	~2.95			
Peak Flux (W/cm^2)	~80	~90	~90			
Area (m^2)	14.85	23.5	~14.85	43.2		
Solar Power (kW)*	10.79	17.08	10.79	31.40	11.5	25

**Solar Power with 850 W/m^2 DNI, 95% mirror reflectance, no receiver losses.*

Figure 5-14 PD3 and PD4 dish concentrator 3D CAD models.

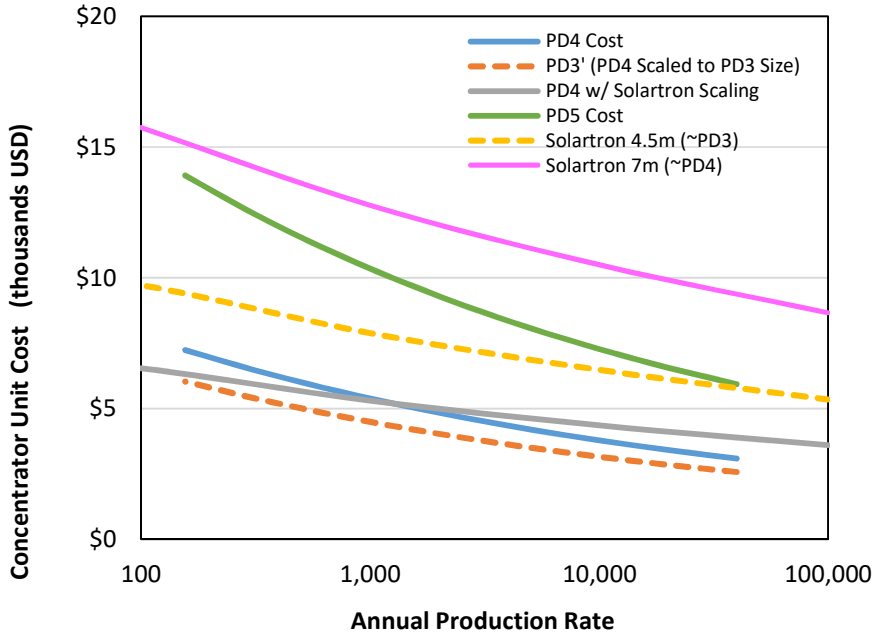

Figure 5-15 Dish concentrator unit costs over 100 to 10,000 annual production rate.

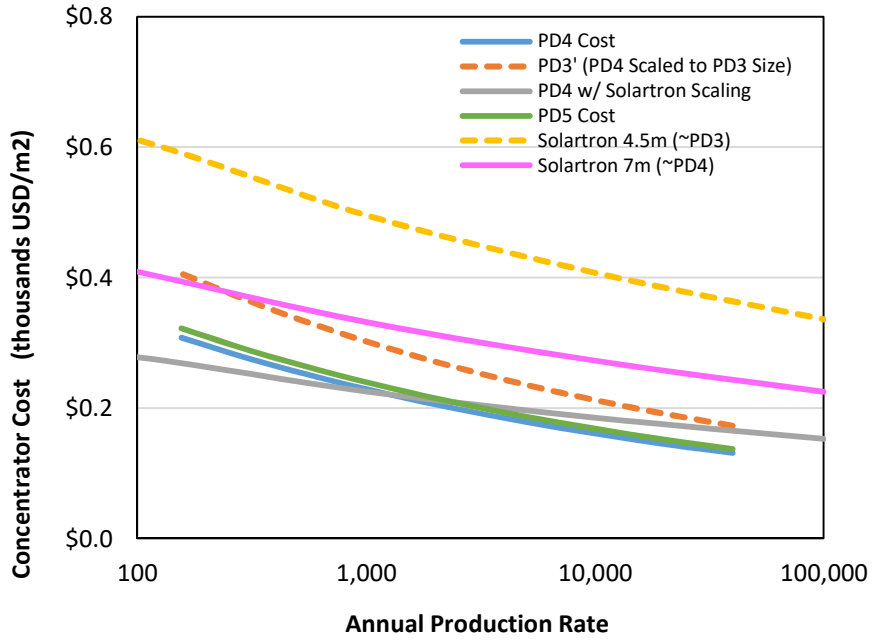

Figure 5-16 Dish concentrator unit costs per m^2 area over 100 to 10,000 annual production rate.

6.0 Technology to Market

6.1 Dish-STARS™ Transition Plan

6.1.1 Development of Business Strategy and Commercialization Plan

Throughout the three phases of this project, the objective of this activity was to investigate business strategies – including various value propositions – and commercialization plans for transitioning Dish-STARS™ as it was advanced throughout the project, and as it could be further developed after the project, to ultimate market deployment. While in Phases 1 and 2, power generation as part of a hybrid solar/natural gas powerplant was the focus, in Phase 3 DOE encouraged the project team to include potential nearer-term applications which, for various reasons, could more readily lead to the power generation applications through a staged approach. This ultimately proved to be the favored commercialization plan.

During Phase 3, technology-to-market project efforts were performed in conjunction with the investigations under the DOE EERE Lab Corps Pilot Program, where the Dish-STARS™ platform was one of 14 technology platforms evaluated. During the first and second quarter of Phase 3, our Lab Corp team was populated with 1) the PI of this effort, 2) an "entrepreneurial lead" from within PNNL, and 3) an Industrial Mentor from outside PNNL.
Training was initiated for this team in September, 2015, to familiarize team members with the Lab Corps approach, which is based on Lean Startup Methodology including the use of what is called the "Business Model Canvas". The Business Model Canvas is initially populated with notional statements about the business opportunity including the value proposition, customers, partners, and other elements. See Figure 6-1. They are then treated as hypotheses to be tested through a number of mechanisms.

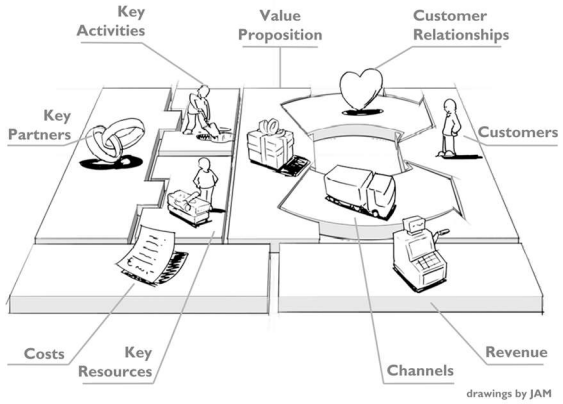

Figure 6-1 The Business Model Canvas: During the Lab Corps process, each element of the Business Model Canvas is populated with hypothesis about the business opportunity, with much of the subsequent Lab Corps effort being work to validate those hypotheses (or create improved ones).

After initial training, the Lab Corps effort transitioned to an intensive, six-week period led by an expert instructor team including business startup experts, a three-day opening session/workshop in October, 2015, weekly virtual sessions plus nearly daily exercises to validate and/or revise the hypotheses from the Business Model Canvas, and a two-day closing session in November, 2015. Figure 6-2 contains additional summary-level information about the overall Lab Corps Pilot Process.

Recognizing Dish-STARS™ as a technology platform that enables several potential applications, an important portion of the Lab Corps effort was the development of value proposition and a product application strategy for the sequential rollout of systems for these applications. The resulting strategy envisions the following products and applications, in approximate order:

1) **H_2 production for fuel cell vehicles.** The Lab Corps effort confirmed this as the nearest-term application of Dish-STARS. This includes both H_2 production at fuel cell vehicle filling stations, when an adequate solar resource and sufficient square footage exists for the concentrators, and central H_2 production with appropriate transport to filling stations. In the near-term, this application area is limited in terms of the numbers of units that might be manufactured and sold; however, it has a relatively high cost target ($2/kg, not including cost of compression and transport, or about $15/MMBTU) and has other attributes that make it attractive for the nearest-term application.

2) **Production and reinjection of H_2 into natural gas pipelines.** This application area has a reasonable cost target ($8-10/MMBTU) and would justify the production and deployment of potentially tens of thousands of Dish-STARS units.

3) **Co-Production of liquid hydrocarbons (e.g., methanol) and H_2.** This application has relatively high cost targets (methanol is currently about $19/MMBTU) and very low carbon emissions other than the carbon within the methanol molecule. The result is low-carbon hydrogen plus moderately-low, lifecycle carbon intensity, with a greater return on investment per Dish-STARS unit. Considering that methanol is one of the world's largest commodity chemicals, the market potential is large.

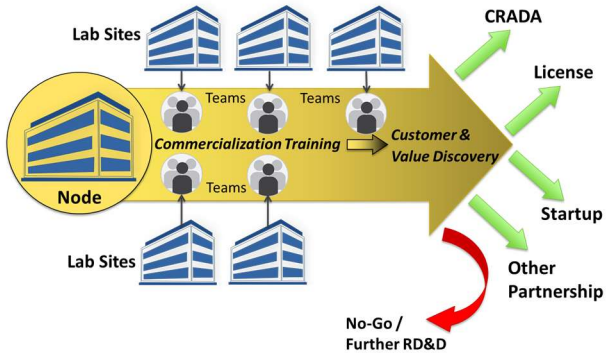

Figure 6-2 DOE EERE Lab Corps Process: During the evaluations, hypotheses about the business enterprise for each technology platform are evaluated, with conclusions drawn about the best commercialization strategy, such as CRADA agreements, licenses, the creation of a startup company, the formation of other partnerships, or a recommendation not to pursue the commercialization of the technology platform.

4) **Central and distributed power generation based on the solar augment in the syngas product.** Application of Dish-STARS for hybrid solar/NG, combined-cycle power systems has the potential for power generation at or near 6¢/kWh and distributed power generation is possible using micro-turbines and/or fuel cells. Co-production of liquid hydrocarbon fuels with power generation is also an option that yields greater economic value. Market potential is large.

5) **Distributed production of liquid hydrocarbon fuels from bio-gas and/or associated gas at landfills, anaerobic digesters, oil fracking sites, etc.** This application was not thoroughly investigated during Lab Corps but represents a potentially important application of Dish-STARS, especially once large-volume manufacturing and economies of hardware mass production have been obtained.

The preferred business strategy that evolved throughout the Lab-Corps effort consists of a Minimum Viable Product (MVP) based on Dish-STARS™ for applications 1) and 2). This combines the high cost target for fuel cell vehicle filling stations and the high production (manufacturing)

6.1.2 Follow-on From Lab-Corps

Lab-Corps evaluators assessed the Dish-STARS™ platform as a strong candidate for near-term commercialization, with a hydrogen production system as the Minimum Viable Product (MVP) and confirmed the Dish-STARS™ Business Model Canvas which identified a startup-company as an appropriate business vehicle.

As this report indicates, the three-phase SunShot project advanced Dish-STARS™ from TRL 3 to TRL 6. To move to a commercial product, the TRL must be advanced further, as follows:

- TRL 6 – System/Subsystem model or prototype demonstration in relevant environment
- TRL 7 – System prototype demonstration in an operational environment
- TRL 8 – Actual system completed and qualified in an operation environment
- TRL 9 – Actual system proven through successful mission operations.

To move Dish-STARSTM beyond TRL 6, a new, two-year CRADA project was proposed (and accepted) for cost-share funding by DOE's Technology Commercialization Fund with the following three objectives:

- The project will support the cooperative development of Dish-STARS™ by the DOE national laboratory and private partners, including the startup company, STARS Technology Corporation, that is being established by the PNNL Lab-Corps team that evaluated Dish-STARS™ on behalf of EERE, and other project team members including PNNL, Southern California Gas Company,
- The project will provide important transition funding at the time that the previous DOE SunShot project, which has supported Dish-STARS™ development from Technology Readiness Level 3 (TRL 3) to TRL 6, is scheduled to end. Otherwise, STARS development would halt until other funds are found.
- The project will help to accelerate the commercial deployment of Dish-STARS™, enabling STARS Technology Corporation to aggressively accomplish, by the year 2020, the dual goals of ramping up to volume production (hundreds to thousands of Dish-STARS™ units per year) – therefore achieving economics of hardware mass production – and groundbreaking for several major deployments by the year 2020. This will enable Dish-STARS™ to be available for a wide variety of applications, including distributed and central power generation, while taking full advantage of the Solar Investment Tax Credit.

This follow-on project will advance Dish-STARS™ through TRL 7 to TRL 8 in important ways. First, it will include additions to the TRL 6 Dish-STARS™ system such as a two-stage, water-gas shift reaction system that maximizes hydrogen production. Second, it will include upstream sulfur removal from the natural gas feedstock (to product reactor catalysts). Third, it will include downstreams separations and hydrogen purification to produce the hydrogen product and a recycle stream. Finally, it will include the investigation of additional valuable improvements including: a) electrical heating of the steam-methane reforming reactor to enable operation during periods where renewable electricity overgeneration is available and to increase the overall productivity of the Dish-STARS™ technology platform and b) initial work to initiate development of the methanol production subsystem which is relevant to applications where methanol would be co-produced with low-carbon hydrogen.

7.0 References

[1] P. H. Humble, D. R. Palo, R. A. Dagle and R. S. Wegeng, "Solar Receiver Model for an Innovative Hybrid Solar-Gas Power Generation Power Cycle," in *8th Annual International Energy Conversion Engineering Conference*, Nashville, TN, 2010.

[2] R. Philippe, M. Lacroix, L. Dreibine, C. Pham-Huu, D. Edouard, S. Savin, F. Luck and D. Schweich, "Effect of Structure and Thermal Properties of a Fischer-Tropsch Catalyst in a Fixed Bed," *Catalysis Today,* vol. 147, pp. S305-S312, 2009.

[3] C. Cao, Y. Wang and R. T. Rozmiarek, "Hetrogeneous Reactor Model for Steam Reforming of Methane in a Microchannel Reactor with Microstructured Catalysts," *Catalysis Today,* vol. 110, pp. 92-97, 2005.

[4] J. Szargut, D. Morris and F. Steward, Exergy Analysis of Thermal, Chemical, and Metallurgical Processes, New York: Hemisphere, 1988.

[5] R. Dvier, J. Fish, R. Levitan, M. Levy, E. Meirovitch, H. Rosin, S. Paripatyadar and J. Richardson, "Solar Test of an Integrated Sodium Reflux Heat Pipe Receiver/Reactor for Thermochemical Energy Transport," *Solar Energy,* vol. 48, no. 1, p. 21, 1992.

Pacific Northwest
NATIONAL LABORATORY

Proudly Operated by **Battelle** *Since 1965*

U.S. DEPARTMENT OF
ENERGY

902 Battelle Boulevard
P.O. Box 999
Richland, WA 99352
1-888-375-PNNL (7665)

www.pnnl.gov